CHALMERS
UNIVERSITY OF TECHNOLOGY

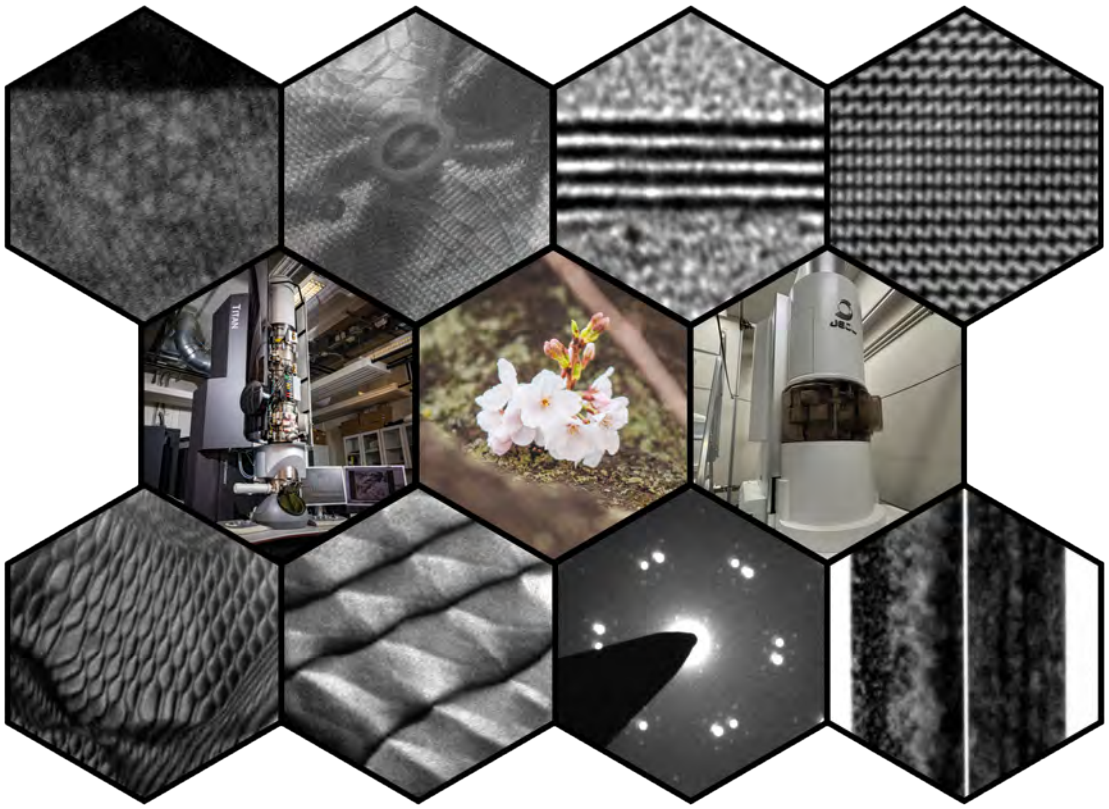

Fabrication and High-Resolution Structural Characterisation of 2D Material Moiré Structures

Master's Thesis in Physics

ERIC LJUNGBERG

DEPARTMENT OF PHYSICS AND ASTRONOMY
CHALMERS UNIVERSITY OF TECHNOLOGY
Gothenburg, Sweden 2026
www.chalmers.se

Master's thesis 2026

Fabrication and High-Resolution Structural Characterisation of 2D Material Moiré Structures

ERIC LJUNGBERG

CHALMERS
UNIVERSITY OF TECHNOLOGY

Department of Physics
Division of Nano and Biophysics
Eva Olsson Group
Chalmers University of Technology
Gothenburg, Sweden 2026

Fabrication and High-Resolution Structural Characterisation of 2D Material Moiré Structures
ERIC LJUNGBERG

Supervisor: Lunjie Zeng, Department of Physics
Examiner: Eva Olsson, Department of Physics

Master's Thesis 2026
Department of Physics
Division of Nano and Biophysics
Eva Olsson Group
Chalmers University of Technology
SE-412 96 Gothenburg
Telephone +46 31 772 1000

Cover: 1) HAADF-STEM image of PL6. 2) HAADF-STEM image of PL2. 3) TEM-BF image of MoS_2 cross-section. 4) Atomic resolution HAADF-STEM image of PL10 anti-parallel stacked domain wall. 5) Image of Thermo Fisher Titan TEM/STEM microscope. 6) JEOL ARM200F Photograph of cherry blossom in Ueno Park. 7) Image of JEOL JEM-ARM200F. 8) DF-TEM image of PL14 anti-parallel stacked domain structure. 9) DF-TEM image of PL3 parallel stacked domain structure. 10) SAED pattern of PL16 anti-parallel stacked domain structure. 11) BF-STEM image of 2H3R_1 cross-section.

Typeset in LaTeX
Printed by Chalmers Reproservice
Gothenburg, Sweden 2026

Fabrication and High-Resolution Structural Characterisation of 2D Material Moiré Structures

ERIC LJUNGBERG
Department of Physics
Chalmers University of Technology

Abstract

Atomically thin two dimensional (2D) materials have become a major research topic since the discovery of graphene. In particular, 2D transition metal dichalcogenides (TMDs), such as MoS2, have attracted extensive research interest due to their unique electrical and optical properties suited for a future-generation of electronic and optical devices. One unique property of 2D materials is that atomically thin layers can be artificially stacked together building tunable structures, for example, Moiré structures. Moiré structures constructed by atomically thin TMDs can be designed to generate and control new material properties, including superconductivity, ferroelectricity, and quantum hall effect. Understanding the fabrication of 2D TMD Moiré structures by stacking atomically thin layers, and determining the structure of 2D TMD Moiré structures with high spatial resolution, are of critical importance for developing and using the novel structures of 2D materials.

In this thesis work, an experimental setup and protocol for fabricating twisted TMD Moiré structures were successfully developed and completed. The fabrication procedure involves the preparation of atomically thin TMD layers from bulk crystals, accurate determination of thicknesses, and mechanical stacking of individual 2D TMD layers in a controllable manner. Then, the structure of twisted TMD Moiré structures was characterized at the nanometre and atomic scales using transmission electron microscopy (TEM) and scanning TEM (STEM). The focus was on stacked bilayer-bilayer and monolayer-monolayer MoS2 Moiré structures. Electron diffraction and TEM dark field (DF) imaging were used to reveal nanoscale domain structures resulting from atomic reconstruction in the Moiré structures. Moiré structures with parallel and anti-parallel stacking showed distinctly different domain structures. Furthermore, STEM imaging provided a direct visualization of domain and domain boundary structures at the atomic scale. DFT calculations were used to propose an hypothesis for the possible atomic arrangement at the Moiré domain boundaries. Possible electrical polarization resulting from changes in the atomic stacking of the structures was also studied using TEM selected area electron diffraction patterns. Evidence of in-plane polarization in MoS2 Moiré structures was observed in electron diffraction, while out-of-plane polarization in MoS2 with rhombohedral stacking was investigated using differential phase Contrast (DPC) STEM imaging.

Keywords: 2D Materials, TMD, DPC, STEM, TEM, Twist-tronics, Moiré Structures, Atomic Resolution Imaging

Acknowledgements

I would like to thank all members of the Eva Olsson Group for a wonderful time and plenty of fruitful discussions during my time in the group. Your support has been a crucial part in the work for my Master Thesis.

I would also like to thank Professor Naoya Shibata and his research group for hosting my visit to Japan and helping me with the measurements conducted there. A special thanks to Assistant Professor Shun Sasano, Takeshi Iwata, Dr. Aowen Li and Asuka Ishikawa for the help with taking the STEM and TEM images in Japan. It was a wonderful experience and I hope to see you all again soon.

I would also like to thank my friends and close ones for all the support with giving me feedback and keeping my morale high.

Eric Ljungberg, Gothenburg, June 2026

List of Acronyms

Below is the list of acronyms that have been used throughout this thesis listed in alphabetical order:

1G	First Generation
2D	Two Dimensional
2H	Two Hexagonal
2H3R	Name of sample with stacked 2H-MoS_2 and 3R-MoS_2 flakes.
2G	Second Generation
3R	Three Rhombic
AFM	Atomic Force Measurement
BF	Bright Field
bi-bi	bilayer-bilayer
cAFM	Conduction Atomic Force Measurement
CMAL	Chalmers Materials Laboratory
EELS	Electron Energy Loss Spectroscopy
DF	Dark Field
DFT	Density Field Theory
DPC	Differential Phase Contrast
tDPC	tilt-scan-averaged DPC
FIB	Focused Ion Beam
HAADF	High Angle Annular Dark Field
hBN	hexagonal Boron Nitride
HR	High-Resolution
LAADF	Low Angle Annular Dark Field
M	Metal
MoS_2	Molybdenum Disulfide
mono-mono	monolayer-monolayer
nms	Nanometers
PC	Polycarbonate
PDMS	Polydimethylsiloxane
PFM	Piezoelectric Force Microscopy
PVC	Polyvinylklorid
PW cut off	Plane wave energy cut off
SAED	Selective Area Electron Diffraction
STEM	Scanning Transmission Electron Microscopy
STM	Scanning Tunnelling Microscopy
TEM	Transmission Electron Microscopy
TMD	Transition Metal Dichalcogenides
X	Chalcogen

Contents

List of Figures

List of Tables

1
Introduction

Two dimensional (2D) materials is sheet like materials that is only a few atomic layers thick. The most well known 2D material is likely graphene, which consists of a single atomic layer consisting of carbon atoms. It has been showed that graphene has a range of uses in electrical applications thanks to its good electrical properties stemming from the k-point band structure. However, graphene does not have a band gap, which is necessary for many electronic applications such as transistors, electrical sensors and solar panels. A class of 2D materials called Transition Metal Dichalcogenides (TMDs) have attracted a lot of research interest because of their promising semi-conducting properties well suited for electrical and optical applications. A monolayer TMD consists of one atomic layer of a transition metal sandwiched between two layers of chalcogenide. In particular, it has recently been found that ferroelectric structures formed by twisting and stacking monolayer TMD crystals, creating Moiré patterns, possess unique properties that are absent in bulk ferroelectric materials. There have been investigations of the electric polarization and ferroelectric domain structures in 2D sliding ferroelectrics using techniques such as piezoelectric force microscopy (PFM), scanning tunnelling microscopy (STM), optical spectroscopy, capacitive sensing, field-effect sensing, as well as Transmission Electron Microscopy (TEM) or Scanning TEM (STEM) diffraction and imaging. Nanoscale domains that originate from atomic reconstruction between the constituting atomic layers and out-of-plane polarization within the domains have been observed [1]. However, domain wall structure and polarization at the walls in 2D sliding ferroelectrics are not well understood. Here, our goal is to characterize the atomic stacking and electric polarization at the ferroelectric domain walls in 2D sliding ferroelectrics at the nanometre (nm) and atomic scales using S/TEM. This thesis will focus on a TMD called Molybdenum disulfide (MoS_2) which consists of on layer of molybdenum with two layers of sulphur.

1.1 Aim

The thesis was written to address three questions.

What is the atomic structure in twisted MoS2 Moiré structures?

How can the thickness of atomically thin MoS2 be determined?

How can electric polarisation be studied in 2D Moiré Structures at the nm scale?

1.2 Limitations

Limitations had to be done to make the thesis feasible in half a year and with the expertise and equipment available. The main limitations are presented below.

The twisted structures were limited to select twist angles of 0.1°, 1°, 2° and 180°. This was to limit the size and spread of the domain size in the twisted structures to be suitable for TEM characterisation. The twisted structures were also limited to being constructed only with MoS_2-2H as this was the phase which the exfoliation method was developed on and time did not allow for additional phases and materials thickness determination methods being calibrated.

The characterisation of the twisted structures were limited to TEM and STEM. This were the techniques that would allow for the highest spatial resolution and was suitable to learn and use for the time frame of the thesis.

Measurement of the out-of-plane polarisation in MoS_2 was limited to the MoS_2-2H and Mos_2-3R phases. The MoS_2-2H served as a good reference for the MoS_2-3R as the MoS_2-2H should not have any polarisation but should have similar diffraction contrast. Due to this, no other materials were tested using DPC STEM and tDPC STEM.

1.3 Goal

The main goal of the thesis was to extract new information about the atomic structure of twisted structures to allow for a deeper understanding of the physical effects involved. The other goal of the master thesis regarding the twisted structures were to establish a production protocol to manufacture twisted structures, not only with MoS_2 but also with other TMDs. This would promote further work with twisted structures and other type of TMD structures. The goal of the cross-sectional measurement of the out of plane polarisation of MoS_2-3R was to test how DPC could be used to measure the out of plane polarisation of twisted structures and if the possible polarisation of the domain barriers could be imaged with DPC.

1.4 Structure of Report

The report starts with background information about the material systems. Explaining the structure of MoS_2 and how it can be used to construct twisted Moiré structures. Then, the characterisation methods used to analyse the twisted Moiré structures, for the development of the thickness determination method and the measurement of the out-of-plane polarisation is introduced with the working principle of SEM, FIB-SEM, TEM, STEM, DPC STEM and AFM explained.

Then, in Methods Chapter 3, the equipment and how it was used is presented. The transfer stage, used to produce the samples is explained and the way the thickness

determination method was developed is explained. The methods used to characterise the domain structures is then explained. Then, how the DFT calculations of the domain structures were made is then presented. The Chapter Methods ends with the DPC and tDPC measurements for measuring the out-of-plane polarisation being explained.

In Results Chapter 4, important aspects with the production of the twisted structures are presented with the results of the development of the thickness determination method. After, the characterisation of the twisted structures is presented. It is divided in the two type of Moiré structures present, anti-parallel and parallel. TEM and STEM images of both structures is presented with atomic resolution images and DFT calculations being presented for the anti-parallel structure. The Results chapter ends with presenting the results for the DPC and tDPC measurement. The thesis ends with Conclusions summarising the insights gained from the thesis.

2

Background

This chapter introduces the 2D TMD material MoS_2. It explains the structure and bulk phases 2-Hexagonal (2H) and 3-Rhombic (3R). It also introduces the concept of twisted Moiré structures and how MoS_2 can be used to construct these. The working principles of the microscopy techniques used to characterise these structures is then explained.

2.1 Structure of MoS_2 and Twisted Moiré Structures

In this section, the structure of MoS_2 is explained as well as the reason why MoS_2 is a good material to study. The section then explains what types of Moiré structures has been studied and how they are formed

2.1.1 MoS_2 Structure and Properties

MoS_2 is a TMD material. One MoS_2 layer consists of three atomic layers, one molybdenum sandwiched between two sulphur layers. Monolayer MoS_2 have a thickness of 6.1 nm [2]. Layers in a MoS_2 crystal can stack in two main phases, the 2H phase and the 3R phase. The main differences between them are that 2H-phase has two layers in its unit cell and no intrinsic polarisation whereas the 3R-phase that has 3 layers in its unit cell and intrinsic out-of plane polarisation. The 3R phase has two configurations, the metal atom in the top layer (M) sits directly on top of the chalcogen (X) in the bottom layer called MX´ and vice versa called X´M. The structure of MoS_2-2H and MoS_2-3R X´M can be seen in Figure 2.1 [3][4].

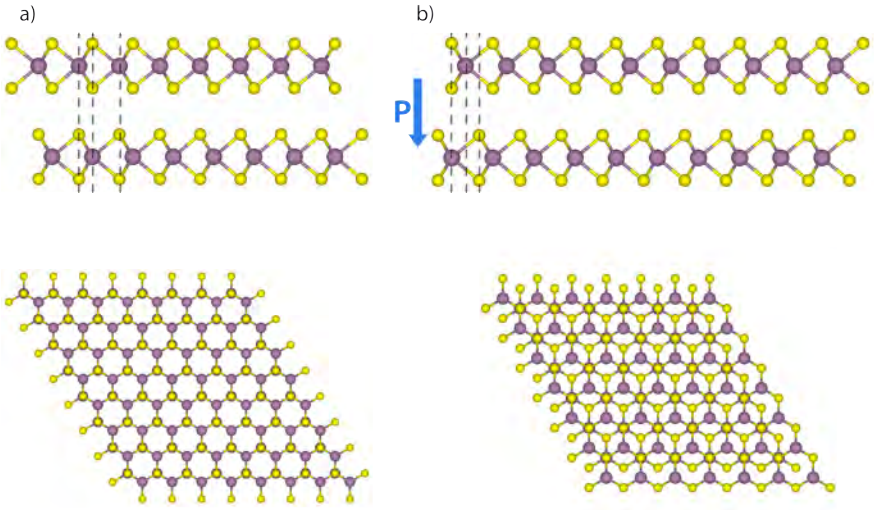

Figure 2.1: a) Shows 2H unit cell and side-on view of the stacking with sulphur in yellow and molybdenum in purple. b) Shows 3R unit cell and side-on view of the stacking with sulphur in yellow and molybdenum in purple. The figure is constructed using the crystallographic data from the Crystallography Open Database [3].

Important to remember is that when isolating a single layer (monolayer) of MoS_2, there are not multiple phases [5].

MoS_2 exhibit interesting electronic band gap properties dependent on the number of layers. The band gap increases with decreasing number of layers and at monolayer the band gap goes from an indirect to a direct band gap. This is a reason why the transport properties have had a large research interest for electronic application. Fewer layers makes the band gap larger and closer to a direct bandgap, which makes the flake absorb more light and of higher wavelengths. This in part explains the flakes changing colour dependent of the number of layers they have.

2.1.2 2D Material Moire structures

Moire structures are created by overlapping two periodic structure over each other with a twist, creating a new periodicity in the pattern dependent on the twist angle θ. The formula for how big the periods in this new pattern are can be described with Equation 2.1 [6]

$$\lambda = \frac{a}{2\sin\frac{\theta}{2}}. \tag{2.1}$$

Due to the gradual change of the moire pattern, the material is not located in its minimal energy configuration. Therefore, the atoms will periodically be displaced to maximise the area of the structure with the lowest energy configuration, creating domains with uniform low energy stacking with domain walls between [7]. An image showing the atomic models of non-relaxed, lacking this relaxations process, and relaxed, with the relaxation process, twisted bilayer graphene can be seen in Fig-

ure. The collective displacement of the atoms is called Periodic Lattice Distortions (PLD)2.2a.

MoS_2, two main ways of Moiré structures can be formed by stacking the layers at the interface either in the same direction, called parallel, or with the adjacent layers rotated 180 degrees relative to each other, called anti-parallel. Making parallel stacked Moiré structures creates domains with 3R phase type stacking. Due to the stacking of the 3R phase in the Moiré pattern, the domains for parallel stacked structures alternate between a MX and XM structure. A STEM image of a parallel stacked Moiré structure can be seen in Figure 2.2b. The domains in a anti-parallel stacked Moiré structure are instead of a 2H phase type structure. The appearance of these can be seen in Figure 2.2c.

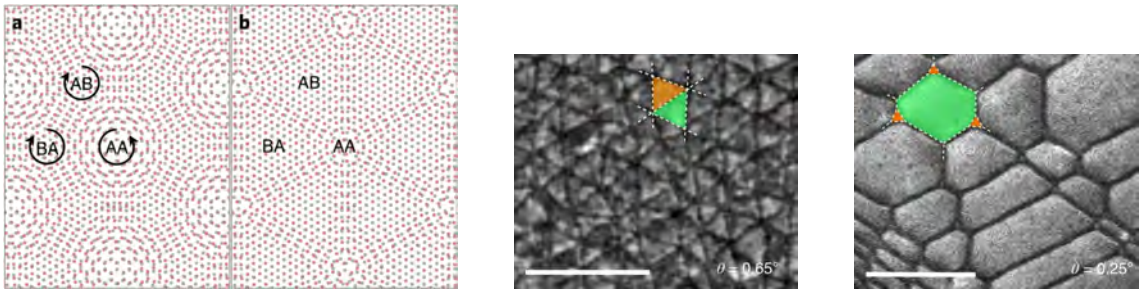

(a) **(b)** **(c)**

Figure 2.2: a) Atomic model of non-relaxed and relaxed twisted bilayer graphene [8]. b) STEM images of parallel stacked Moiré structure with the two types of domains are marked in green and orange. The scale bar is 100 nm. c) STEM images of anti-parallel stacked Moiré structure with a domain marked in green. The scale bar is 100 nm [5].

2.2 Electron Microscopy

For high-resolution characterisation of materials, a range of electron microscopy techniques are needed. In this thesis, the main characterisation method was electron microscopy. Therefore, in this section, the working principles of different electron microscopy techniques used are explained starting with electron microscopy techniques for deeper understanding of these techniques.

2.2.1 Scanning Electron Microscopy (SEM)

SEM is a technique for imaging conducting samples by using electrons scattered by the sample surface from an electron beam. The basic working principles begins at the electron gun. Electrons are ejected from the electron gun, then guided and formed by magnetic coils and apertures into a beam that hits the surface of the sample. The electrons from the beam scatters in the sample, knocking electrons out of the shells of the atoms and creating secondary electrons. The electrons from the beam also scatter and exit the sample, creating backscattered electrons. As the

beam is scanned over the sample, these secondary and backscattered electrons can be captured and used to create images of the sample. Secondary electron images are more sensitive to the topology of the sample, whereas the backscattered electrons are more sensitive to the elemental composition of the sample. The electrons in the electron beam can be accelerated at different acceleration voltages, usually up to 30kV. Accelerating the electrons at higher acceleration voltages makes the electrons go furtherer into the sample and generating more backscattered electrons [9].

2.2.2 Transmission Electron Microscopy (TEM)

TEM is a technique that images thin samples (usually below 100nm [10]) by transmitting an electron beam through the sample and detecting the transmitted electrons. The basic working principle of a TEM is described in Figure 2.3. A TEM system works by electrons being ejected from the electron gun. The electrons are formed into a beam by the illumination system consisting of collimator lenses and apertures. In TEM, a parallel beam is used. The final shape is then refined by the objective lens and then transferred through the sample. The outgoing beam is then projected by the imaging system onto a fluorescent plate or charge coupled-device(CCD) camera. The imaging system can project the focal plane of the objective lens to get a normal image of the sample, but it can also image the back focal plane of the objective lens to image the diffraction of the sample. With the objective aperture, the electrons from the middle diffraction spot, the bright field(BF) spot, can be blocked and only allow electrons from a certain diffraction spot, creating a dark field(DF) image [10].

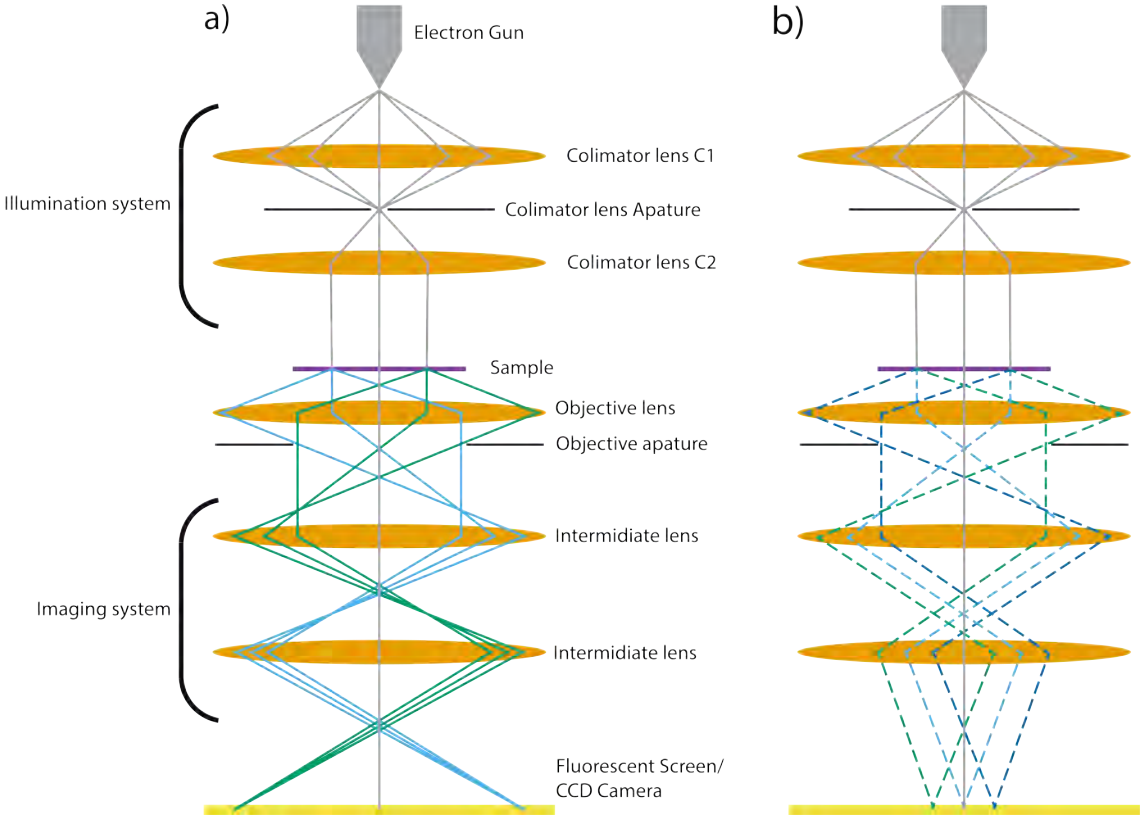

Figure 2.3: Schematic image of the working principle of TEM. a) Illustrates imaging mode. b) Illustrates diffraction mode.

2.2.2.1 Diffraction

Electrons travelling through a material can scatter off the atoms present the material. If the material is crystalline, the electrons can scatter off the atomic planes and at some angles exhibit constructive interference. This can be likened to light bouncing of a set of mirrors and is called Bragg diffraction after the use of bragg's law to predict the spots created. The diffraction of the atoms can be captured by projecting the objective lens back focal plane onto the fluorescent plate of CCD camera, this can be seen in Figure 2.3. Projecting the back focal plane captures the so called diffraction pattern which can be used to analyse the crystal structure of the sample. Each spot in the diffraction pattern come from an atomic plane in the sample except for the middle spot which are electrons that have not been scattered. An example of the diffraction pattern from MoS_2 can be seen in Figure 2.4a.

In some samples, the diffracted beams of one plane can diffract again on planes further into the sample, this is called double diffraction. In this case, a similar diffraction pattern is created around the diffraction spots as around the bright field spot. A schematic figure of double diffraction is drawn in Figure 2.4b. Important to remember is that the double diffraction dots around a main spot comes from the diffraction of the nearby main diffraction spots [10].

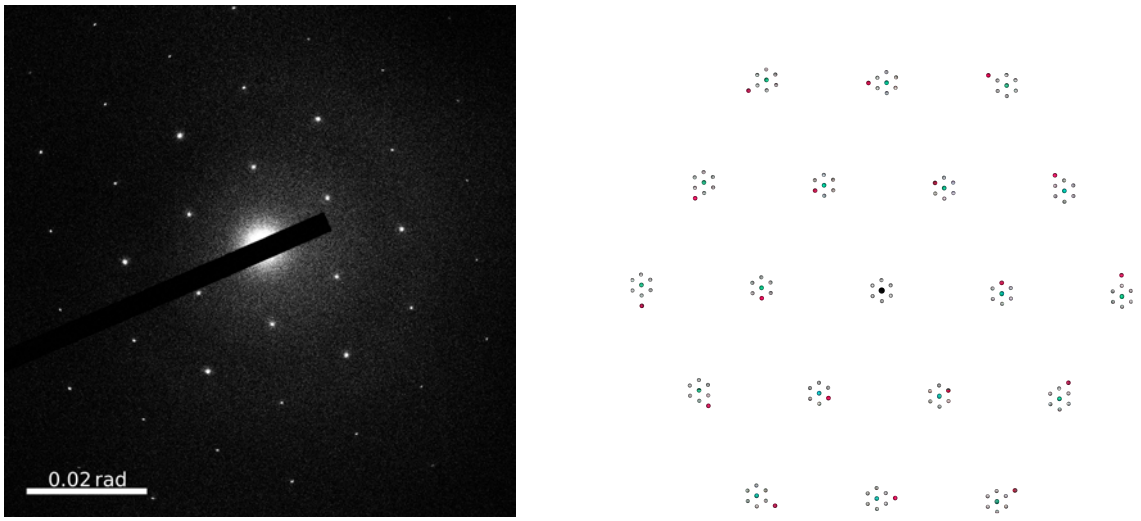

(a) 2H-MoS_2 diffraction pattern **(b)** Double diffraction pattern.

Figure 2.4: Image a) is a diffraction pattern of 2H-MoS_2 captures in a JEOL JEM-F200. The black stripe is the beam-stop blocking the BF spot. Image b) is a schematic drawing of the double diffraction pattern from two 2H-MoS_2 crystals on top of each other. The red dots are from the top 2H-MoS_2, the blue are from the bottom 2H-MoS_2 and the gray dots are the gray dots are the double diffraction spots.

2.2.3 Scanning Transmission Electron Microscopy (STEM)

STEM is similar to TEM, but instead of using a parallel beam for imaging, a focused beam is used and scanned across the sample. To create an image, the amount of electrons coming through the sample is recorded. Annular detectors are placed below the sample at different scattering angles, making it possible to form images from different kinds of signals. Signal captured from non scattering or next to non scattered electrons are called BF, signal using electrons scattered at low angles are called LAADF (Low Angle Annular Dark Field) and signal using electrons scattered at high angles are called HAADF (High Angle Annular Dark Field). The detectors used to capture these signals are usually a disk, thus the annular term in the name of the signals [10].

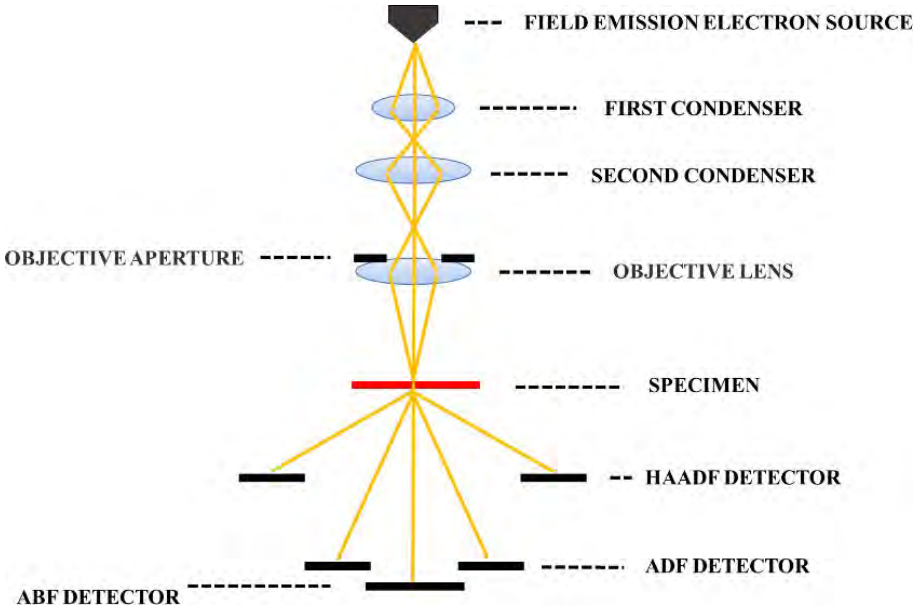

Figure 2.5: Figure of the detectors in STEM [11].

The different signals can be used to image different features in smaples based in the atomic numbers of the atoms present causing the deflection of the electrons.

2.2.4 Differential Phase Contrast (DPC)

DPC is a STEM technique that uses segmented detectors instead of normal annular detectors to detect magnetic and electric fields in materials. By making the BF spot large, the deflection of the BF can be detected by measuring the movement of the centre of mass(CoM) of the BF spot. The deflection of the electrons could then be correlated to the magnetic or electric fields present in a sample. A figure of the working principle of DPC is shown in Figure 2.6

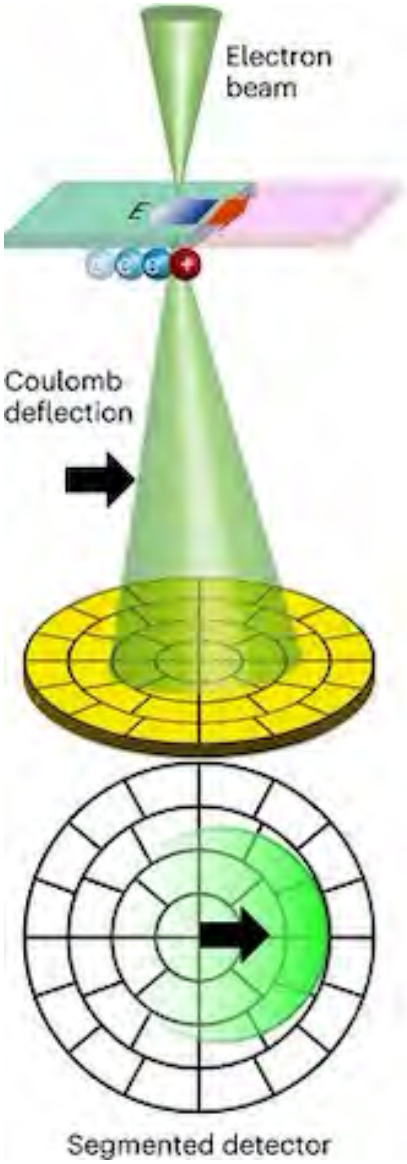

Figure 2.6: Figure of the detectors in DPC [12].

A problem with this technique is diffraction contrast sensitivity. Materials that have strong diffraction contrast can move the CoM dependent on zone axis alignment or variance in crystal structure in the material, thus creating CoM shift not stemming from the presence of electric or magnetic fields. A method to combat this is tilted DPC (tDPC). tDPC uses the same principle as normal DPC but tilts the beam at different angles for each spot and uses the average CoM shift. This decreases the CoM shift from the material structure but preserve the shift from the magnetic or electric field [12].

2.2.5 Focused Ion Beam (FIB)-SEM

FIB-SEM is a combined system of a SEM and a FIB which allows for high precision milling at high spatial resolution. The milling process is done by ejecting ions, at high speeds to knock away material in the sample. This process can also be used to

deposit material by injecting a precursor gas and knocking the heavy atoms in the gas on to the surface of the sample using the ions from the FIB system. To produce a cross-section using this system, trenches are dug around the area of interest and a micro-manipulator is attached to lift out the cross section and bring the cross-section to a copper TEM grid where it can be attached [13].

3

Methods

In this chapter, the method to produce stacked 2D material structures is described. It first describes the exfoliation process to create atomically thin MoS_2 flakes, followed by a description of the method to stack flakes to create Moiré stacks. Then, the different characterisation methods used to investigate these structures is explained. Finally, the method for measuring the possible out-of-plane polarisation stemming from the stacking in MoS_2-2H and MoS_2-3R is explained.

For the production of samples and characterisation, various instruments were used. In Table 3.3, a summary of all the instruments used can be seen. The use of each is described in this chapter.

3.1 Fabrication of MoS_2 Moiré Structures

In this section, the method used to produce stacked 2D material structures is described. It first describes the main tool used, the Transfer station. It then describes the exfoliation process that produced atomically thin flakes for stacking. Then, the thickness determination that was developed is described that allowed for fast and accurate identification of the number of layers in the atomically thin flakes. The section ends with describing the stacking process of used for both atomically thin flakes but also thicker flakes.

3.1.1 Experimental Setup for Mechanical Exfoliation and Stacking of 2D Materials

For the assembly of samples, an in-house built transfer station was used. Images of the transfer station can be seen in Figure 3.1. The transfer station was built for assembling 2D samples on different kinds of silicon chips and TEM grids.

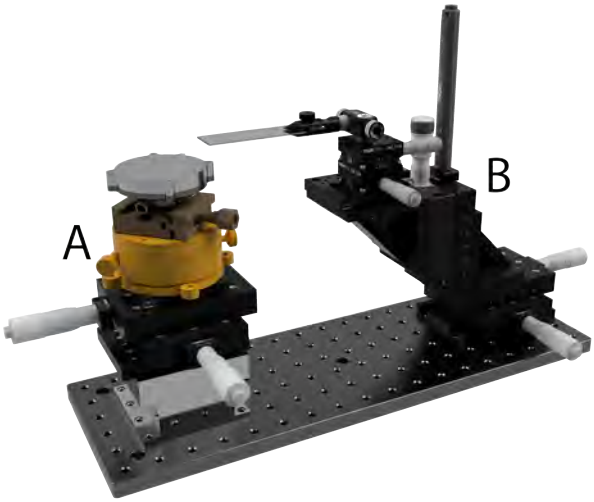

(a) Rendering of the Transfer station.

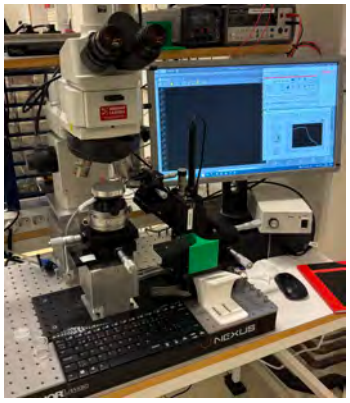

(b) Photo of the Transfer Station.

Figure 3.1: Images of the Transfer Station used for the assembly of samples. a) A render where the letter A highlights the chip holder system and the letter B highlights the moving arm system.b) Image of Transfer Station in the lab.

The Transfer station has two main systems, the chip holder system and the moving arm system. The chip holder system holds the chip on which the transfer is performed on. It consists of two Thorlabs PT1 micrometer slides, one Newport M-UTR80 rotation stage, one Arca Swiss screw mount modified with magnets attached, and a custom vacuum chuck on top. The slides move the chip in plane, the rotation stage rotates the chip, and the vacuum chuck heats the chip and holds it down with vacuum applied on the underside of the chip. The moving arm system consists of two micrometer slides, one motorized slide, one piezo motor slide, one goniometer and one glass slide holder. The two micrometer slides move the moving arm in plane, and the motorized slide moves it up and down. The piezo motor slide can also be used for higher precision vertical movement, but only the normal motorized slide was used. The goniometer controls the angle of the glass slide attached to the moving arm with the glass slide holder. The heating of the vacuum chuck and the movement of the motorized slide was computer controlled with a custom built LabView program and Thorlabs Kinesis software. With this setup, the position and angle of the chip (or TEM grid) mounted as well as the position of the glass slide attached can be fully controlled. An optical microscope is mounted above the stage to see the samples being prepared. The temperature was controlled with a control loop consisting of a digital multimeter measuring the potential over a thermocouple for measuring the temperature and thermal element connected to a power source for heating. The code for the control loop was written in LabView.

3.1.2 Preparation of 2D TMD Flakes by Mechanical Exfoliation

For the production of flakes, dry mechanical exfoliation was used. This method works because the forces between the tape and the flakes are stronger than the interlayer Van der Waals forces, allowing the tape to split the flakes[14]. Nitto Semiconductor Wafer PVC Tape tape and silicon chips were used for the exfoliation. SiO_2 chips with 285nm thick oxide for bigger optical image contrast[15]. The flakes were exfoliated once from the crystal, twice using only the tape and then between the tape and the chip. Exfoliations after the first exfoliation of the mother tape were performed using the exfoliation attachments for the transfer station seen in Figure 3.2b.

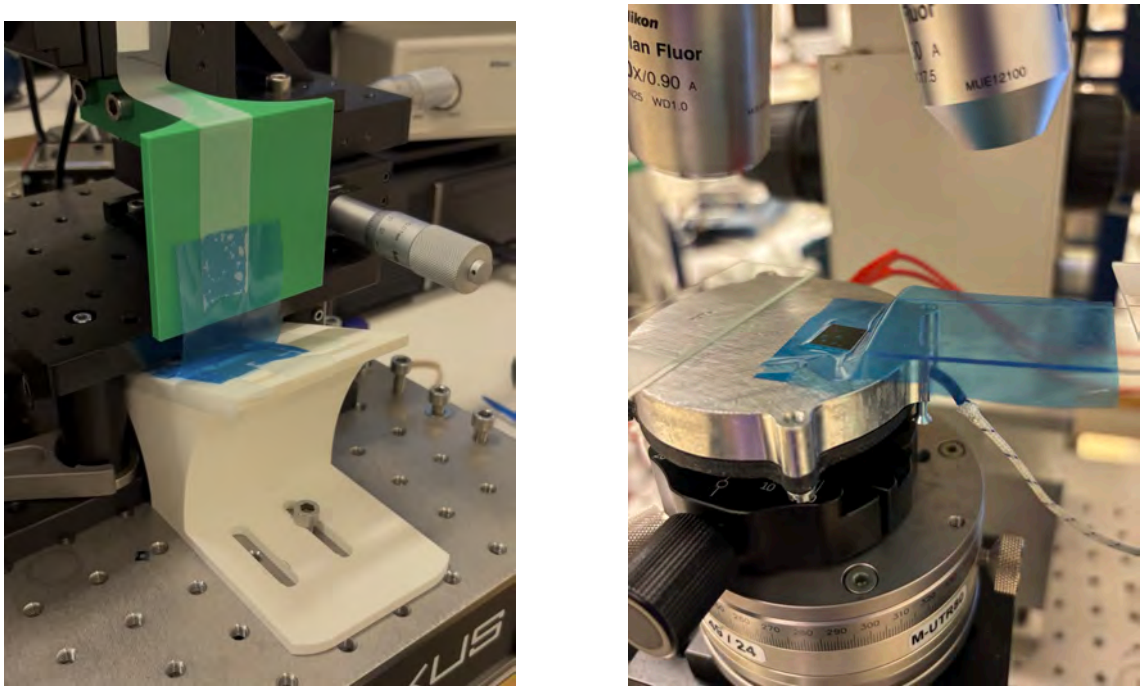

(a) **(b)**

Figure 3.2: a) Image of exfoliation of flakes using tape strips. The green plate moves upwards and the white plate is stationary. b) Image of peeling process for the final exfoliation of the flakes to the substrate. The chip can be seen as a black square covered by blue PVC tape.

The complete procedure executed was as follows.

1. The silicon chips were heated to 200°C for 1 hour.
2. The crystal MoS_2 was pressed against the mother tape strip using tweezers.
3. The first generation (1G) tape strips were pressed against the mother tape with a wide cotton swab and lifted off the mother tape at 70° tilt using the transfer station with a speed of 0.5mm/s vertically. This was repeated six times. The exfoliation setup can be seen in Figure 3.2a.

4. The same exfoliation process was repeated once per 1G tape strip, yielding second generation (2G) tape strips .
5. The silicon chips were plasma cleaned for 10 minutes.
6. Within 20 minutes of the plasma cleaning being finished, the 2G tape strips were applied to the chips with a wide cotton swab.
7. The chips with the 2G tape strips applied were heated at 80°C in a hot plate with pressure applied for 30 minutes.
8. The chips were cooled down while under pressure and then the tape were peeled off using the transfer station at ca 90° and a speed of 0.5mm/s vertically. The peeling setup can be seen in Figure 3.2b.

3.1.3 Thickness Determination of Atomically Thin MoS_2 Flakes

To establish the thickness determination of a atomically thin MoS_2 flakes using the optical contrast, Atomic Force Measurement (AFM), Raman spectroscopy and cross-sectional high-resolution (HR)-TEM was used as control measurements. In this section, each step is described. First, how the acquisition of the image contrast is performed is explained. Then the calibration of the image contrast is explained by going through the experimental details of how Raman spectroscopy, AFM and cross-sectional HR-TEM was performed.

3.1.3.1 Image Contrast in Optical Microscope

To acquire the colour contrast for each flake, an image was taken of the flake using a Nikon LV-UEPI-N equipped with an IMAGINGSOURCE DFK 33UX264 camera with Nikon NIS-Elements D software using the following settings:

Table 3.1: Software settings for Nikon NIS-Elements D.

Setting	Value
Gain	1
Red Gain	2
Green Gain	1
Blue Gain	1
Gamma	2
Offset	1
Apertures	Fully Open

Then, a line profile was taken using the software and the average value of each colour channel of the line profile was used for the absolute intensity of the flake. Finally, the absolute value was divided by the absolute value of the substrate, in this case 300 nm SiO_2. This was repeated for all flakes used for the model.

3.1.3.2 Raman Spectroscopy

Raman spectroscopy on atomically thin 2H-MoS_2 was performed on a WITec alpha300 R Raman microscope with a 532 nm laser. The flakes were analysed using spot measurements from each region and the distance between the A_{1g} and E^1_{2g} was used for analysing the thickness, as well as the position of the A_{1g} and E^1_{2g} peaks. These features change depening in the number of layers present. A spectrum from a 2H-MoS_2 can be seen in Figure 3.3.

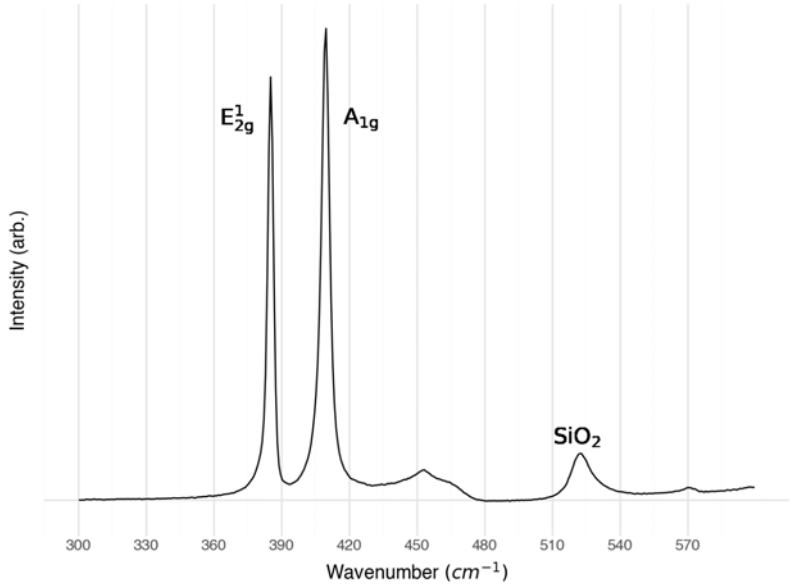

Figure 3.3: Raman spectrum showing the main peaks visible for MoS_2 and SiO_2 marked.

The peak positions were determined using functions in the Scipy python package.

3.1.3.3 Thickness Determination of 2D TMD Flakes Using AFM

AFM is a method to measure a materials properties by probing it with a nm thin Si or Si_3N_4 needle. The materials response on the needle is measured by shining a laser on the backside of the needle and tracking the deviation from the equilibrium position. This is done while raster scanning, creating high resolution images of the material analysed. Many material properties can be measured using AFM, one of them being the thickness of 2D material flakes[16].

The AFM data was acquired using a Bruker Dimension 3100 AFM in tapping mode. The images captured was analysed using the Gwyddion software by levelling the image using the silicon substrate. Height values of the flakes were captured by and making line profiles at the edge of the flakes and the substrate and subtracting the height of the flake with the height of the substrate.

3.1.3.4 Cross-Section Preparation by FIB-SEM

Cross-sections of atomically thin MoS_2 flakes were produced to prepare cross sectional TEM specimens using a FEI Versa3D FIB-SEM using a gallium ion source. To prepare the cross-sections, the flakes were first covered with graphite. The graphite protects the flakes during platinum deposition which was done to protect the flakes during milling. Graphite is also a Van der Waals 2D material which allowed for stacking. Then, a lamella of the flake was lifted out and placed on a copper TEM grid after which the final thinning was done. The final thickness of the cross-sections was <100nm in thickness.

3.1.3.5 Cross-Sectional HR-TEM of 2D TMD Flakes

Cross-sections were analysed using a FEI Tecnai TEM microscope. HR-TEM BF images were taken of the cross-sections at 200kV acceleration voltage and analysed using open source software ImageJ and the python package HyperSpy.

3.1.4 Construction of 2D TMD Moiré Structures

The process of stacking the flakes is done with a polymer stack consisting of a Poly-Carbonate (PC) film on a Polydimethylsiloxane (PDMS) mounted on a glass slide. The first step to create the polymer stack was to prepare the PC film. This was done by dissolving PC in chlorophorm with a 6 wt%. Pipetting 70μL onto a glass slide and pressing it down with a second glass slide, then sliding them against each other along the long edge. This created a PC film around 2μm thick. The glass slides were heated on a hot plate at 100°C for 2 min and then the film was cut to 1.5-2 cm squares. A 2 mm square of PDMS was placed on a new glass slide. A 1 cm square whole was cut from scotch tape and used to pick up the PC film. The film was then applied to the PDMS square and the stack was finally heated on a hot plate at 120°C.

With the polymer stacks prepared, the stacking process could begin. The stacking began with the selection of flakes. If thicker flakes were chosen, they sometimes needed to be cut. This was done with a 532nm laser with a power of 0.1mW in a WITec alpha300 R. The line measurement with 1 second dwell time and 40 points was used to get straight cuts in the flakes. Once the flakes were ready for stacking, the chip with the flakes was mounted on the vacuum chuck and heated to 75°C. The polymer stack was angled and brought down until it made contact with the chip. The point of contact created a line, this was called the wavefront. The wave front was moved over the flake that was to be picked up by pushing the polymer stack down. The flake was picked up by lifting the polymer stack up again. The chip was moved to a new position and the wave front was moved over the second flake with the first flake aimed on top of the second flake. The temperature was increased to 85°C, then the wavefront was moved back. This was repeated until the stack was complete. Deposition of the stack was performed by setting the temperature to 85°C. The wavefront was moved over the stack and the temperature was increased to 180°C over a 10 min period. During the process, the polymer stack was moved upwards to compensate for the thermal expansion of the PDMS. At 150°C,

the PC detached from the PDMS and at 180°C the PC melted of the polymer stack which could then be removed. The chip or TEM grid was then cooled down to room temperature and then submerged in chlorophorm to remove the PC on the chip or TEM grid and left a clean 2D material stack.

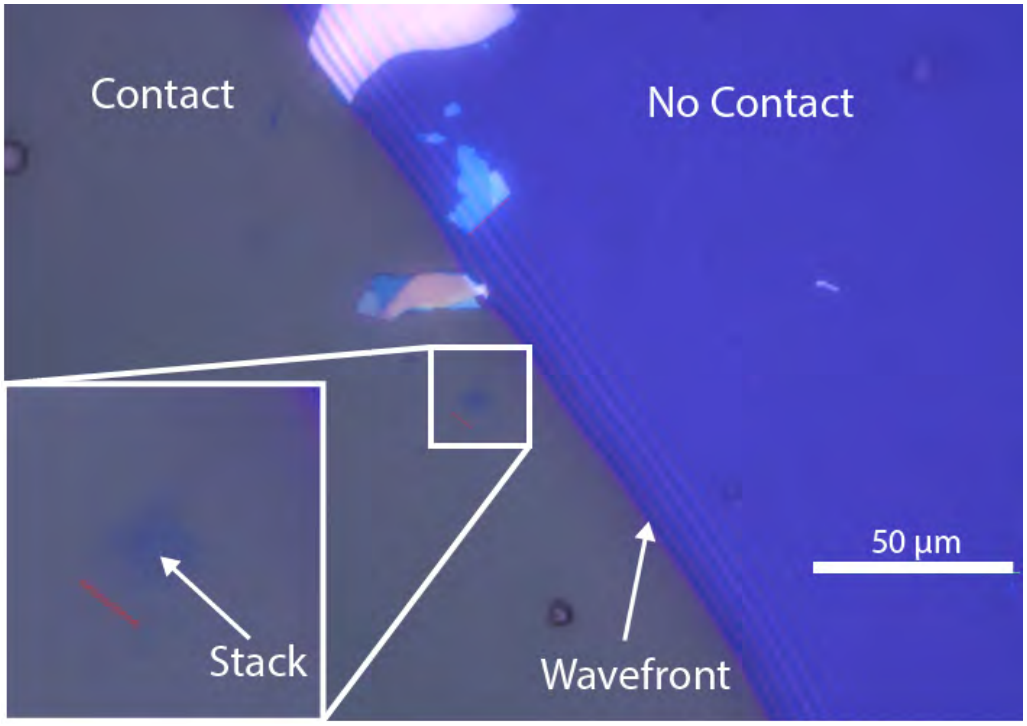

Figure 3.4: Image of stacking process. The bottom left area is where the PC has made contact with the substrate and the purple top right area is were no contact has been made. The shapes in the middle of the image are MoS_2-2H flakes.

3.1.5 Samples Produced for Characterisation

Stacked Moiré structures were constructed by stacking two bilayer or monolayer flakes on top of each other with a twist. This created Moiré structures with both parallel and anti-parallel stacking at the interface. A table for all the planar samples made can be seen below in Table 3.2.

..

Table 3.2: List of all produces Moiré stacks.

Sample	Thickness	Kind of Stack	Twist Angle (deg)	Grid
PL1	Bi-Bi	Anti-Parallel	0.1	300nm SiN 300nm holes
PL2	Bi-Bi	Anti-Parallel	0.1	5nm SiN
PL3	Mono-Mono	Parallel	0.1	300nm SiN 300nm holes
PL4	Mono-Mono	Parallel	0.1	300nm SiN 300nm holes
PL5	Mono-Mono	Parallel	1	300nm SiN 300nm holes
PL6	Mono-Mono	Parallel	2	300nm SiN 300nm holes
PL7	Mono-Mono	Parallel	0.1	5nm SiN
PL8	Mono-Mono	Parallel	0.1	300nm SiN 300nm holes
PL9	Mono-Mono	Parallel	0.1	300nm SiN 300nm holes
PL10	Mono-Mono	Parallel	0.1	300nm SiN 300nm holes
PL11	Mono-Mono	Parallel	0.1	300nm SiN 300nm holes
PL13	Bi-Bi	Anti-Parallel	0.1	300nm SiN 300nm holes
PL14	Bi-Bi	Anti-Parallel	0.1	300nm SiN 300nm holes
PL15	Bi-Bi	Anti-Parallel	0.1	300nm SiN 300nm holes
PL16	Bi-Bi	Parallel	180.1	300nm SiN 300nm holes

There were also two Mono-Mono stacks sandwiched between hBN flakes, these were lost in the final step of cleaning the PC of the flakes with chlorophorm. These account for the missing samples PL12 and PL17. The reason why these were washed off and not the normal samples are unknown.

3.2 Characterisation of Twisted TMD Moiré Structures

In this section, the techniques used for the characterisation of bilayer-bilayer (bi-bi) and monolayer-monolayer (mono-mono) stacks is described. It starts with presenting the Moiré stacks produced. Then the different techniques used to characterise the Moiré structures is described. Lastly, the way DFT calculations made to calculate the energy distribution over the barriers observed is explained.

3.2.1 TEM of Twisted TMD Moiré Structures

The samples produced were analysed using TEM at 80keV acceleration voltage to avoid knock-on beam damage. Two different TEM microscopes were used, a Thermo Fisher FEI Tecnai T20 LaB6 and a JEOL JEM-F200. DF was used during operation on both microscopes but in different ways. On Tecnai, a diffraction spot was chosen for DF and isolated using the objective aperture. On F200, the beam was deflected so the diffraction spot that was chosen for DF was moved to the BF spots normal position and an aperture was inserted.

3.2.2 STEM of Twisted TMD Moiré Structures

HAADF-STEM images with atomic resolution of bi-bi stacks were captured with a JEOL ARM200F at 80kV by capturing 10/20 images using 4 μs pixel dwell time and then stacking them. The image series were stacked by selecting non-distorted frames and correcting the frames for drifting effects.

Low mag HAADF-STEM, LAADF-STEM and BF-STEM images were taken by JOEL Ltd. using a JSM-IT810 with a segmented detector at an acceleration voltage of 30 kV.

3.2.3 DFT Calculations of Barrier Structures

Density Field Theory (DFT) is a calculation method to calculate the electron density of a system. Calculating the electron density can explain many aspects of a system, such as density of states, relaxation processes, and total energy of a system. DFT is performed by describing the electron density as a functional and minimizing this functional. The electrons interactions are in this case represented as plane waves. Two important parameters to control when performing DFT with plane waves are the plane wave energy cut off (PW cut off) and the k-point sampling. These parameters need to be set to values that allow the system to converge, otherwise the results may be misleading and show higher energies because of incomplete convergence.

DFT calculations were performed using the python packages ASE and GPAW. ASE was used to create the atomic models from MoS_2-2H[3] by stacking, translating and rotating unit cells. The optimisation of the DFT calculation parameters plane wave cut-off and k-point sampling was performed by calculating the total energy of the system and checking convergence against time. Convergence was determined to have been achieved when stable low energy was observed. These results can be seen in Figure 3.5b.

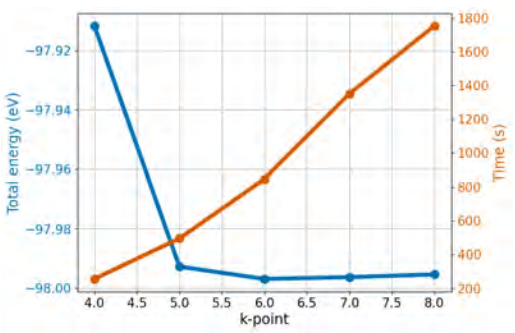

(a) k-Point Sampling

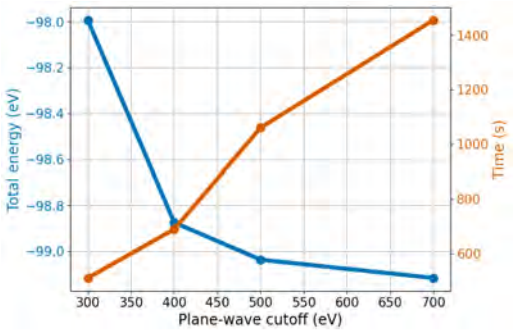

(b) Plane Wave Cut Off

Figure 3.5: a) k-Point sampling convergence plot. The blue is the total energy calculated and the red is the calculation time. b) PW cut off convergence plot. The blue is the total energy calculated and the red is the calculation time. Both convergence test were run on the domain structure and the vortex structure and showed similar results.

The parameters chosen were a PW cutoff of 500 eV and and a k-point sampling of 5 points. This was deemed the best compromise between calculation convergence and calculation time.

The calculations for the barriers local energy distribution were performed by constructing three atomic models from areas in the ant and armchair type barrier. The total energy was then calculated and compared with the total energy of the domain structure.

Calculations for the local energy distribution for the pure shift of bilayers in the $[10\bar{1}0]$ and $[21\bar{1}0]$ directions were performed by first constructing 13 systems with incrementally more shift between the two bilayers for half a unit vector. The step size of the shift was 0.16 Å. The structures were made from two unit cells with 12 atoms in total. The total energy was calculated for all systems and compared to the energy of the domain structure. The calculations were repeated for the $[10\bar{1}0]$ for a hole unit vector to include the entire barrier to investigate if the total energy was symmetric over the barrier. This was shown to be the case, thus the following calculations was only made for half a unit vector.

Calculations for the energy preference of the angle of the shift between the two bilayers were performed by first constructing 15 systems with 0.95 Å shift between the two bilayers with incrementally higher angles. The step size of the angle was 2.14°. Then, the total energy was calculated and compared to the 0° shift.

The structures were made from two unit cells with 12 atoms in total. 20 Å of vacuum was added and periodic boundary conditions were set to false for the out-of-plane direction to insure that the calculations did not treat the system as being bulk in the number of layers. The thickness of the vacuum is a parameter that could have been optimised to ensure correct energy conversion and optimal calculation time. But due to time constraints, the vacuum was set to a value of 20 Å which

was deemed high enough.

3.3 Experimental Setup for Measuring Stacking Induced Polarisation

In this section, the method to measure the bulk stacking induced polarisation in MoS_2-3R is explained. It started with producing cross-sections of MoS_2-3R and MoS_2-2H flakes. Then, DPC imaging was done to check for diffraction contrast. As diffraction contrast was present, tDPC was then used. Lastly, the data was analysed with a written python program.

3.3.1 Fabrication of Cross-Sections of MoS_2-3R and MoS_2-2H flakes with FIB-SEM

Stacks of MoS_2-3R, MoS_2-2H and graphite was deposited on SiO_2 285 nm substrates. Cross-section was then made from the stacks. For final preparation, the cross-section was thinned down to a thickness of 200-250nm and 125nm.

SEM images from the FIB-SEM preparation can be seen in Figure 3.6

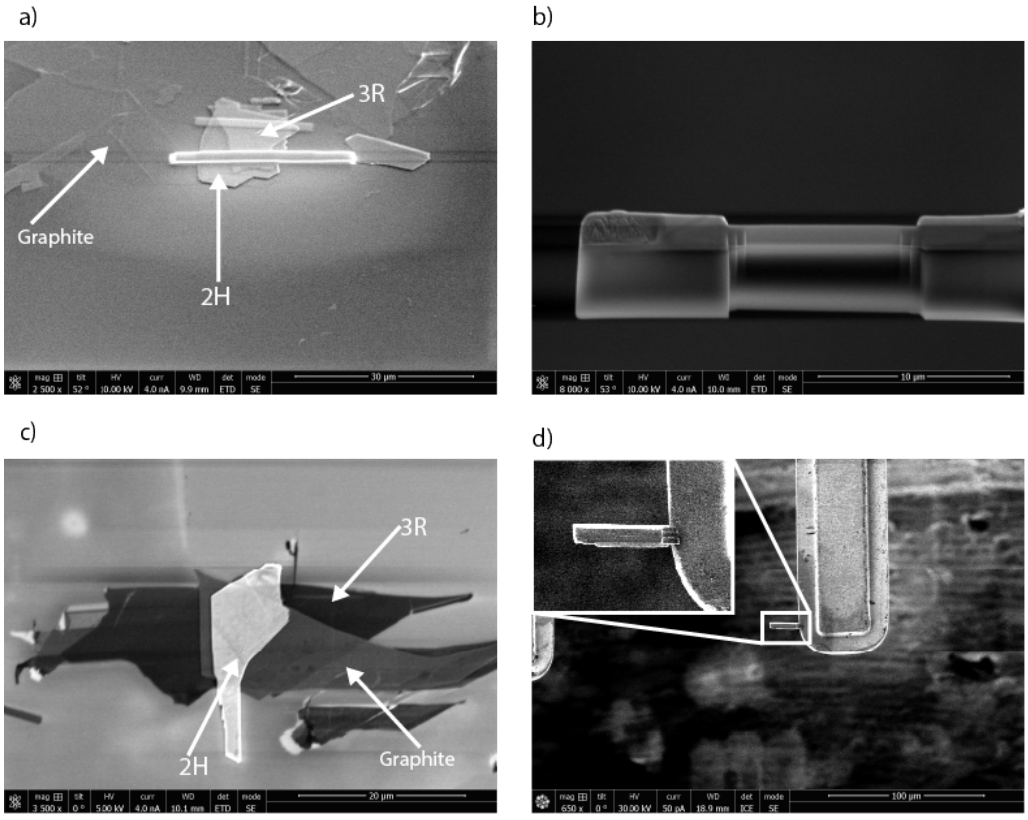

Figure 3.6: a) Flakes used for 2H3R_1 with protective platinum strip deposited. b) Finished cross-section 2H3R_1. c)Flakes used for 2H3R_3 with protective platinum strip deposited. d) Cross-section 2H3R_1 before final thinning.

3.3.2 DPC-STEM and tDPC-STEM measurement of MoS_2 Bulk Stacking Phase Induced Polarisation

The DPC data were captured using a convergence angle of 852 μrad and the tDPC data was captured using a convergence angle of 1 mrad. For both DPC and tDPC, the BF spot was enlarged and centred in the middle of the third circle. The gain for each detector was calibrated by imaging a standard sample consisting of gold nanoparticle and making the polarisation around the edges even.

The data analysis of the DPC and tDPC data was done by averaging the signal along the cross-section and marking the sections using the contrast from the DF and BF images. To confirm the correct labelling of the regions, Electron Energy Loss Spectroscopy (EELS) was used to identify the SiO_2 area and graphite area.

In Figure 3.7, a DF STEM image can be seen of 2H3R_1 with dots marking areas where EELS spectra where captured.

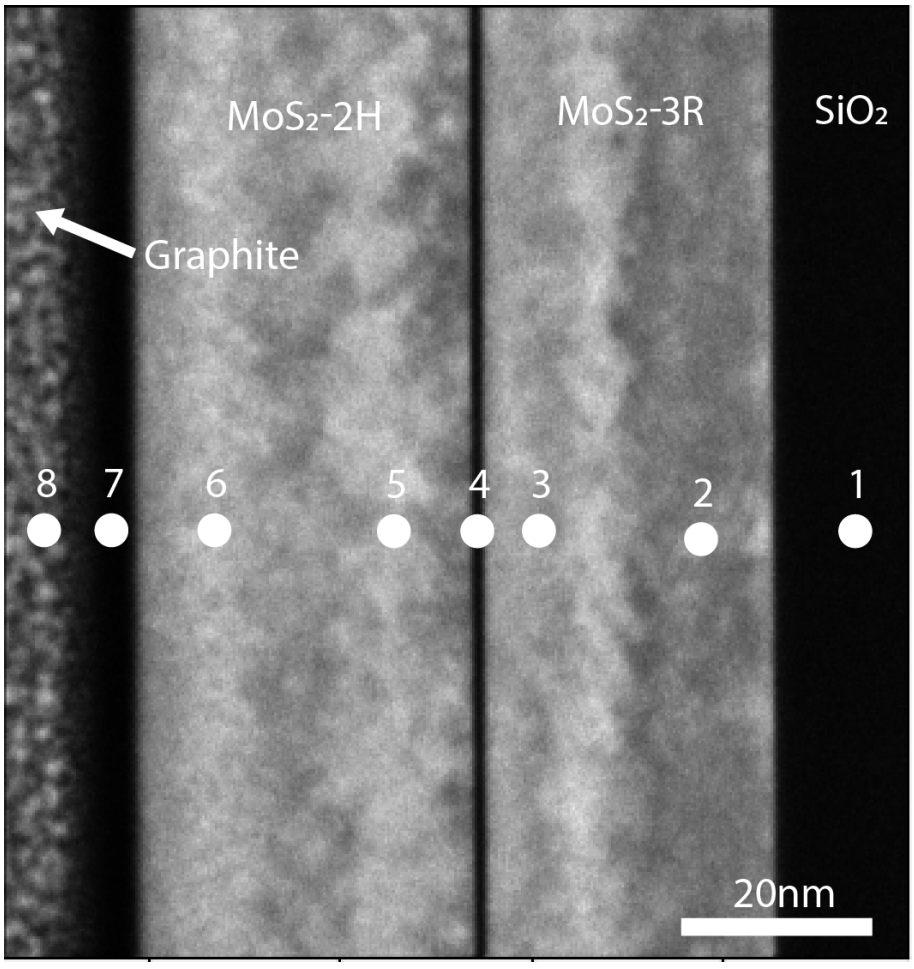

Figure 3.7: STEM DF taken of 2H3R_1. The dots marks where EELS spectra were gathered.

The spectra from these spots can be seen in Figure 3.8.

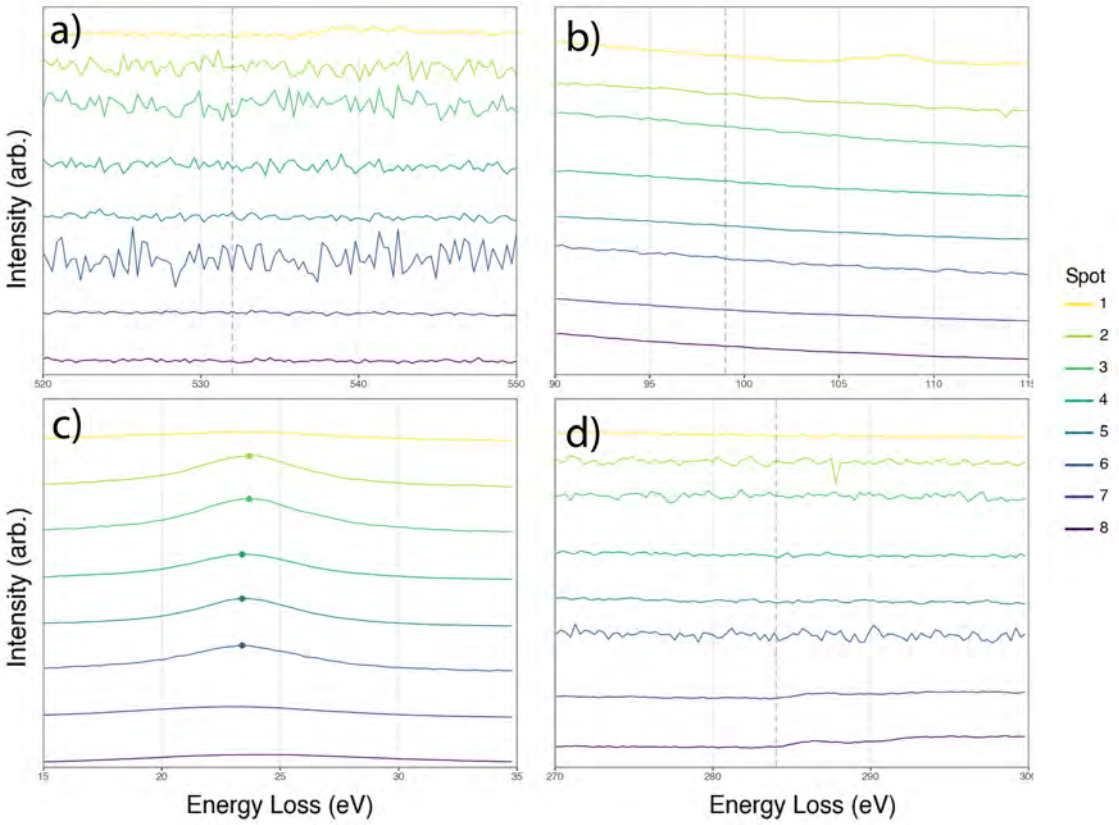

Figure 3.8: EELS spectra from the 8 points marked in 3.7. The spectra are numbered one to eight from top to bottom. The four images are from different regions in the EELS spectra. In the high loss spectra a),b) and d), gray dashed lines show the expected positions of the elemental edges.

Chemical EELS edges can be seen close to the elemental edges that was expected from the SiO_2 and graphite areas in the spectras presented in Figure 3.8. The elemental edges were not perfectly aligned with the expected energy loss. But as no other expected edges observable in this sample were closer to the ones observed, the misalignment was concluded to be due to calibration error. This was probably due to the High Loss-EELS spectra not being calibrated against the zero loss peak. With the stacking order of the flakes known, the regions could be identified. Supporting this information was the presence of a bulk plasmon at 23.4/23.7 eV, only visible in the MoS_2 regions. The bulk plasmon energy was different, 23.4 eV in MoS_2-2H and 23.7 in MoS_2-3R. This could be because of the difference in unit cell volume due to stacking. The difference in column between the 3R and 2H phases could have an impact on the valence electron density, which could have an effect the bulk plasmon energy[17]. This strengthened the labelling of the regions made from the stacking order and the elemental edges.

With the regions on the images labelled, the CoM shift in MoS_2-3R could be extracted. The extraction of CoM shift in the images was done by aligning the images along the y-axis and averaging all colons which yielded a line profile of the CoM shift. The MoS_2-2H region was used to normalise the signal. Then, the CoM shift

for MoS_2-3R was also plotted as a density plot using the non-averaged data and using the average value of the MoS_2-2H as a reference.

3.4 Instruments Used

A summary of all the instruments used for sample preparation and characterisation can be seen in Table 3.3.

Table 3.3: Instruments used for sample production and characterisation.

Instrument	Used for
Transfer Station	2D Flake Exfoliation and Stacking
WITec alpha300 R	Raman Spectroscopy and Cutting
Bruker Dimension 3100	AFM
FEI Versa3D	FIB-SEM
Helios G5	FIB-SEM
FEI Tecnai T20 LaB6	TEM
JEOL JEM-F200	TEM
Thermo Fisher Titan	STEM
JEOL ARM200F	STEM
JSM-IT810	STEM
JOEL JEM-2100F	DPC
MARS	STEM-tDPC

4

Results and Discussion

In this chapter, the results from this thesis is presented and discussed. First, the important aspects and details in the method to produce twisted structures is discussed. This includes a discussion on methods for producing good quality atomically thin flakes. Then, thickness determination of atomically thin flakes using optical microscopy is discussed. After which, the results from the Raman cutting technique and Plasma cleaning analysis is discussed. Parameters that effect stack quality and stacking success rate are presented as why they are important to control for high quality is then discussed.

With Moiré stacks of high quality, the results from the characterisation of the stacks is discussed. Starting with TEM DF imaging with Selected Area Electron Diffraction (SAED) patterns, showing the domain size and shape with diffraction patterns. Then, STEM imaging of stacked structures is shown with atomic resolution of anti-parallel stacked twisted structures. DFT calculations are then presented to investigate the energy distribution in structures found in the domain barrier. After which other observations found during S/TEM imaging is presented and discussed.

The chapter ends with presenting the measurement of possible out-of-plane polarisation measurements using DPC and tDPC and a discussion as if it is feasible to measure possible in plane polarisation of the domain walls in parallel stacked twisted structures.

4.1 Evaluation of Fabrication Method of MoS_2 Moiré Structures

In this section, the fabrication method used to produce MoS_2 Moiré explained in Section 3.1 structures is discussed. The explanation alone does not convey all the important aspects and reasoning behind the steps in the method. Therefore, this is discussed in this section. It starts with discussing the mechanical exfoliation of atomically thin MoS_2 flakes. Then continues with discussing the calibration of the thickness determination method to identify the number of layers in atomically thin flakes. The section continues with discussing the preparation technique using lasers to cut flakes. Finally, the section discusses important aspects and observations regarding the stacking process.

4.1.1 Mechanical Exfoliation for Producing Atomically Thin MoS_2 Flakes

The exfoliation method described in Chapter 3used to produce the flakes for the twisted structures was based on previous descriptions of mechanical exfoliation presented by Diez et. al.[18] but modified to increase the yield of thin flakes. There are many parameters in the exfoliation of flakes. Here, the most important are discussed.

One important parameter was the temperature of the silicon chip during the final peeling of the tape of the silicon chip. If the temperature was elevated above room temperature, a sharp reduction in total amount of flakes exfoliated was observed. Also, removing the pressure of the tape before cooling during the last heating cycle also appeared to reduce the amount of flakes exfoliated but not as drastically as the previous factor. Why this trend occurs is unclear and further investigation would be needed to establish an explanation.

The greatest refinement of the exfoliation method was the way of separation of the tape strips implemented. Most mechanical exfoliation is traditionally done by hand, contrary to this thesis, where this was performed using the transfer stage. This seemed to produce larger and thinner flakes more consistently compared to prying the tape strips apart by hand. A possible reason could be that the exfoliation using the transfer station is more repeatable, controllable, and does not apply any forces on the flakes that breaks them, resulting in smaller flakes.

Plasmas cleaning the chips before exfoliation seemed to increase the amount of thin flakes exfoliated. This could be because the surfaces are cleaner and this allows for better Van der Waals interaction between the chips and the flakes. It could also be due to the surface being slightly negatively charged, making the flakes stick better to the surface.

The cooking of the silicon chips before plasma cleaning was a minor improvement. The purpose behind this additional step was to remove any residual water that was residing in the chips, and chance creating a more electronegative surface, better for binding to the flakes. Removing the water would also prevent it from disturbing Van der Waals forces between the MoS_2 and silicon chip. However, no significant improvement was seen in performing this step.

4.1.2 Thickness Determination of Atomically Thin MoS_2 Flakes

The number of layers in the flakes used for the stacks was an important variable to quickly and reliably identify to allow for an efficient production method. To quickly select flakes with the right thickness for production of MoS_2 Moiré structures, a method to determine the thickness of atomically thin MoS_2 flakes using image contrast was developed. An image of a atomically thin MoS_2 can be seen in Figure 4.1.

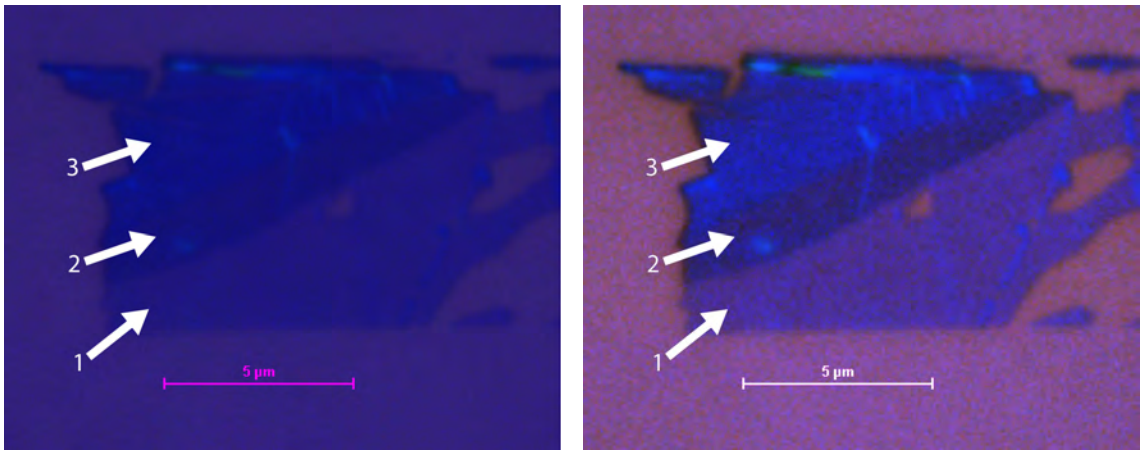

(a) Normal Contrast **(b)** Enhanced Contrast

Figure 4.1: Image of MoS_2 flake with regions of different thicknesses on 385 nm thick SiO_2 substrate. Arrows with numbers mark the thickness of the different regions.

As seen in the Figure 4.1, the colour can be hard to determine by eye. Therefore, the method was also needed to eliminate error from user bias.

To establish a ground truth, cross-sectional HR-TEM and Raman spectroscopy was used. Cross-sectional HR-TEM was used as this provides high spacial resolution and imaging of the individual layers directly. Raman spectroscopy was also used to complement the HR-TEM images and provided relative measurements for flakes not imaged using HR-TEM due to them being lost during the cross-section production. Raman is also a common way in literature to measure the number of layers in atomically thin flakes which allowed for comparison to other studies. AFM was also performed as this is also a common way in literature to measure the thickness of atomically thin flakes.

4.1.2.1 Cross-Sectional HR-TEM of 2D Flakes

The thicknesses of atomically thin MoS_2 flakes were measured using cross-sectional HR-TEM with an acceleration voltage of 200kV, Figure 4.2 shows some of the images used.

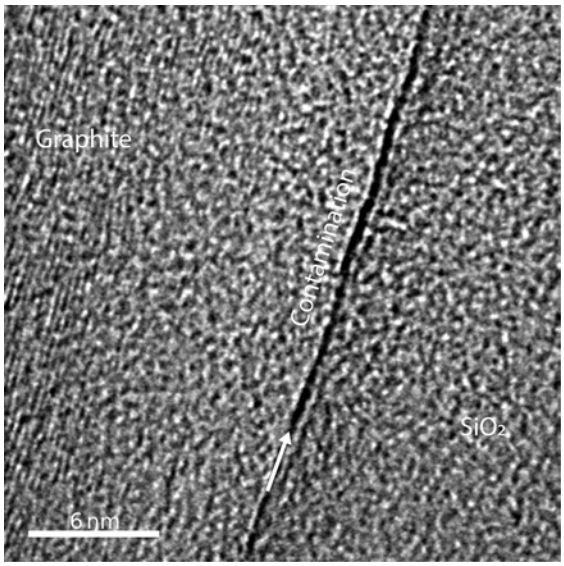

(a) Monolayer Flake

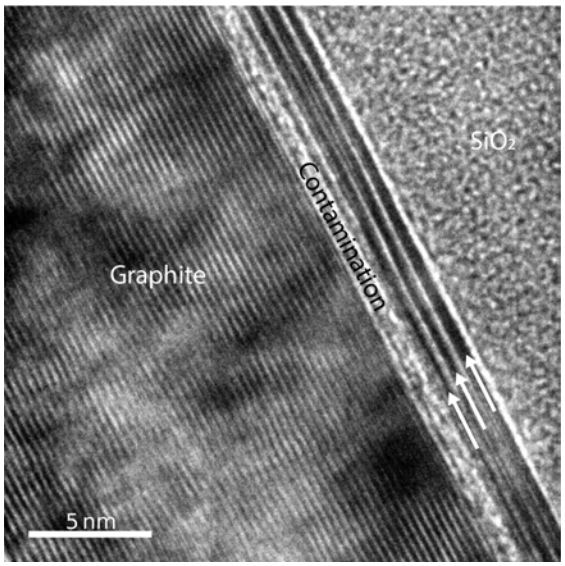

(b) Three Layer Flake

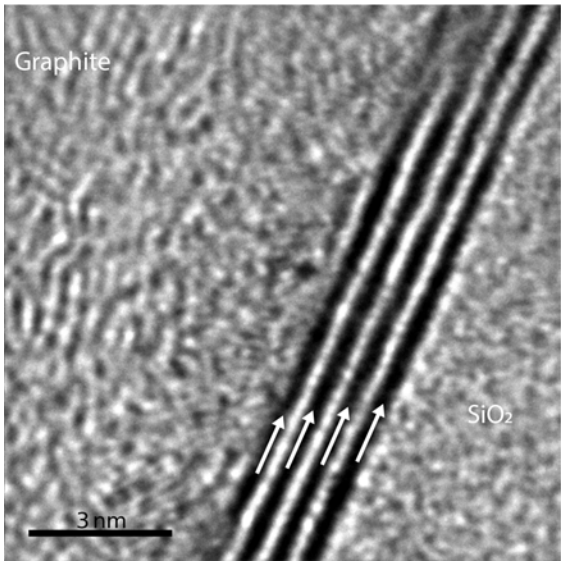

(c) Four Layer Flake

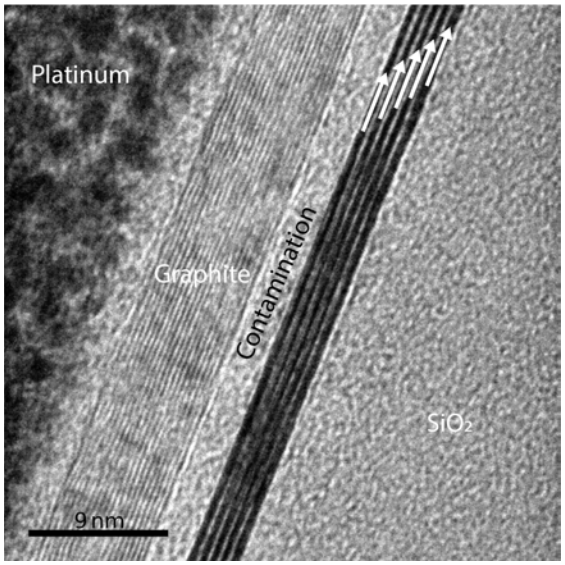

(d) Five Layer Flake

Figure 4.2: The Figure shows images of cross-sections of flakes used to calibrate the thickness determination. The parts in the images from the left are: graphite, contamination, MoS_2 and SiO_2. The platinum deposition can also be seen to the left in d). Note that b) is not the same flake used for the optical contrast but comes from a second measurement to confirm the measurement made with Raman spectroscopy.

In the images, graphite was used to protect the flakes from the platinum deposition visible in Figure 4.2d can be seen. To the right in the images, SiO_2 substrate can be seen. The MoS_2 layers can be seen marked with arrows. Between the graphite and the MoS_2 flakes, there is a amorphous layer present. This is likely contamination but the source is unknown. This contamination layer could be as a result from gathering dust or hydrocarbons in the environment and could be the reason why flakes attempted to be stacked days after exfoliation have a lower success rate as the

PC would not make as good of a contact with the flakes. However, this is speculation and would need further investigation to establish a conclusion. Due to this being BF TEM images, it can be hard to distinguish what contrast the layers are as this changes based on many parameter, focus being one of them. The monolayer image gives an indication as to what contrast we should be looking for. The monolayer in Figure 4.2a is seen as a dark line. As all images were taken in under focus condition, the same could likely be said for the other cross-sections as well. Another challenge with these measurements were that the cross-sections needed to be thin enough that the flakes did not bend along the beam direction, as this would make layers intersect in the cross-section images. Figure 4.2b shows bright contrasts in the dark layers, that can be attributed to cross-section sample being too thick. This probably comes from this cross-section sample being thicker than the other cross-sections. A way to fix this would be to further thin it down and image it again but due to time limitations and the supporting information of the Raman measurement, this was not done. STEM images of the cross-sections would be beneficial as they do not suffer from the same problem of having complex contrast and would make it easier to see the layers. Due to time limitations, this was not done.

4.1.2.2 Raman Peak Shift Measurement of Atomically Thin MoS_2 Flakes

Raman spectroscopy was used due to it being a faster and more common way to identify the number of layers in atomically thin flakes. Raman spectra where captured form all flakes present in two chips and later analysed by finding the peak position of the A_{1g} and E^1_{2g} peaks and measuring the distance between them. The measurement can be seen in Figure 4.3.

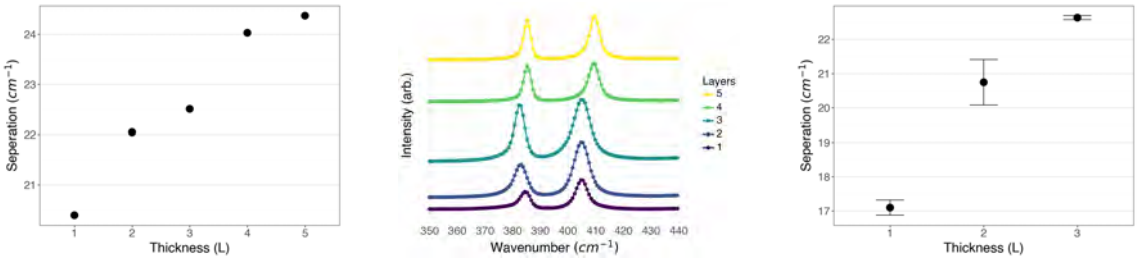

(a) Chip 1 **(b)** Chip 1 spectra **(c)** Chip 2

Figure 4.3: Raman peak separation of $\mathbf{A_{1g}}$ and $\mathbf{E^1_{2g}}$ depending on thickness. a) is Chip 1 and b) is Chip 2. Chip 2 only had three flakes measured and thus only have 3 data points shown in the plot. The error bar shows the maximum and minimum values estimated during the fitting.

Some differences and similarities can be seen between the measurements of the chips. The similarity between Chip one and two is that there is a trend that the thinner the flakes get, the smaller the peak separation. This trend has previously been observed, but the absolute values are different from literature [19][20]. Previous measurements in literature used 515.4/532 nm [19][20] laser which is similar to this thesis which used a 532 nm laser, so this is unlikely to be the cause of the difference. A possible explanation for the difference between Chip 1 and 2 could be that the initial mea-

surement of Chip 1 used an intensity of the laser that was too high and damaged some parts of the flakes and could change the flakes properties locally. (These areas were avoided in the manufacturing of the cross-sections.) Measurements for Chip one had a higher intensity than Chip 2 which could make the signal to noise ratio being better for Chip one than Chip two. This could make the peak fitting harder to perform and result in errors. Crystal defects could also be a reason that the peak position is not the same between measurements.

Due to the discrepancy of the absolute values of the Raman separation between flakes with the same thickness, the Raman measurements were not used directly as measurements of the thickness. The Raman results were used to relate the flakes not imaged directly with HR-TEM, to the flakes that were directly imaged with HR-TEM

4.1.2.3 AFM Measurements of Atomically thin MoS_2 Flakes

AFM measurements were made to complement the other thickens determination techniques as this a common way in the field to measure the thickness of 2D material flakes. The results of the AFM measurements can be seen in Figure 4.4.

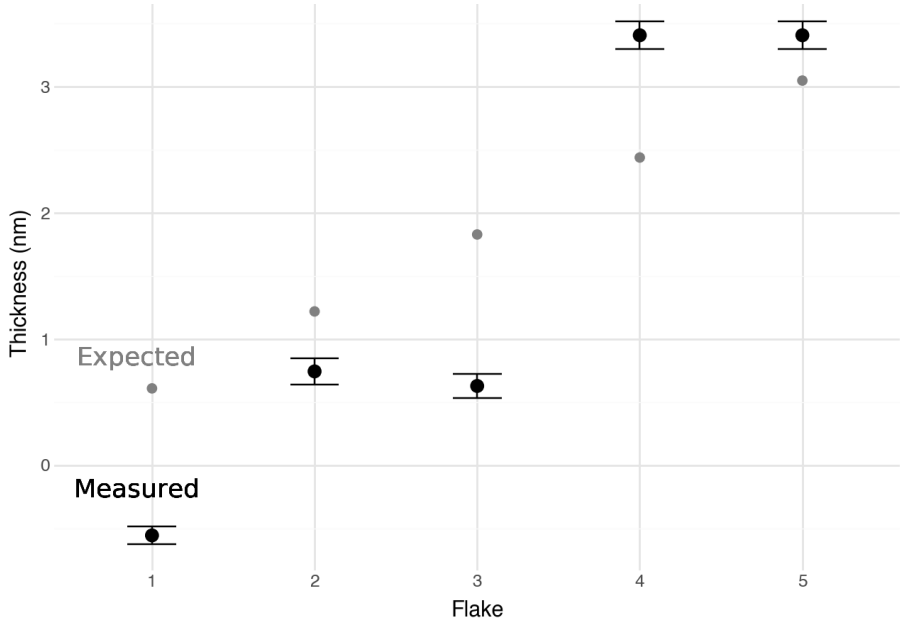

Figure 4.4: AFM results from measuring the thickness of MoS_2 Flakes. Expected thickness of the the flakes with different number of layers can be seen as gray points. These were calculated from each layer being 0.61/ : nm thick.

The data from AFM did not agree with the other measurements made and with how thick the layers should be from theory. In Figure 4.4, we see that most data points are lower than the expected value expect for four and five layer flakes which were higher. This could be because of a wide range of effects but one that could be affecting is the contamination built up on the surface visible in Figure 4.2. The contamination could interact with the AFM needle in a different way than the MoS_2

and SiO_2 which would affect the signal. These results were not used for the optical thickness determination model due to them not agreeing with other measurements and to many sources of error.

4.1.2.4 Optical Contrast Measurement

The optical measurements results are presented in Figure 4.5a. In the figure, the values of the different colour channels in the image can be seen and the layers are distinguishable from each other by comparing the intensity of the channels. Some variation of the intensity was observed between flakes of the same thickness, these results can be seen in Appendix Chapter B. This could be due to the flake having bends, cracks and patches missing which changes the colour. It could also be that the flakes were affected by the environment and thus changed colour. But this could also be a result from errors in the measurement of the flake. One culprit could be that the intensity of the light source is not the same everywhere on the flake. This creates a variation in the measurement if the exact same spot is used every time. During these measurements, all flakes were not imaged at the same position under the microscope objective which could affect the signal intensity as there were a intensity variation across the field of view. But all flakes were measured close to the centre in the field of view which should mean that the affects from the intensity variation should not be severe. The variation in intensity was discovered after the flakes used for this calibration had already been used for fabrication of cross-sections and could thus not be re-analysed. The same location was always used after this was discovered.

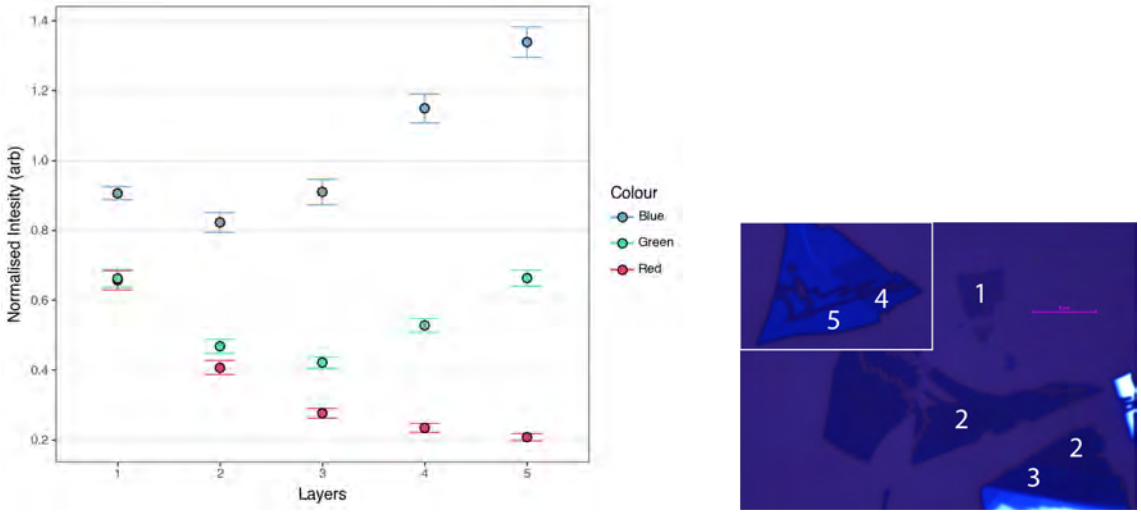

(a) Optical contrast **(b)** Image of flakes

Figure 4.5: a) Optical model obtained from MoS_2-2H. The error bars show the standard deviation of the data in the line profiles. b) MoS_2 flakes used for the optical contrast. The numbers in the image represent the number of layers of each flake.

The thicknesses of 1,4 and 5 layers was confirmed using TEM analysis of cross-sectional specimens of the 2D flakes. The thicknesses 2 and 3, however was lost in the fabrication process. Raman was used together with the cross-sectional HR

TEM images to confirm these thicknesses. TEM images together with Raman results was considered good enough for identification of the flake thicknesses during the manufacturing but for better confidence in the results, STEM measurements observing cross-sections of flakes that have been measured using the same position in the optical microscope would be beneficial.

Looking at the trend for the image contrast in the images, more and more light is absorbed by the flakes as the intensity decreases with decreasing amount of layers for blue and green channel. But for the red channel and the green and blue channels below three layers, the intensity increases again. The same trend seen in the blue channel as the green and red is different compared to previous measurements [20]. Why there is a difference between the other measurement and this one is hard to say and would need more investigation to understand.

4.1.3 Laser Cutting and Plasma Cleaning

Shaping and cutting of parts of flakes is an important tool for precision staking of 2D flakes. Therefore, it was of interest to see how much damage laser cutting did to the MoS_2 flakes. In this section the damage induced from cutting the flakes with a laser is presented. First, flakes with a thickness of $20 - 50$ nm were investigated. Figure 4.6b shows an image of the typical damage present in the thick flakes.

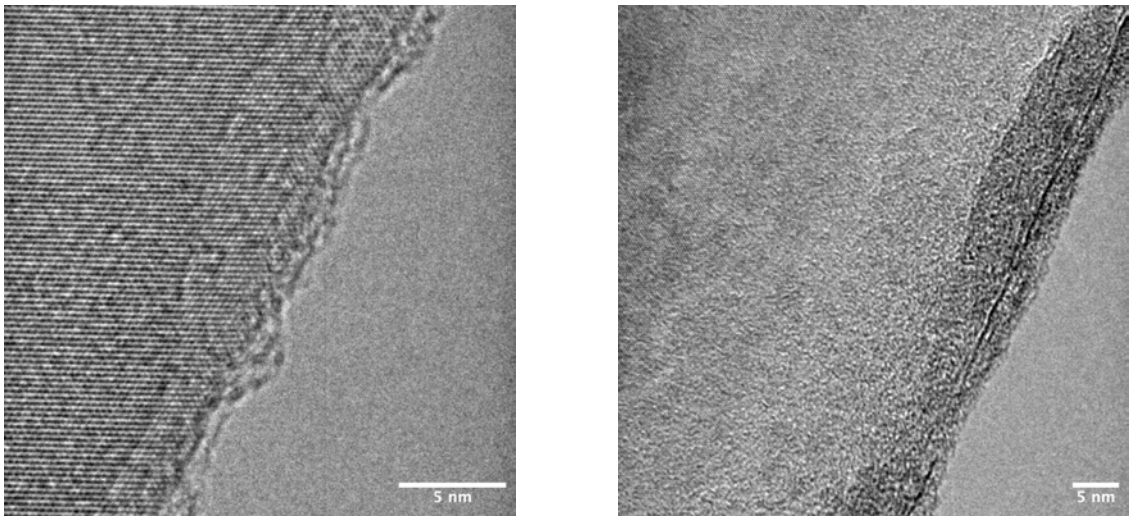

(a) Normal **(b)** Damaged

Figure 4.6: a) Normal thick flake. b) Damaged flake where an amorphous layer is present. The atomic columns in b) is not as clear as in a), this is likely due to the flake in a) being angled closer to zone axis rather that damage from the laser cutting.

As seen in the Figure 4.6b. An amorphous layer, $5 - 10$ nm wide, is created after laser cutting. This is probably due to thermal effects from the heat applied by the laser. For the thin flakes, the damage was similar but smaller with an amorphous $2 - 5$ nm at the edge. Typical laser induced damage on thin flakes can be seen in

Figure 4.7b.

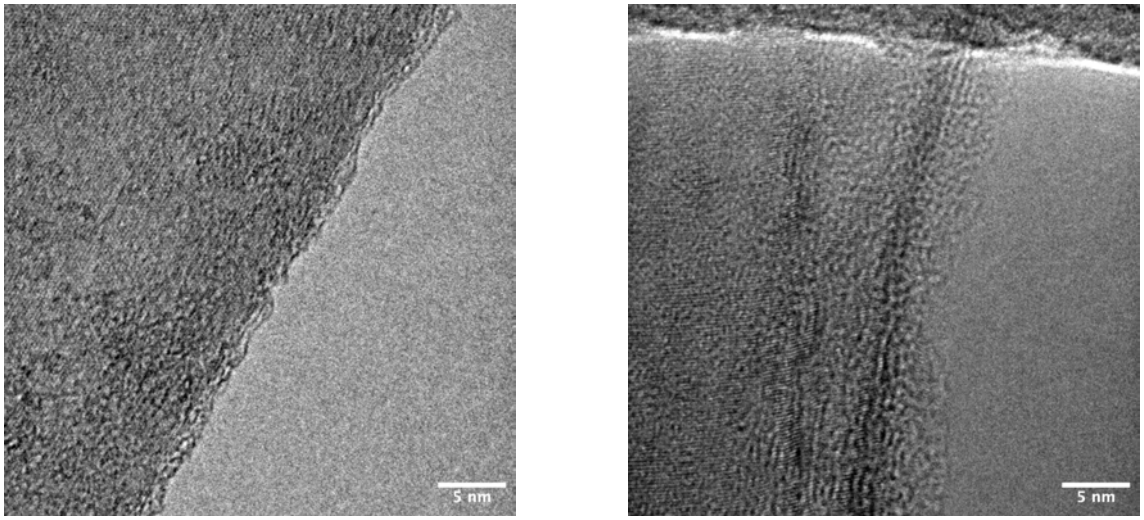

(a) Normal **(b)** Damaged

Figure 4.7: Image a) shows a normal thin flake. Image b) shows the damaged thin flake where an amorphous layer is present.

An interesting comparison between thick and thin flakes is that the thick flake without laser damage, seen in Figure 4.6a, has an amorphous layer $1-3\,\text{nm}$ thick present on the edge. Where as the thin flakes, seen in Figure 4.7a shows almost no amorphous layer present on the edge. This could be due to the thick flakes having a staircase structure, allowing amorphous material to accumulate on the surface, but the lack of any signs of crystallinity in the amorphous region makes this unlikely. A more likely reason is that the thick flakes edges having a larger surface area, more amorphous material can attach to it than thin flakes with edges with smaller surface area. Both thick and thin flakes showed little damage from the laser to the atomic structure of the molybdenum atoms. These results do not show the damage to the sulphur atoms so the total extent of the damage is hard to estimate from these pictures alone. But, as the damage to the molybdenum was small relative to the microns size of the samples and therefore laser cutting was deemed safe to use in the preparation of the samples for the rest of the thesis.

Plasma cleaning was done for 20 seconds with 4% oxygen argon gas. Plasma cleaning of the flakes showed damage to the atomic structure of the flakes. The damage was especially present in the thicker flakes. Figure 4.8b shows the typical features of plasma cleaning damage.

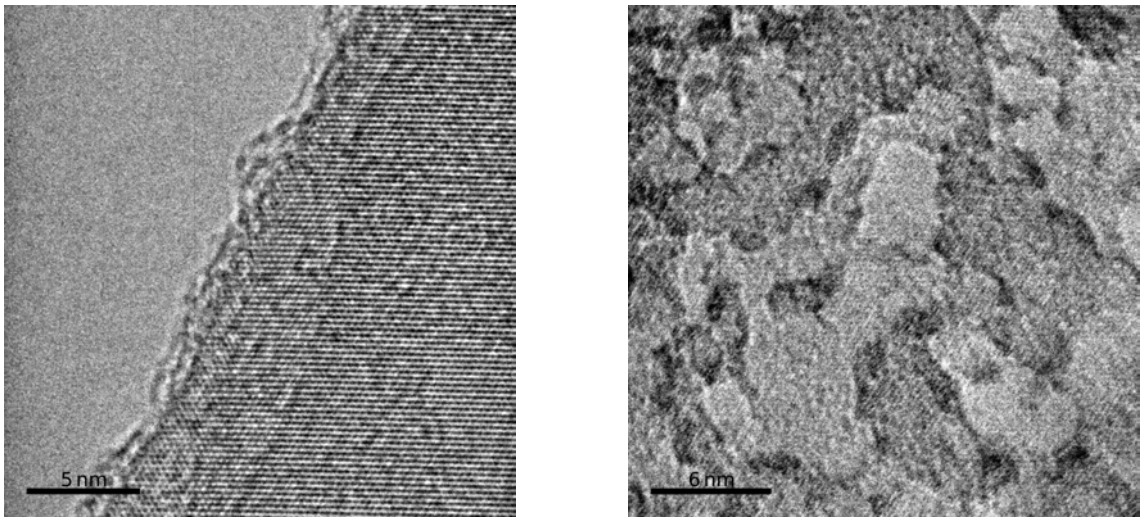

(a) First image **(b)** Second image

Figure 4.8: a) Reference image of free-standing MoS_2 flake. b) Image of free-standing MoS_2 after 20 seconds of plasma cleaning. The atomic columns not being as present in b) does not have to be because plasma cleaning but could be due to the image being taken of zone axis or astigmatism.

Flakes with plasma cleaning damage showed dark and light contrast present in the surface. Exact cause why this happens would need further investigation.

4.1.4 Fabrication 2D Twisted Structures by Stacking

Twisted-bilayers and other structures is shown to be manufactured using the method described earlier in the thesis. Here, important aspects during the manufacturing process, flake properties, temperature, angle of the glass slide relative to the substrate, angle of approach for the wavefront and production of PC stacks, is presented.

The exfoliation method developed during the thesis showed to reliably produce at least one 3 μm^2 monolayer flake per 1 cm^2 chip. However, not all flakes produced were suitable for stacking. Larger uniform flakes worked better for stacking, so flakes that had multiple cracks or were less than 4 μm across its shortest edge were discarded. It was also observed that it was important to pick up the largest flake first. When attempting to pick up a larger flake with a smaller flake, the contact area was probably too small, thus the force pulling the second flake was not bigger than the force holding the larger flake down to the substrate, leaving it on the substrate.

Temperature of the vacuum chuck was an important parameter when stacking. When picking up the first flake, 75°C worked the best. This was because the temperature was low enough that the PC would not be to sticky and get stuck on the substrate, making the wave front jump forward in steps and become unpredictable. But the 75°C was still hot enough to make the PC sticky enough to pick up the first flake. If the flake was not picked up, a second attempt could be made with an unused part of the PC. But instead of lifting up the flake with 75°C, the temper-

ature could be increased to 85°C and then picked up. This worked on some flakes but doing so risked moving the wavefront further forward likely due to the PDMS expanding. This was compensated by moving the glass slide upward while heating to 85°C, keeping the wavefront locked in the same position. The second pickup most successful when using 85°C as the high control of the wavefront was not as critical, due to the second flake being isolated, and the pickup of the second flake was observed to be more successful when using higher temperature. This could be due to the contact between the flakes where more uniform from the higher pressure being applied and PC becoming softer and conforming to the stack better. Temperatures higher than 85°C was not used during the pickup process because the PC was observed becoming to soft and stretching or even breaking during the pickup process.

The quality of the PC stacks was an important parameter to control. When the PC stacks were produced, the uniformity was checked. It was observed that using PC stacks with wrinkles made the pickup unpredictable as the PC could stretch and move during the pickup. In producing the PC stacks, it was observed that the brand of tape had an effect of the quality. Having fresh PC film was also observed to be important. Using PC film older than 3 weeks for the PC stacks resulted in very few flakes being picked up. Making new PC film improved the performance of the PC stacks to picking up nearly all flakes. The area of the PC stamp that had been in contact with the substrate was observed to not be as successful at picking up flakes. As a solution to this problem, fresh part of the PC stack was used or it was discarded. Flakes that had been in contact with the PC was observed to be contaminated, this can be seen in Figure 4.23. The contamination probably contributed to the observed behaviour that a flake that was not picked up during the first attempt, was rarely pick up during proceeding attempts. This meant that multiple attempts at picking up a flake was not viable and after an attempt had been made and was unsuccessful, the flake would be discarded.

The angle of the glass slide relative to the substrate was important for the behaviour of the wavefront. If the angle was too small, the wavefront would move to quickly to reliably control the position were it would stop in the flake during the pickup of the first flake. Having a too high angle would make the wavefront front jump forward in steps and become unpredictable, similar to having a too high temperature. A pitch and roll of 4.5° was deemed as the optimal settings during the production process. However, when depositing the stack on a TEM grid, a lower angle would sometimes be needed to reach the grid with the glass slide and not break the grid, especially important for the 5 nm continuous SiN grids. The faster wavefront was not a problem here due to the high accuracy of the wavefront not being critical for this step. The optimal setting was found to be $1.5 - 2°$ of pitch and roll.

Another important development of the transfer process for the behaviour of the wavefront was the implementation of the jog movement to stop the wavefront. Probably due to the PDMS being soft, when the movement of the glass slide is stoped, the wavefront does not always stop immediately. The wavefront continued $1 - 5\,\mu$m

which often led to failed stacking. By jogging the glass slide upwards, the pressure on the PDMS was released enough to stop the wavefront but not too much to retract it. This prevent extending the wavefront nearly entirely.

Which side to approach the flake was a helpful parameter to optimize during the pickup process. The majority of mono- and bilayer flakes exfoliated were close to rectangular. To optimize the success rate, the flake was always approached on the short side. This provided a longer area to move the wavefront over, making the optimal area to stop the wavefront on larger and easier to hit. It was also observed that pickups of flakes was more successful when approached this way. If the flake was triangular, it was observed that approaching the flake on the base was more successful, this could be because the flake pealed away from the substrate easier at the tip compared to the base. The base has initially higher surface area in contact with substrate when the PC tries to lift it of the substrate. Having a smaller initial surface area could decrease the forces holding on to the flake relative to the force trying to pull it up, making the pickup process easier to start.

A difficult problem to overcome was to see the monolayer flakes after pickup. The thinnest flakes were hard to see in the substrate and became transparent after pickup. To aim the wavefront and flakes, triangulation using thicker nearby flakes was used. During pickup, when the wavefront made contact with the flakes, the flakes became visible again. This made the final positioning of the wavefront on the flake easier but the second step of stacking the flakes on top of each other was still difficult but possible with triangulation based on features in thicker flakes surrounding the target flake.

4.2 Characterization of MoS_2 Moire structures

In this section, the characterisation of MoS_2 Moire structures is presented. The stacks produced were of two types, parallel stacking, when the alignment of the MoS_2 molecules in the layer at the interface was the same, and anti parallel, when the alignment of the MoS_2 molecules in the layer at the interface was reversed. A complete list of samples used can be found in Table 3.2. For the parallel stacked twisted structures, bi-bi and mono, stacks were used. For the anti-parallel stacked twisted structures, only bi-bi stacks were used due to time constraints.

The section starts with discussing the characterisation of parallel stacked structures, presenting TEM, STEM images and SAED patterns showing domain structures and possible polarisation effects. Then, the section continues with discussing the characterisation anti-parallel structures, presenting TEM, STEM images and SAED diffraction patterns showing domain structure and atomic structure of the domain walls. DFT calculations for the energy distribution in the domain walls is also be presented. The section ends with presenting other observation not directly relating to the Moiré domain structures.

4.2.1 Parallel Stacked Twisted Structures

Parallel stacked structures were analysed using DF-TEM imaging. In this part, the structure of these are presented and possible effects affecting the shape of the domains as well as imaging mechanisms resulting from the atomic structure in the domains is discussed.

4.2.1.1 Twisted mono-mono Stacks

During imaging of the parallel stacked twisted bilayers, all samples showed heavy bright and dark contrasts which is discussed later in this section. However, some parts did not show this contrast, but other patterns. One of these patterns can be seen in Figure 4.9.

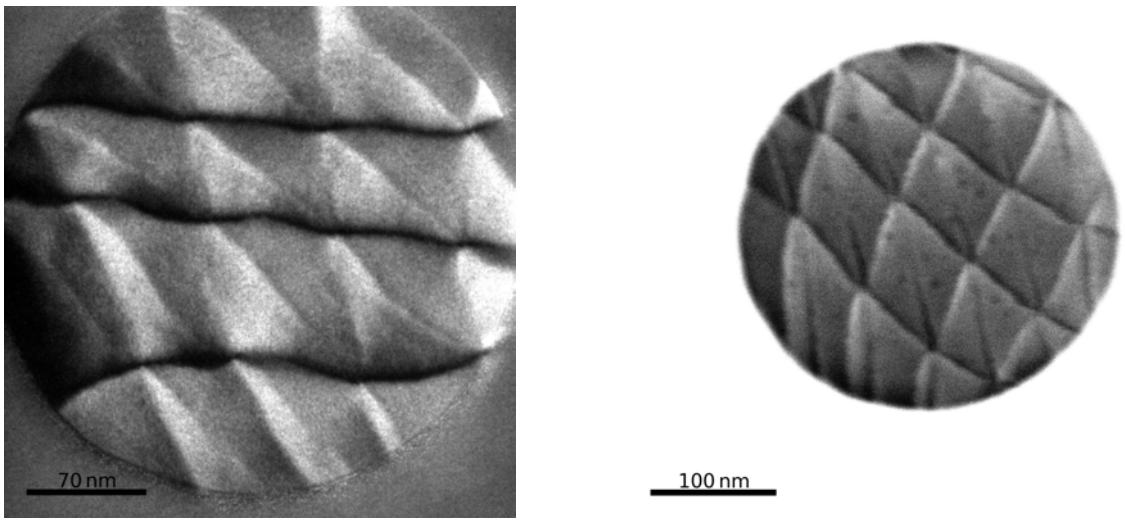

(a) DF **(b)** HAADF

Figure 4.9: a) DF image of parallel twisted mono-mono stack on a SiN TEM Grid with 300 nm holes. b) HAADF image of the same hole as a). Both images is from the same hole on PL3.

In Figure 4.9, one DF image and one HAADF image can be seen. In the DF image, bright and dark triangles are present with black lines going horizontal across the image. The bright and dark regions show domain structure and the bright and dark contrast could be from the stacking in the different domains being different. This is discussed more in Figure 4.10. The HAADF image of the same area shows again the triangular domains but in this image the domains have similar brightness with the walls having a darker contrast. This could indicate that the domains scatter electrons to a higher angle than the walls which could mean that the walls have a lower density of atoms as the mass of the atoms are the same in all parts of the sample.

The patterns look similar to parallel stacked Moiré structures that have undergone relaxation that can be found in literature [21], which indicates that these patterns are Moiré structures as well. Looking closer at the patterns, there are some trends

that can be found. The triangular patterns have different size and shape between holes, not being very regular across the whole region. This could be because the fabrication applies too much stress on the flakes and is not consistent enough to make large homogenous moire patterns consistently. It could also be because the flakes are free-standing, strain is applied which changes the shape of the domains. Uneven strain, for example from the flake buckling differently between holes, would give rise to different shape of the domains.

Looking at the dark field signal coming from the domains, the contrast changes depending on which DF spot is used for imaging. This can be seen in Figure 4.10.

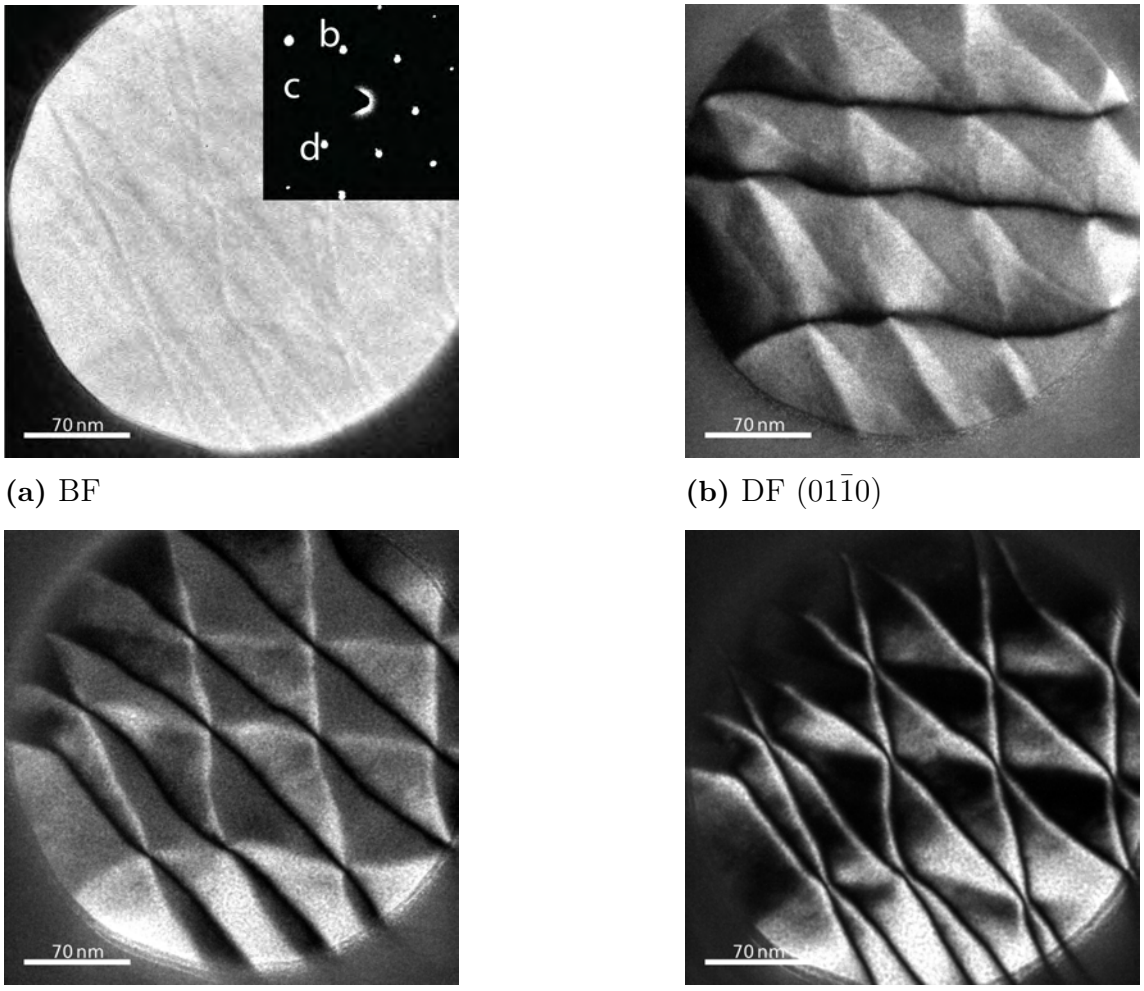

(a) BF

(b) DF $(01\bar{1}0)$

(c) DF $(\bar{1}010)$

(d) DF $(\bar{1}\bar{1}20)$

Figure 4.10: a) BF TEM image with SAED in the top right corner. b-d) DF images from different diffraction spots. All images are captured from the same hole on PL3.

In the images in Figure 4.10, there are bright and dark triangles with lines between them present in the DF images. The difference in brightness suggests that there is a difference in the crystal stacking in these areas. For a moire pattern with parallel stacking, this difference could be the difference between XM and MX stacking. The

black line appearing at the domain walls, changes direction depending on the diffraction spot chosen for DF. This could also be as a result from the atomic stacking in these walls. Another interesting observation about the walls can be seen Figure 4.10d. The bright and dark contrast at either side of the domain barrier is more present than in the other images. Looking at the bright contrast, it can be seen that it follows the under side of the barrier, even when the domain type switches. This could be due to either that the stacking at the barrier results in the same contrast for both domains, and possibly be similar in structure. Or, that the stack is bending at the domain barrier and the contrast is due to bending from change in atomic structure.

Something to note in Figure 4.10d is that the alternation of the dark and bright contrast stop close to the edges of the bottom and top parts of the hole. This could be as a result from the flake bending and changing the crystal orientation relative to the beam. This could also explain the shape of the domains changing at the edges of the hole. But confirm this, simulations and more advanced techniques would be needed.

Before moving on from this area, the diffraction pattern has interesting features to be discussed. In Figure 4.11, the diffraction pattern from the area shown in Figure 4.10 can be seen.

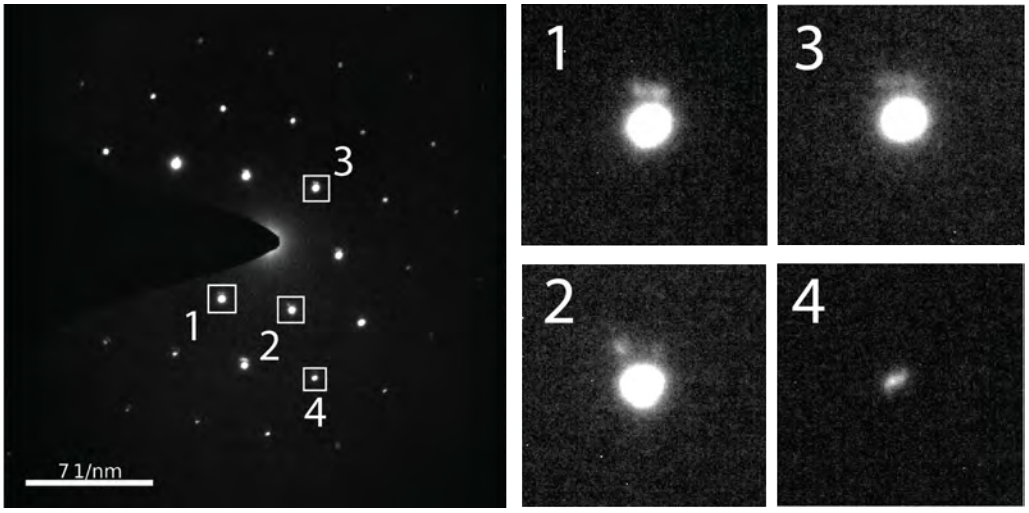

Figure 4.11: SAED diffraction patterns from the area shown in Figure 4.10d. To the left are some spots that are magnified. Spot number one is the $(\bar{1}\bar{1}20)$ spot. Spot number two is the $(0\bar{1}10)$ spot. Spot number three is the $(11\bar{2}0)$ spot. Spot number four is the $(0\bar{2}20)$ spot.

In the diffraction pattern. Main diffraction spots can be seen and appear to be elongated, more visible in the higher order diffraction spots such as picture four in Figure 4.11. This could be because the diffraction spots from the two monolayers overlapping due to the high intensity and the small twist angle ($0.1°$) between the monolayers. But for the lower order diffraction spots, extra spots can be seen close to the main spot. These extra spots appear to be on the same side for all

diffraction spots. This makes it unlikely that the spots are from periodic lattice distortion as these diffraction patterns are symmetric. An explanation could be that in-plane electrical polarisation present deflect the diffracted electrons, creating a new weaker spot [22]. If the spots are due to polarisation, the polarisation is likely to be from the domain walls as the polarisation in the domains should only be out of plane. The three extra dots in this case could be explained by the domain walls having slightly separate direction of the polarisation. As there are only three main directions for the domain walls, a maximum of three dots should be visible. However, not all diffraction spots have three extra spots. Some spots only have one or two extra spots. This could be due to the structure not being completely homogenous, changing the intensity and direction for the spots resulting from polarisation. Using the splitting, the possible electric field strength can be calculated using the formula

$$E = \frac{\gamma p^2}{em^* t} \tag{4.1}$$

where E is the electric field, γ is the deflection angle of the beam, p is the momentum of the electrons, m^* is the relative mass of the electrons and t is the sample thickness. The field in the domain walls would be $0.395 \pm 0.045 \frac{\mathrm{V}}{\mathrm{nm}}$. Further investigation combining piezo force microscopy and TEM would be interesting to establish if this is due to polarisation or other effects[23].

Smaller suspected Moiré domains were also imaged in another sample using HAADF, these images can be seen in Figure 4.12.

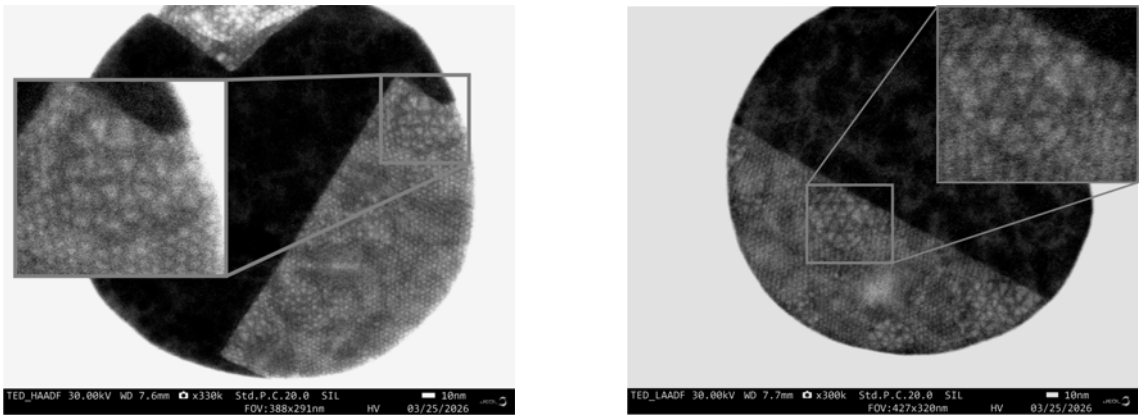

(a) Area 1 **(b)** Area 2

Figure 4.12: a) HAADF STEM image from area one on PL6 with possible Moiré patterns. b) LAADF STEM image from area one on PL6 with possible Moiré patterns.

In these images, areas with triangles can be seen. These are the areas with the twisted bilayers. These HAADF and LAADF images show the same trend as the HAADF images in Figure 4.9 with the domains being brighter than the walls and not being very regular across the sample. A dark and bright contrast can also be seen were there is only monolayer present. This dark and bright contrast could be contamination and could also be affecting the Moiré pattern.

4.2.1.2 Twisted Bi-Bi Stacks

One bi-bilayer stack was created with parallel stacking. TEM imaging showed that this sample suffered the same problem with strong suspected corrugation contrast, but some areas showed Moiré domain structures. In Figure 4.13 the images gathered from this area can be seen.

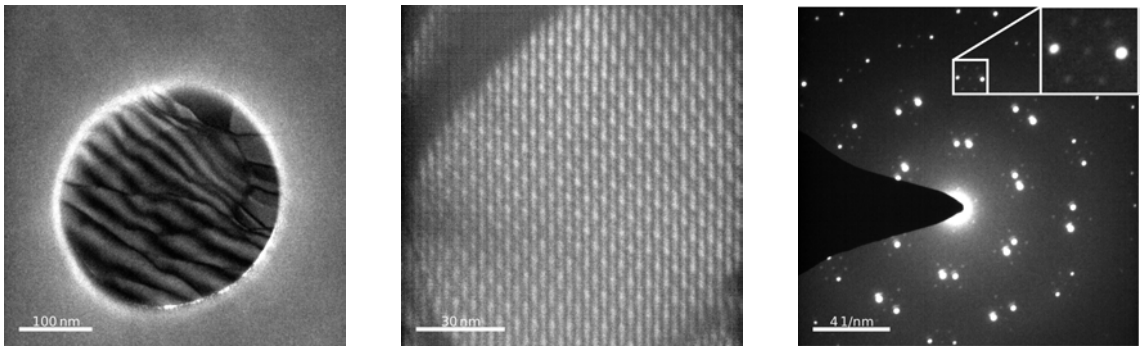

(a) Area 1 **(b)** Area 2 **(c)** SAED Area 2

Figure 4.13: a-b) DF TEM images with possible Moiré patterns present on PL16. c) SAED pattern taken from Area two.

In Area 1 in Figure 4.13, bright and dark lines can be seen. These are suspected to be corrugation and is discussed in Section 4.2.3.1. At the top right part of the hole, a possible Moiré pattern can be seen with some domains visible. However, to confirm that this is a moire pattern, a larger area of this pattern would be optimal. In Area 2 in Figure 4.13, possible Moiré structure can be seen. The domains in this image are very small and due to imaging conditions, there shape is not fully resolved. Looking at the diffraction pattern from this area can help is interoperate what the image could depict. Looking at the diffraction pattern in Figure 4.13, two main diffraction patterns from the two bilayers can be seen. These are the brightest spots visible in the diffraction pattern. Close to these are darker spots seen in the zoomed region in Figure 4.13c, these darker spots could be double diffraction spots. But as they are symmetrical around each pair of bright diffraction spots and not radiating out from one of them, this is unlikely. Therefore, it is more likely that these comes from periodic lattice distortions similar to effects seen in twisted bilayer graphene [7] and would suggest that the image in Figure 4.13b is indeed a Moiré pattern. But to establish this, better images with higher magnification would be needed. Why the extra spots are visible in this SAED pattern and not in the SAED pattern in Figure 4.11 could be due to the difference in twist angle.

The stack in Figure 4.13c has a high twist angle of 6° measured from the diffraction pattern. This makes the domains smaller and more atoms in the image would undergo periodic lattice distortions, making the diffraction spot from them stronger compared to smaller twist angels that would produce fewer walls and therefor fewer atoms that gets effected by periodic lattice distortions. Using the equation 2.1, the domain size should be 3 nm for a twist angle of 6°. This is hard to confirm in Figure 4.13b due to the low spatial resolution but looks to be close to the same size as

predicted from the twist angle.

4.2.2 Anti-Parallel Stacked Twisted Structures

Anti-parallel stacked structures were analysed using DF TEM imaging, HAADF STEM at 80 kV and 30 kV and BF STEM at 30 kV. The energy of the different parts of the systems observed using HAADF STEM at 80 kV were investigated by calculating the energy of select parts with DFT. From these measurements, the effects on shape and size of the domains were discussed and kinds of domain walls were also discussed.

4.2.2.1 Twisted Bi-Bi Stacks

Three of the twisted Bi-Bi stacks produced showed areas with possible Moiré patterns. Two of these can be seen in 4.14.

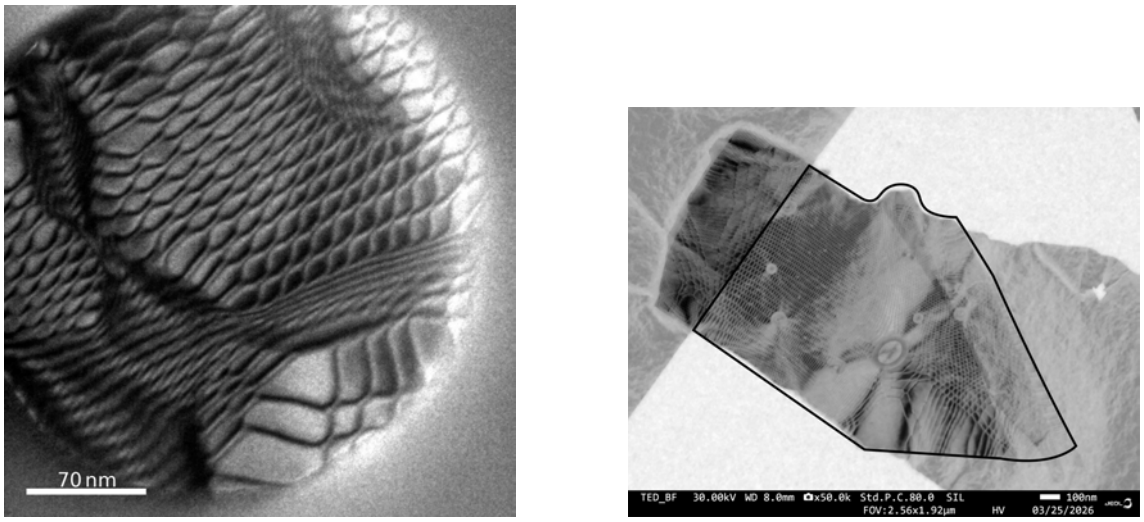

(a) PL14 **(b)** PL2

Figure 4.14: a)DF TEM image of PL14 on 300 nm SiN window with 300 nm holes. b) BF STEM image of PL2 with the area with two bilayers stacked marked with a black outline. Courtesy of JEOL Ltd. for providing the image.

In figure 4.14a, a DF TEM image can be seen taken of a bi-bi stack with 0.1° of twist on a 300 nm SiN window with 300 nm holes. In the image, there are irregular hexagonal features which show domains surrounded by domain walls. There are also wavy features breaking up the hexagonal pattern. These features could be bending of the flake. The wavy features often in this image have a dark contour which could be bending contrast and therefore suggest that these could be bends in the flake which would also change how the two bilayers align relative to each other and therefore change the appearance of the Moiré structure. The domains shape changes throughout the image, even in the same pattern area. Bigger change of the shape was also seen between holes surrounding the one showed in the figure. The pattern reaching from the middle to the top of the image has its domains becoming more elongated further up in the image. The elongation could be due to strain being

applied from both the flake being bent from being stretched over the hole, but could also be from the bends in the flakes to the left and right of the area. This is also a feature that could be observed in Figure 4.14b.

In Figure 4.14b, a BF STEM image can be seen taken of a bi-bi stack on a 5 nm continuos SiN window. In the highlighted area, possible Moiré patterns can be seen as irregular hexagonal patterns. The biggest bubble free area is 0.4 μm large. The Bubbles are likely from the stacking process and can be seen as round bright features. The dark and bright contrast surrounding the bubbles are likely bending contrast as the flakes would most likely be bent from the bubbles. We can also see that the size and shape of the domains are different in left and right side of the image. Looking on the left side of the image, the shapes appear to be more regular and consistent with the bending contour here being more stable. On the right hand side, the shapes changes size and shape more and there is more bending contrast present. This could be again that the shape and size of the domains are affected by the bending of the flake. It seems that to produce large area regular patterns, minimising the bending is an important factor. Using continuos film could help making better Moiré structure by eliminating the bending the flakes experience from being suspended over the holes.

4.2.2.2 HAADF-STEM of Twisted Bi-Bi Stacks

Two regions were selected for atomic resolution imaging based on domain size and regularity. Overview images of the regions can be seen below in Figure 4.15 with the domain walls chosen for atomic resolution imaging noted and crystallographic direction marked. Important to note is that the first overview image does not capture all boundaries analysed.

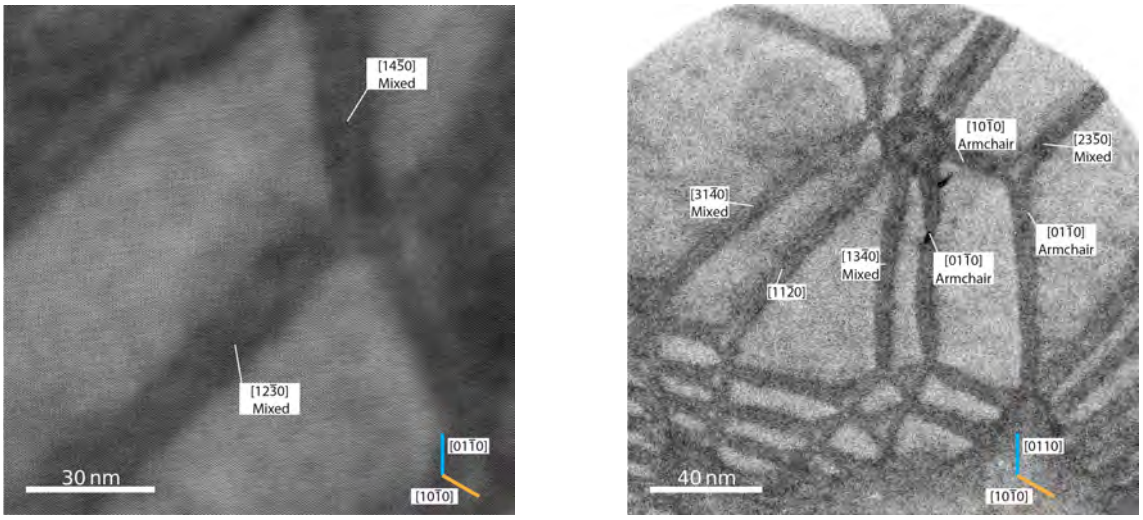

(a) Area 1 **(b)** Area 2

Figure 4.15: HAADF overview images over the areas imaged with HAADF. The approximate direction of the walls are marked with the walls image having its type marked under the direction. The unit cell vectors can be seen in blue and orange in the lower right corner.

During imaging, three types of domain walls were found, these can be seen in Figure 4.16.

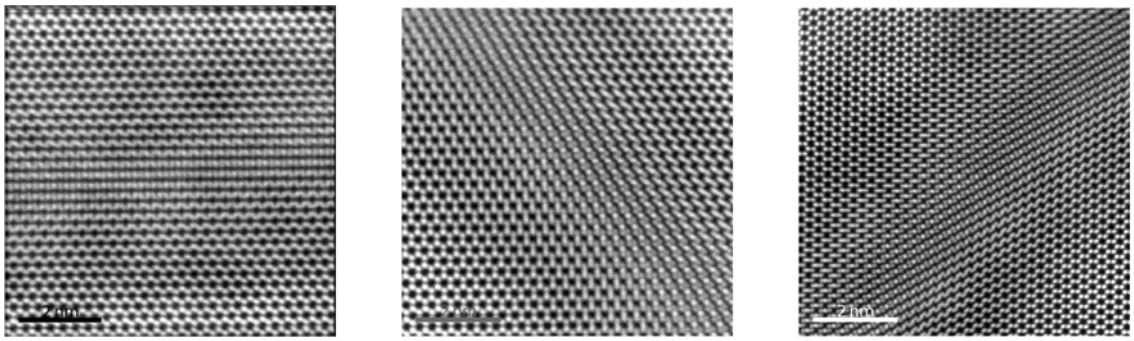

(a) Armchair **(b)** Ant **(c)** Mixed

Figure 4.16: a-c)HAADF images of the atomic structure in the domain walls. The atoms can be see as bright dots.

In the images, domains can be seen at either top and bottom or left and right corner with the barrier in the middle. Consistent for all domains was that the structure looked like normal 2H stacking. The domains having 2H stacking would be logical as this should be one of the lowest energy configuration available of this system and relax in to the 2H crystal structure. However, due to the slight twist between the bi-layers, there is a mismatch between domains were the atoms stack on top of each other. This would create domain walls which are visible in the images. The walls was usually of a similar thickness, counting the start of the barrier from the change in intensity, usually $9 - 7$ nm.

Images of the walls revealed that the type of barrier could be dependent on the crystallographic direction the barrier follows. When the barrier followed the $[10\bar{1}0]$, $[01\bar{1}0]$ and $[11\bar{2}0]$ directions, the barrier was of an armchair or ant type. The barrier was of a mixed type when following other directions. To understand what exactly is happening in the walls is hard to do by imaging alone. However, together with the knowledge that this system has two bi-layers, we can propose an hypothesis of what the movement of the layers could be.

Making the assumption that the bilayers remains largely intact and that the shift mainly comes in the form of translation between the bi-layers, a hypothesis of the bi-layers movements can be formed. In Figure 4.17, the suggested relative movement can be seen of the layers for the armchair type barrier. By tracing the splitting of the atoms from unit cell to unit cell, the relative movement can be traced.

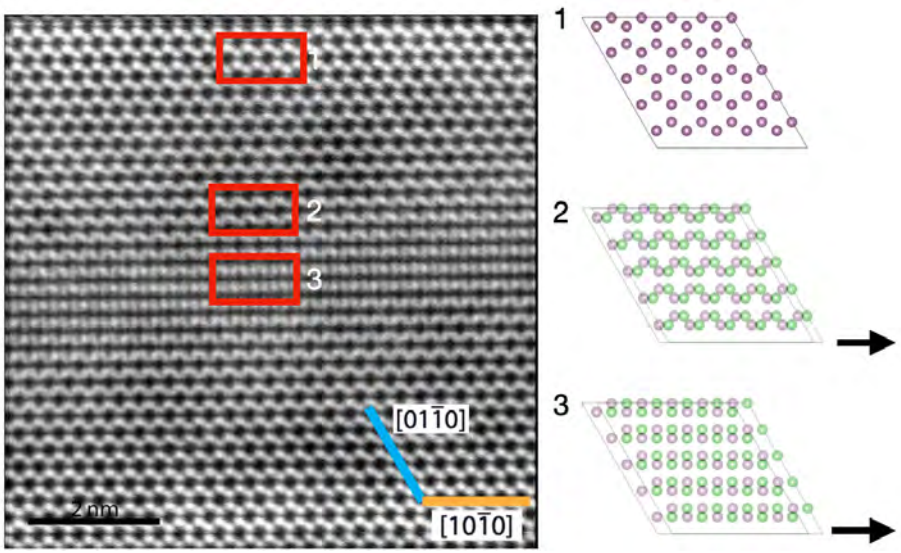

Figure 4.17: Image of the hypothesis of the movement of bilayers in the armchair type barrier. The right part shows bilayer movement in the corresponding number on the image. The individual bilayers have separate colours in the right.

Over the armchair barrier, the relative shift is in the same direction over the whole barrier and follows the $[10\bar{1}0]$, $[01\bar{1}0]$ or $[11\bar{2}0]$ direction. The movement of the relative shift does not always match the direction of the boundary and can be in other directions.

In Figure 4.18, the suggested relative movement can be seen of the layers of the ant type barrier can be seen.

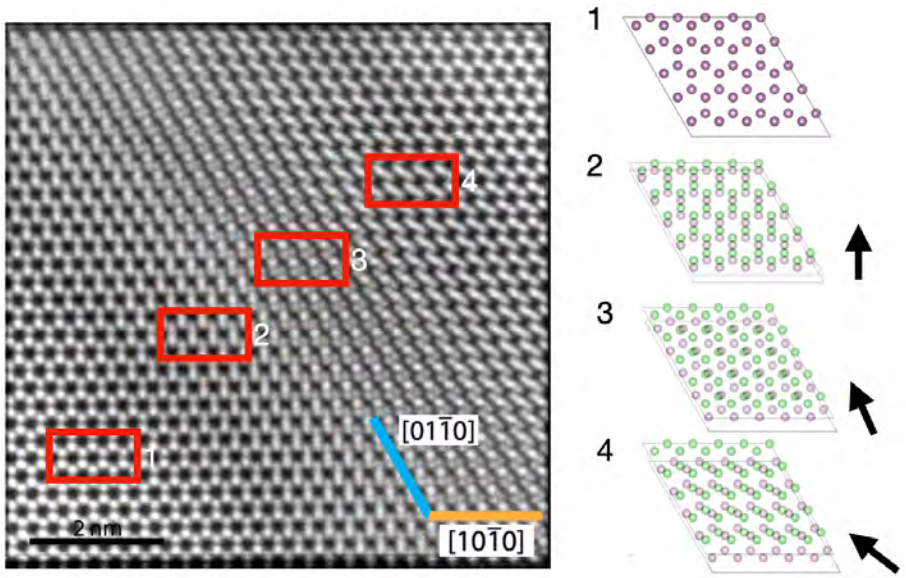

Figure 4.18: Image of the hypothesis of the movement of bilayers in the ant type barrier. The right part shows bilayer movement in the corresponding number on the image. The individual bilayers have separate colours in the right.

Over the ant type barrier, the relative shift changes direction over the barrier. For the case in the figure going from left to right, the proposed relative shift is first in the $[12\bar{3}0]$ and then gradually changes to shift in the $[\bar{1}2\bar{1}0]$ direction. This means that the shift would change by 60 degrees over the barrier.

In Figure 4.19, the suggested relative movement can be seen of the layers of the mixed type barrier can be seen.

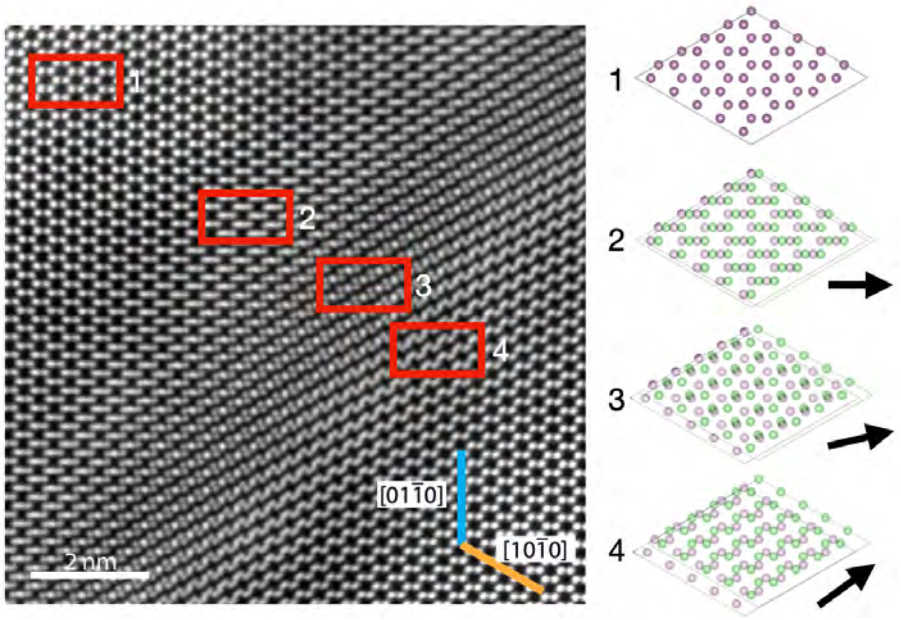

Figure 4.19: Image of the hypothesis of the movement of bilayers in the mixed type barrier. The right part shows bilayer movement in the corresponding number on the image. The individual bilayers have separate colours in the right.

Over the mixed type barrier, the relative shift changes direction over the barrier. For the case of the shift in the figure, the shift starts in the $[21\bar{3}0]$ direction and gradually changes to the $[11\bar{2}0]$ direction. This means that the shift would change by 30 degrees over the barrier.

The most common barrier was the armchair and mixed types, as only one barrier of the ant type was found out of the 13 imaged. This could be because the armchair and mixed types are more energetical favourable than the ant type, thus the structure always trying to minimize the energy of the system would prefer these. Another factor that could effect this would be the strain applied on the stack from bending from being suspended over a hole. This added strain could effect the sheer strain giving rise to the different types of walls.

Something that the atomic models in the Figure 4.17, 4.18 and 4.19 does not consider is the strain. It is hard to establish in these images as the exact positions of the atoms and thus the strain as well. But, non-precise calculations can be made as to roughly how big the strain could be. By taking the distance of the shift and dividing it by the width of the domain, we can gage the sheer strain. Making the assumption that the as the two bi-layers are free-standing, they would experience an equal sheer strain, the sheer strain can be estimated to be around 2.25% but could be higher locally.

Another assumption made that may not be true is that these structures are static. Looking at the individual images used for the final images shown earlier. Dynamic effects could be effecting the structures imaged. In Figure 4.20, the first and last

image taken during a sequence can be seen.

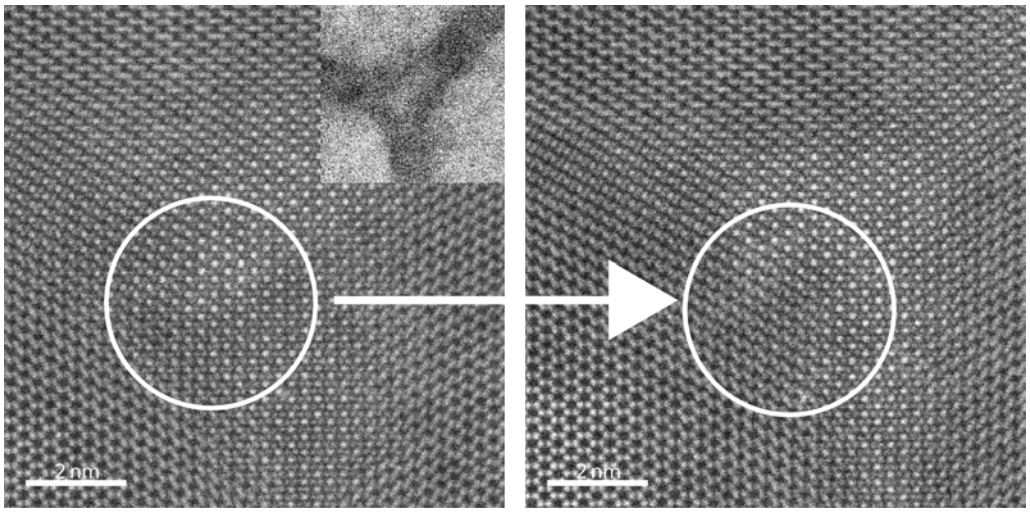

Figure 4.20: Image of intersection of three walls. The circles show an area with difference in atomic stacking between image one and two taken 80 seconds apart. The arrow shows highlights which image was taken first and last.

The images in the figure are taken 80 seconds apart. The middle part of the images highlight by white circles show that the structure is not the same in both images. The brightest atoms present in the left image is not present any more when the right image is taken. These dynamic effects could be from heating effects from the beam on the sample as heat would provide more energy to the system. This extra energy could create extra energy and start jumping between states that are local energy minimas. The bright atoms disappearing could also be knock-on damage and be vacancies created from the beam. In the future, it would be interesting to lower the dose and see if these dynamic effects is still present.

4.2.2.3 DFT calculations of Domain Walls of Twisted Bi-Bi Stacks

To investigate what walls would be more energetically favourable, DFT calculations were used. The results from the DFT calculations can be seen in Figure 4.21.

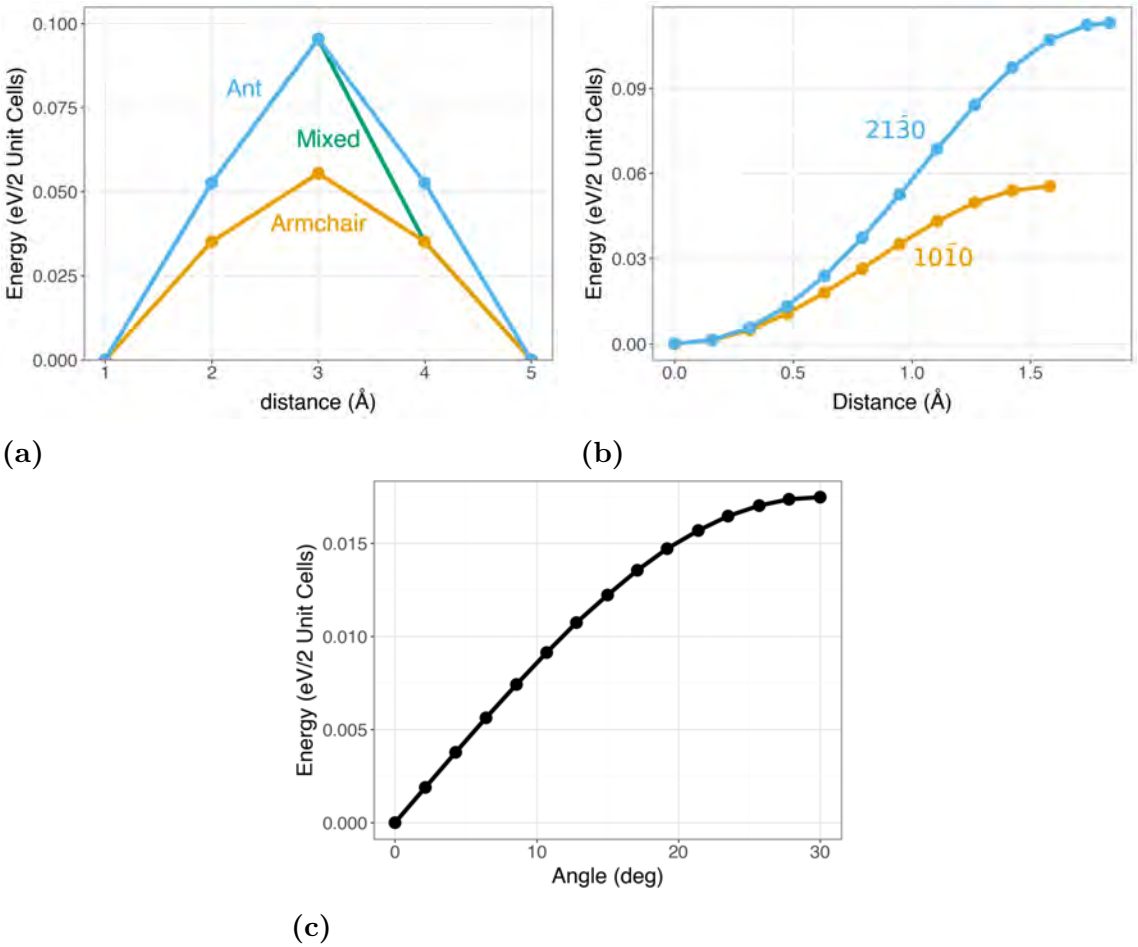

Figure 4.21: a) DFT calculation results for the barrier types found during HAADF imaging. The y-axis is energy per two unit cells and the x-axis is the step selected over the barrier. b) DFT calculation results from translation of the bilayers relative to each other in two directions. The y-axis is energy per two unit cells and the x-axis is in Ångstrom. c) DFT calculation results from translating 0.9 Å in different directions. The y-axis is energy per two unit cells and the x-axis is in degrees.

As these calculations uses heavy approximations, they should not be used as proof but as a possible estimation of the energy in the barrier. In Figure 4.21a, we can see a difference between the walls in the energy. The three points marked in the figure represent the energy of the system from the Figure 4.17, 4.18 and 4.19. We can see that the armchair barrier is energetical more favourable than the ant barrier and the mixed barrier. This could be the reason why few ant type walls was observed but further analysis would be needed to confirm this.

Figure 4.21b shows that the energy gain across the systems over the boundary is non-linier and that the armchair barrier type is again more energetical favourable than the ant barrier type. But the nonlinearity can also be a product from the way the calculation was made.

Figure 4.21c shows the energy gain across the systems when applying the shift

in different directions. Shift angles between 0° and 30° degrees with a translation of 0.95 Å was calculated. This calculation showed that the 0° translation, corresponding to the armchair barrier, was the most energetically favourable one.

These calculations can as mentioned serve as an estimation as what could be the energy distribution over the barrier. However, by isolating the parts of the system and assuming infinite repetition of each part, all longer range effects are missed. As each part are unit cells large and connected to each other, these effects are very important and would be needed to draw any conclusions. Simulations of the total system would be a probably be a good way to include the these effects.

4.2.3 Other Observations

In this part, observations not relating directly to the Moiré patterns constructed using bi-bi and mono-mono layers is discussed. Starting with the black and white contrast visible in many samples and can be seen in Figure 4.12a. Then, contamination likely between the layers is discussed and then potential Moiré patterns from hBN is shown.

4.2.3.1 TEM Directional Periodic Black and White Contrast

A feature present in nearly parallel stacked samples were black and white fuzzy stripes that was only visible in DF. The pattern changed direction depending on which diffraction spot was used for DF imaging. The patterns can be seen in Figure 4.22. Based on the appearance and behaviour depending on diffraction spot, the flakes could be corrugated. If they are corrugated, this could be explained by the relaxation of the atomic structures not being purely in-plane but also out-of-plane. This would result in corrugated structures. Some areas in mono-mono stacks showed reconstruction. These were always close to areas with thicker parts close to the area with domains present. This makes sense based on the hypothesis that the thicker flakes close by restricts the flakes reconstruction to be in-plane. It would also make these regions unstable and prone to damage, which could explain the reason that it was not possible to find them during HAADF imaging.

To strengthen this hypothesis, mono-mono stacks sandwiched between hBN was constructed, however all these samples were lost in the last cleaning step. Bi-bi stacks with 180° twist was also constructed to make the flakes more rigid and make the relaxation mostly in-plane. These samples showed some areas of possible reconstruction but the majority of the area was still dominated by the fuzzy stripes. Something that complicates this hypothesis is STEM images gathered from a corrugated area. The sample PL6, a mono-mono stack and PL2, a bi-bi stack, was first analysed in TEM DF mode and deemed to be corrugated and lacking domain structures. When later analysing the same sample in STEM at 30kV and 80kV, domain structures appear to be present in the same area. This could be as a result of the possible corrugation having a stronger diffraction contrast than the domains. Thus in DF TEM, the corrugation dominates the signal but in STEM, the corrugation is not as present and the domains become visible.

As no reference images similar to the dark and bright stripes could be found in literature, more measurements as 4D-STEM or Ptychography would be needed to establish what the cause of them are. Further measurements would also be interesting to check other samples deemed to be corrugated and lacking domains to see if there are domains present using STEM.

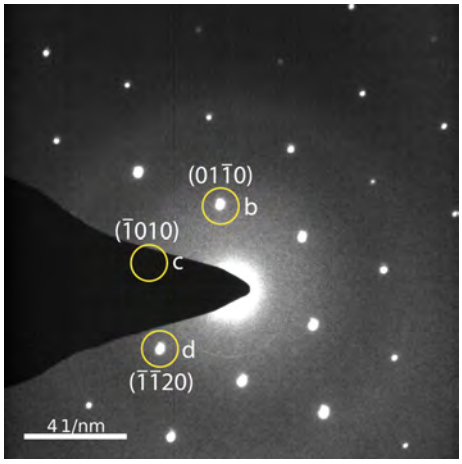

(a) Diffraction [0001]

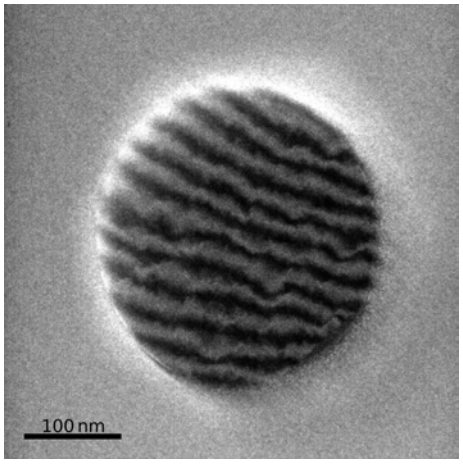

(b) DF (01$\bar{1}$0)

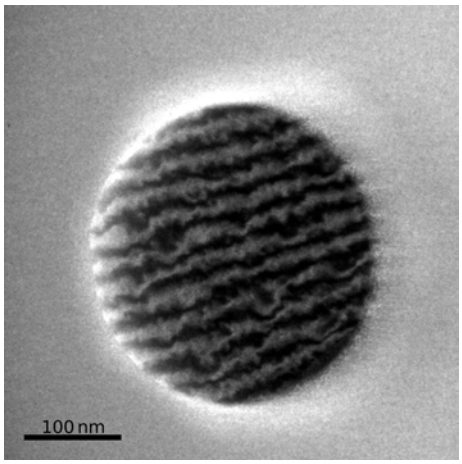

(c) DF ($\bar{1}$0$\bar{1}$0])

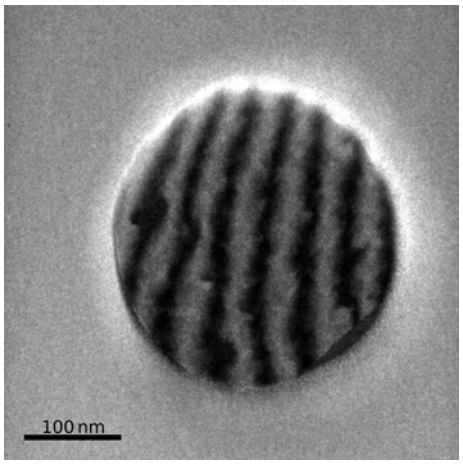

(d) DF ($\bar{1}\bar{1}$20)

Figure 4.22: a)SAED of PL10 where possible corrugations was observed shown in images b-d). b-d) DF TEM images captured from PL10 showing the possible corrugations direction depending on the DF spot chosen for imaging.

4.2.3.2 TEM Imaging of Contamination in Twisted Structures

Imaging of areas where the PC had made contact with the bottom flake can be seen on Figure 4.23.

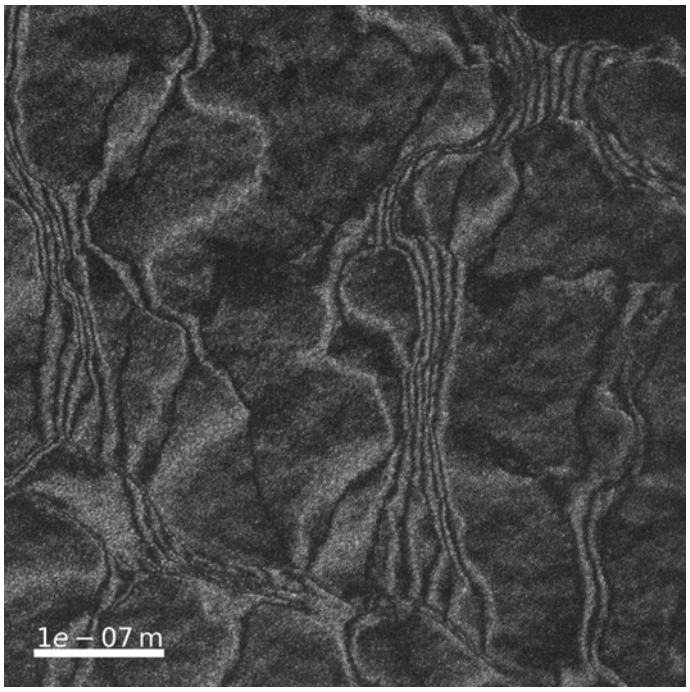

Figure 4.23: DF TEM image of PL7 were the PC made contact with the bottom. The stack is in 5 nm thick SiN window

In the figure, black and white lines without periodicity is precent. These features were observed to not change direction which suggests these are different from the earlier features proposed to be corrugation. As these images is taken from the an area on the stack where the PC made contact, this could be residue from the PC trapped between the two flakes. Contamination between the flakes would prevent them from making contact and creating Moiré structures. This would mean that preventing the PC extending too far over the bottom flake during pickup of the top flake is important from creating good stacked structures.

4.2.3.3 TEM Images of Moire Pattern in Folded hBN

While pickup of a hBN flake, parts of the flake stuck to the substrate longer than the majority and was buckled during pickup. During imaging of this part of the hBN flake showed periodic structures, some that looked like Moiré structures. DF TEM images of this is shown in Figure 4.24.

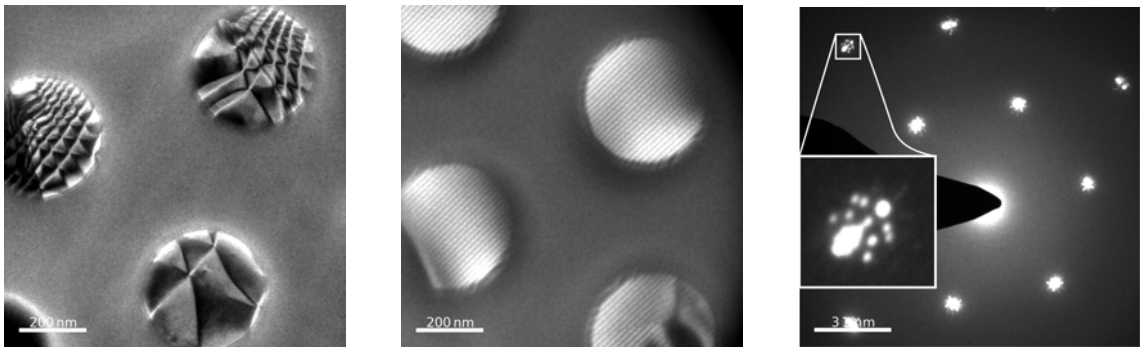

(a) DF Area 1 **(b)** DF Area 2 **(c)** Diffraction Area 2

Figure 4.24: a-b) DF TEM images of periodic patterns resembling Moiré structures. c) SAED from Area two in b).

In Area 1, there are dark and bright triangular domains present. These are similar looking to domains showed earlier in this report, but as the thickness and the twist angle is unknown, little can be said in this report about this structure. Based in optical contrast of the hBN flake, it can be estimated that it is nms thick but no greater accuracy without further analysis can be reached. The Area in Figure 4.24b shows smaller periodicity pattern with diffraction pattern also shown in Figure 4.24c. In the diffraction pattern, additional spots can be seen radiating out from one of the main spots in each pair of the diffraction pattern. This is especially clear in the main spot pair in the top left corner. This pattern is similar to what would be expected from double diffraction. But again, as little is known about the system it would be hard to draw any hard conclusions about this without further investigation.

4.3 Detection of out-of-plane polarisation from atomic stacking in MoS_2

Parallel stacked twisted structures can exhibit out-of-plane polarisation due to the stacking in the domains. In contrast, in anti-parallel stacked twisted structures, there is no out-of-plane polarisation. One method that can be used to investigate electric fields in materials is DPC. To detect possible out-of-plane polarisation in the two different kind of stacking, we studied cross-sectional structures of 2H and 3R-MoS_2 flakes, which show anti-parallel and parallel stacking of individual MoS_2 layers, respectively. The measurements were made to see if the polarisation present in bulk MoS_2-3R could be imaged.

The section begins with presenting DPC results, discussing the difficulty of diffraction contrast and motivating the use of tDPC which the results from is then presented.

4.3.1 DPC Measurement of 2H and 3R Stacking

The DPC images taken of the cross-sections prepared showed that strong diffraction contrast was present. In Figure 4.25, the x and y CoM shift have a lot of features. These are probably due to diffraction contrast coming from the beam being close to the zone axis of the MoS2. By tilting the sample around the x-axis in the figure, some of the diffraction contrast could be mitigated. This is most likely due to tilting away from the zone axis reduces the diffraction contrast and improves the DPC signal. However, even after tilting, there was a lot of diffraction contrast present. Due to this, it was decided to use tDPC to remove the remaining diffraction contrast.

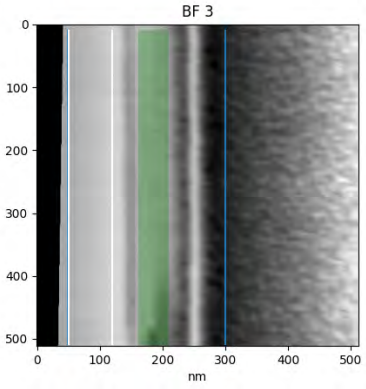

(a) BF image

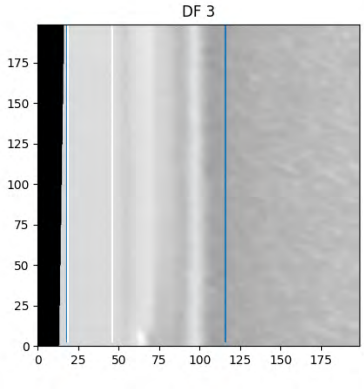

(b) DF image

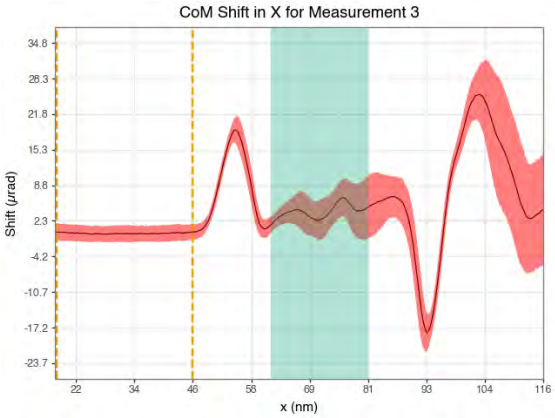

(c) CoM shift x-axis

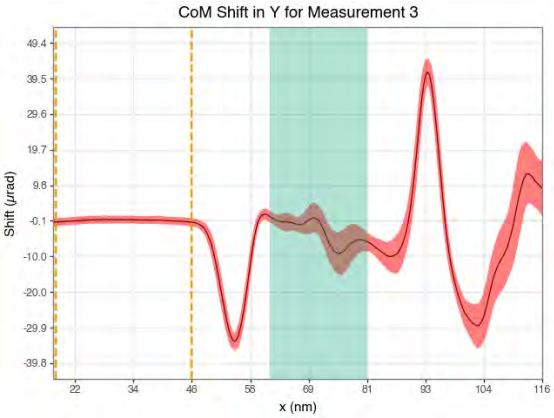

(d) CoM shift y-axis

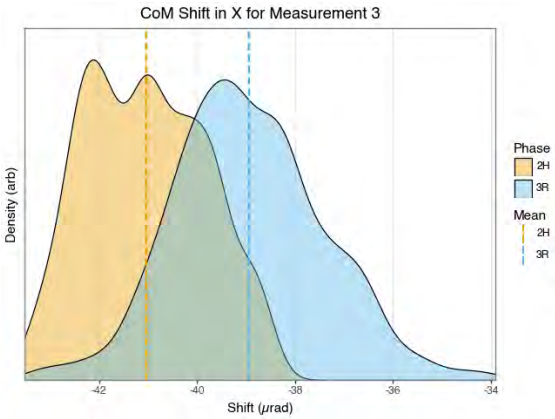

(e) CoM shift x-axis in 3R

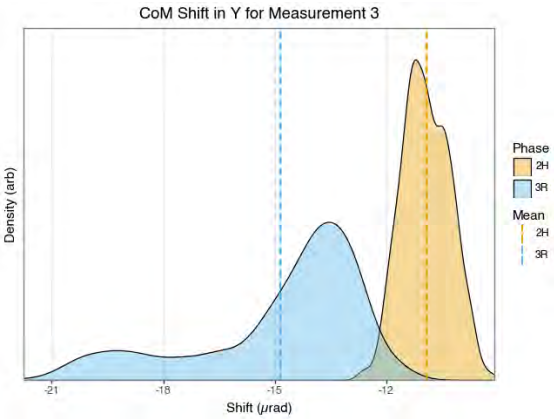

(f) CoM shift y-axis in 3R

Figure 4.25: a) BF image of sample with blue lines showing where the line data was gathered from, the white lines showing the 2H part and the green shaded area showing the 3R part. b) DF image of sample with blue lines showing where the line data was gathered from and the white lines showing the 2H part. c-d) Line graph showing the CoM shift in x- and y-axis with the red shading showing the standard deviation, the orange lines showing the 2H part and the shaded green area showing the 3R part. e-f) Density plots of the CoM shift in the 2H and 3R parts of the image with the mean represented as a dashed line.

4.3.2 tDPC Measurement of 2H and 3R Stacking

To remove the diffraction contrast, tDPC was used. In Figure 4.26, one of the processed tDPC images can be seen. The diffraction contrast is not as prevalent as in the first image but some contrast can still be seen in the middle of two MoS_2 regions. Taking the mean CoM shift of the 3R-MoS_2 region and comparing it to the 2H-MoS_2 region, it is hard to see a clear pattern. The data of the mean shift of the CoM for all tDPC measurements can be seen in Figure 4.27. The shift from all measurements are very small compared to previous measurements and with the possibility of residual diffraction contrast still effecting the imaging, caution should be taken when interpreting the results. Between the first and second measurement of the 2H3R_3, the signal changed and the out of plane shift was stronger after thinning. The sign of the signal also changed from negative to positive with the out-of-plane shift displaying the largest difference. What this could be due to is hard to tell and would require further investigation. Because the 3R-MoS_2 flake was very thin in 2H3R_3, the usable area where the interface did not effect the signal was much smaller and could have effects on the measurements due to the probe size being large compared to the thickness.

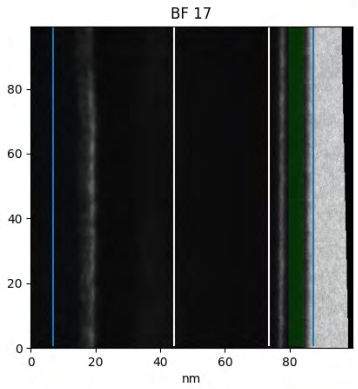

(a) BF image

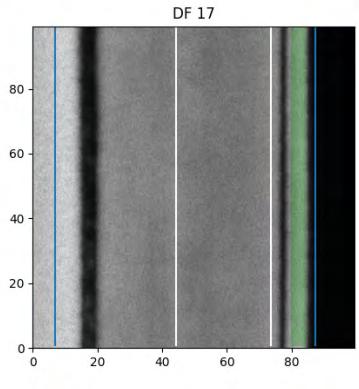

(b) DF image

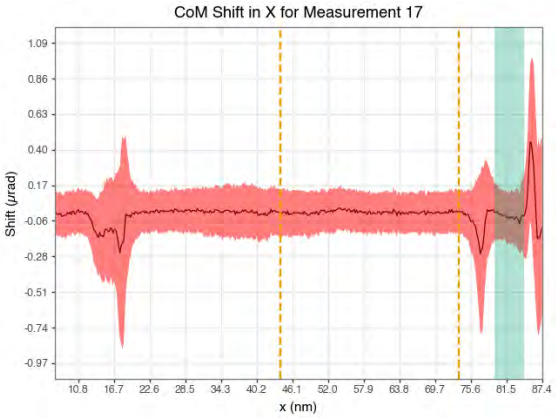

(c) CoM shift x-axis

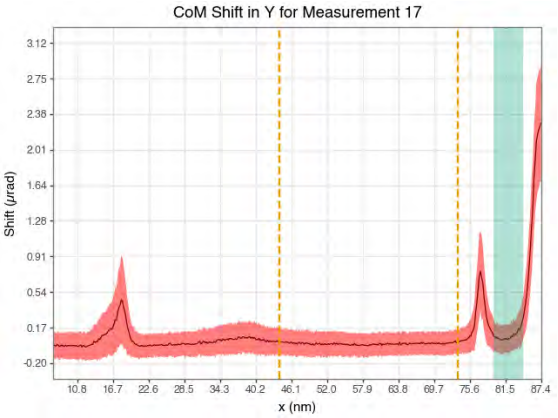

(d) CoM shift y-axis

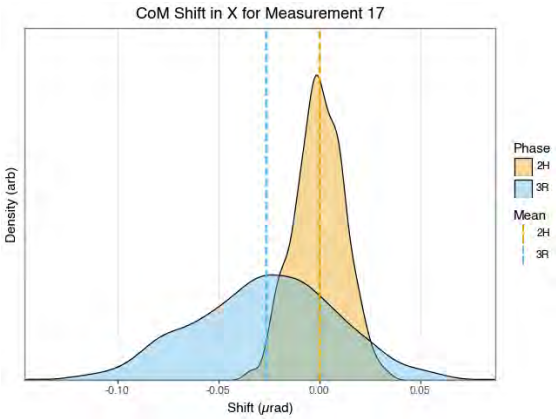

(e) CoM shift x-axis in 3R

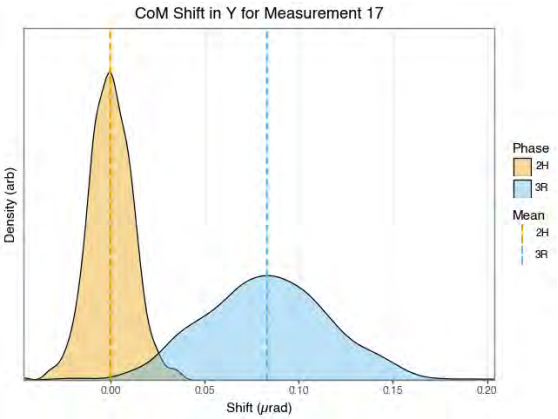

(f) CoM shift y-axis in 3R

Figure 4.26: a) BF image of sample with blue lines showing where the line data was gathered from, the white lines showing the 2H part and the green shaded area showing the 3R part. b) DF image of sample with blue lines showing where the line data was gathered from, the white lines showing the 2H part and the green shaded area showing the 3R part. c-d) Line graph showing the CoM shift in x- and y-axis with the red shading showing the standard deviation, the orange lines showing the 2H part and the shaded green area showing the 3R part. e-f) Density plots of the CoM shift in the 2H and 3R parts of the image with the mean represented as a dashed line.

The CoM shift observed in MoS_2-3R using tDPC is summarised in Figure 4.27.

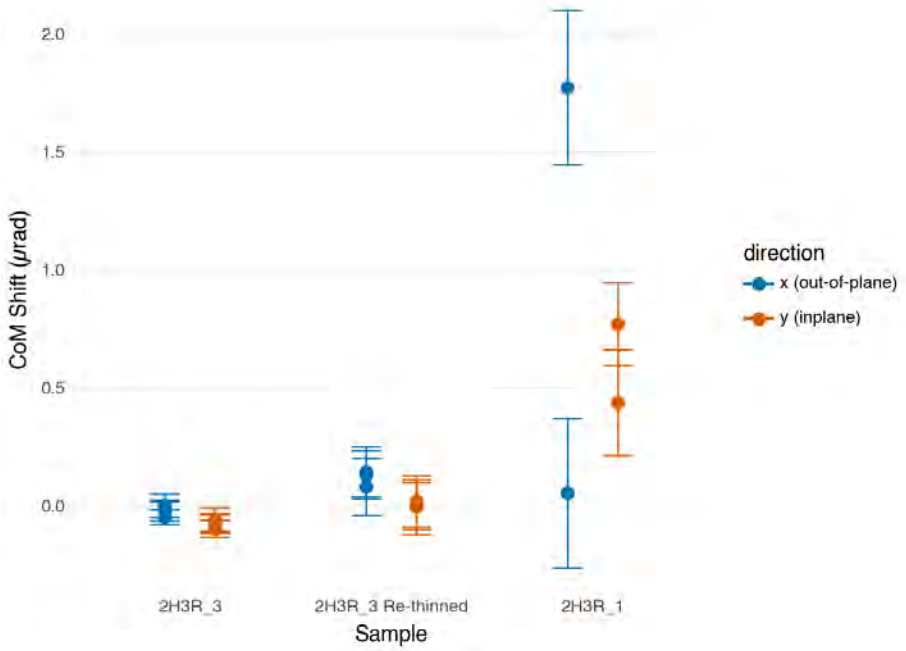

Figure 4.27: The figure shows the CoM shift in 3R from all tDPC measurements. The error bar shows the standard deviation of the data.

The combined results are hard to interoperate and no clear trends can be seen. It is suspected that even when using tDPC, the polarisation is not strong enough to be detected due to the still present diffraction contrast. Simulations of the diffraction contrast from the MoS_2 would be needed to say of the polarisation was captured in these measurements.

5

Conclusion

In this thesis, an experimental setup, a protocol for fabricating twisted TMD Moiré structures has been successfully developed, improved and used. For the exfoliation of atomically thin flakes, temperature and exfoliation technique were found to be important parameters to control. For the stacking process, flake size, temperature of the vacuum chuck, quality of PC film, angle of the glass slide relative to the substrate, wavefront control and which side of the flakes to approach was found to be important parameters for successful stacking. A fast and reliably thickness determination of atomically thin flakes was also developed for faster and more efficient twisted TMD Moiré structures production. Raman cutting was also found to be a good method to shape flakes with minimal damage to the main structure.

Characterisation of the produced twisted TMD Moiré structures produced STEM images and TEM BF, DF and SAED patterns of parallel stacked and anti-parallel stacked structures. The characterisation of the parallel stacked twisted TMD Moiré structures structures showed that domain structures had successfully formed on the samples produced. These were used to characterise the shape and behaviour of the domains and domain walls with SAED spot splitting possibly stemming from a $14.8 \pm 1.5 \, \frac{\mathrm{V}}{\mathrm{nm}}$ electric polarisation present in the domain walls. The characterisation of the anti-parallel stacked twisted TMD Moiré structures structures showed that domain structures had successfully formed on the samples produced. STEM images showed that 0.4 μm large areas of bubble free Moiré structures were made. The images showed a variation in the domain size that could be from the bending of the flakes. Atomic resolution imaging of the domain walls showed the atomic structure of the transition from one domain to another. A hypothesis was presented for the shift of the individual bilayers and was investigated using DFT calculations. The DFT calculations showed that some of the structures seen were not energetically favourable and could stem from global effects not accounted for in the DFT calculations. Other observations was also imaged. Dark and bright lines were observed in all samples in DF TEM. These could be bending contrast from corrugation in the structures. Moiré patterns were also observed in hBN when covering the twisted TMD Moiré structures with hBN.

DPC and tDPC was used to measure the out-of-plane polarisation of bulk MoS_2-3R. The results from the DPC and tDPC showed no conclusive polarisation, probably due to strong diffraction contrast. Due to this, it is hard to say if it is possible or not to measure the polarisation of twisted TMD Moiré structures.

With the above findings, this thesis has contributed to the research of 2D materials and made new useful observations on twisted TMD Moiré structures.

Bibliography

[1] S. Du, J. Liu, and S. Zheng, "Emerging Optoelectronic Applications of Sliding Ferroelectricity," *Advanced Materials Technologies*, vol. 10, no. 12, Jun. 2025, ISSN: 2365-709X. DOI: 10.1002/admt.202402121.

[2] S. Haastrup et al., "The Computational 2D Materials Database: high-throughput modeling and discovery of atomically thin crystals," *2D Materials*, vol. 5, no. 4, p. 042 002, Sep. 2018, ISSN: 2053-1583. DOI: 10.1088/2053-1583/aacfc1.

[3] B. Schönfeld, J. J. Huang, and S. C. Moss, "Anisotropic mean-square displacements (MSD) in single-crystals of 2 H - and 3 R - MoS ₂," *Acta Crystallographica Section B Structural Science*, vol. 39, no. 4, pp. 404–407, Aug. 1983, ISSN: 0108-7681. DOI: 10.1107/S0108768183002645.

[4] W. Zhao et al., "Metastable MoS ₂ : Crystal Structure, Electronic Band Structure, Synthetic Approach and Intriguing Physical Properties," *Chemistry – A European Journal*, vol. 24, no. 60, pp. 15 942–15 954, Oct. 2018, ISSN: 0947-6539. DOI: 10.1002/chem.201801018.

[5] A. Weston et al., "Atomic reconstruction in twisted bilayers of transition metal dichalcogenides," *Nature Nanotechnology*, vol. 15, no. 7, pp. 592–597, Jul. 2020, ISSN: 1748-3387. DOI: 10.1038/s41565-020-0682-9.

[6] S. J. Shah et al., "Progress and prospects of Moiré superlattices in twisted TMD heterostructures," *Nano Research*, vol. 17, no. 11, pp. 10 134–10 161, Nov. 2024, ISSN: 1998-0124. DOI: 10.1007/s12274-024-6936-3.

[7] S. H. Sung et al., "Torsional periodic lattice distortions and diffraction of twisted 2D materials," *Nature Communications*, vol. 13, no. 1, p. 7826, Dec. 2022, ISSN: 2041-1723. DOI: 10.1038/s41467-022-35477-x.

[8] H. Yoo et al., "Atomic and electronic reconstruction at the van der Waals interface in twisted bilayer graphene," *Nature Materials*, vol. 18, no. 5, pp. 448–453, May 2019, ISSN: 1476-1122. DOI: 10.1038/s41563-019-0346-z.

[9] J. I. Goldstein, D. E. Newbury, J. R. Michael, N. W. Ritchie, J. H. J. Scott, and D. C. Joy, *Scanning Electron Microscopy and X-Ray Microanalysis*. New York, NY: Springer New York, 2018, ISBN: 978-1-4939-6674-5. DOI: 10.1007/978-1-4939-6676-9.

[10] D. B. Williams and C. B. Carter, *Transmission Electron Microscopy*. Boston, MA: Springer US, 1996, ISBN: 978-0-306-45324-3. DOI: 10.1007/978-1-4757-2519-3.

[11] M. Zhang, R. Wei, J. Zeng, and Y.-H. Lin, "Probing atomic-scale structure of dielectric ceramics with scanning transmission electron microscopy," *Journal*

of Advanced Dielectrics, vol. 14, no. 03, Jun. 2024, ISSN: 2010-135X. DOI: 10.1142/S2010135X23430014.

[12] S. Toyama et al., "Real-space observation of a two-dimensional electron gas at semiconductor heterointerfaces," *Nature Nanotechnology*, vol. 18, no. 5, pp. 521–528, May 2023, ISSN: 1748-3387. DOI: 10.1038/s41565-023-01349-8.

[13] L. A. Giannuzzi and F. A. Stevie, Eds., *Introduction to Focused Ion Beams*. Boston, MA: Springer US, 2005, ISBN: 978-0-387-23116-7. DOI: 10.1007/b101190.

[14] H. Sun, O. Sahin, A. Javey, J. W. Ager, and D. C. Chrzan, "Theory of mechanical exfoliation of van der Waals bonded layered materials," *Physical Review Materials*, vol. 8, no. 6, p. 064 003, Jun. 2024, ISSN: 2475-9953. DOI: 10.1103/PhysRevMaterials.8.064003.

[15] F. Sigger et al., "Spectroscopic imaging ellipsometry of two-dimensional TMDC heterostructures," Jul. 2022.

[16] G. M. McClelland, R. Erlandsson, and S. Chiang, "Atomic Force Microscopy: General Principles and a New Implementation," in *Review of Progress in Quantitative Nondestructive Evaluation*, Boston, MA: Springer US, 1987, pp. 1307–1314. DOI: 10.1007/978-1-4613-1893-4{_}148.

[17] J. Palisaitis, C.-L. Hsiao, M. Junaid, J. Birch, L. Hultman, and P. O. Å. Persson, "Effect of strain on low-loss electron energy loss spectra of group-III nitrides," *Physical Review B*, vol. 84, no. 24, p. 245 301, Dec. 2011, ISSN: 1098-0121. DOI: 10.1103/PhysRevB.84.245301.

[18] J. Díez-Mérida et al., "High-yield fabrication of bubble-free magic-angle twisted bilayer graphene devices with high twist-angle homogeneity," *Newton*, vol. 1, no. 1, p. 100 007, Mar. 2025, ISSN: 29506360. DOI: 10.1016/j.newton.2024.100007.

[19] B. Chakraborty, H. S. S. R. Matte, A. K. Sood, and C. N. R. Rao, "Layer-dependent resonant Raman scattering of a few layer MoS ₂," *Journal of Raman Spectroscopy*, vol. 44, no. 1, pp. 92–96, Jan. 2013, ISSN: 0377-0486. DOI: 10.1002/jrs.4147.

[20] H. Li et al., "Rapid and Reliable Thickness Identification of Two-Dimensional Nanosheets Using Optical Microscopy," *ACS Nano*, vol. 7, no. 11, pp. 10 344–10 353, Nov. 2013, ISSN: 1936-0851. DOI: 10.1021/nn4047474.

[21] K. Ko et al., "Operando electron microscopy investigation of polar domain dynamics in twisted van der Waals homobilayers," *Nature Materials*, vol. 22, no. 8, pp. 992–998, Aug. 2023, ISSN: 1476-1122. DOI: 10.1038/s41563-023-01595-0.

[22] Y. Wang et al., "Ultrafast dynamics of ferroelectric polarization of NbOI2 captured with femtosecond electron diffraction," *Nature Communications*, vol. 16, no. 1, p. 8132, Aug. 2025, ISSN: 2041-1723. DOI: 10.1038/s41467-025-63533-9.

[23] N. Tilak, G. Li, T. Taniguchi, K. Watanabe, and E. Y. Andrei, "Moiré Potential, Lattice Relaxation, and Layer Polarization in Marginally Twisted MoS ₂ Bilayers," *Nano Letters*, vol. 23, no. 1, pp. 73–81, Jan. 2023, ISSN: 1530-6984. DOI: 10.1021/acs.nanolett.2c03676.

A

Calculations

A.1 Calculation of In-plane Electrical Polarisation from the Deflection of the Electron Beam

The electric field strength was calculated by using the equation used in previous work[22]

$$E = \frac{\gamma p^2}{em^* t} \tag{A.1}$$

where E is the electric field, γ is the deflection angle of the beam, p is the momentum of the electrons, m^* is the relative mass of the electrons and t is the sample thickness. γ was calculated by comparing the distance of the splitting from the polarisation with the distance from the BF spot to the $(10\bar{1}0)$ spot. γ was measured to be from 0.136 to 0.11 mrad.

B

Optical Image Contrast Measurement

The second Chip image contrast measurement can be seen in Figure B.1.

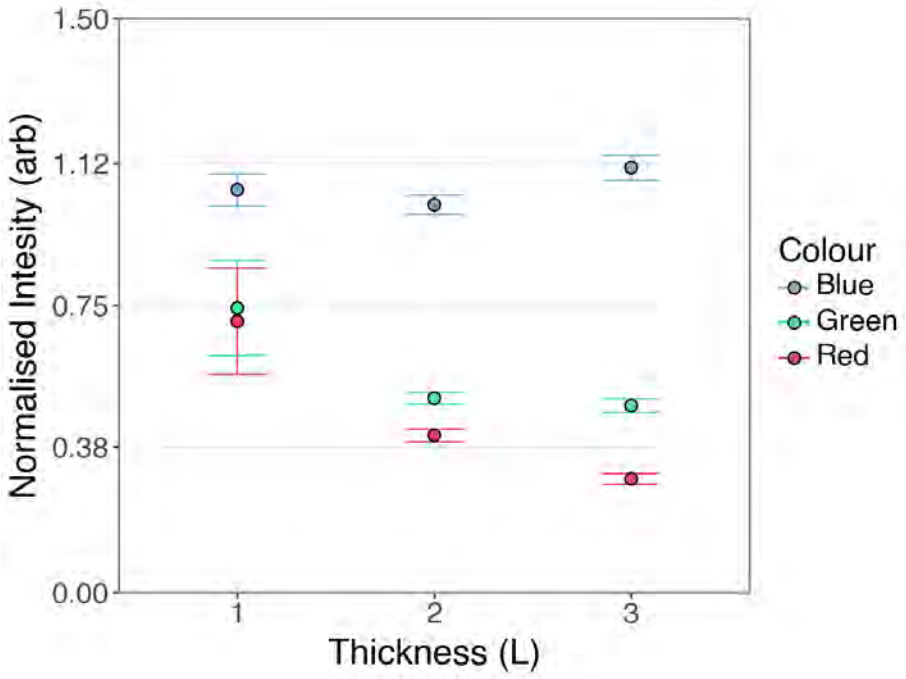

Figure B.1: Optical image contrast shown with each colour being plotted as the relative intensity of the substrate.

The intensity is higher than the measurement for the first chip. This could be due to some setting being different as follow up measurements show the same intensity as the measurements for the first chip. This is most likely due to the exposure time being different.

C

tDPC

The tDPC data presented in this part has the following structure: a) BF image of sample with blue lines showing where the line data was gathered from, the white lines showing the 2H part and the green shaded area showing the 3R part. b) DF image of sample with blue lines showing where the line data was gathered from, the white lines showing the 2H part and the green shaded area showing the 3R part. c-d) Line graph showing the CoM shift in x- and y-axis with the red shading showing the standard deviation, the orange lines showing the 2H part and the shaded green area showing the 3R part. e-f) Density plots of the CoM shift in the 2H and 3R parts of the image with the mean represented as a dashed line.

C.1 Sample 2H3R_1

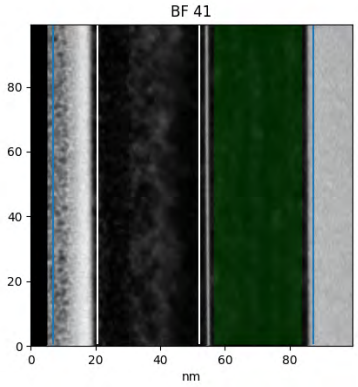

(a) BF image

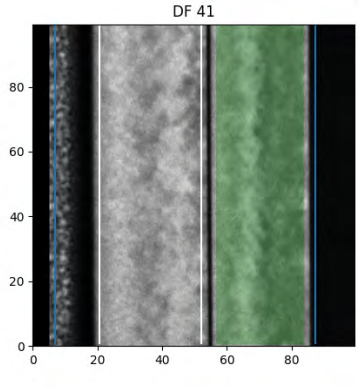

(b) DF image

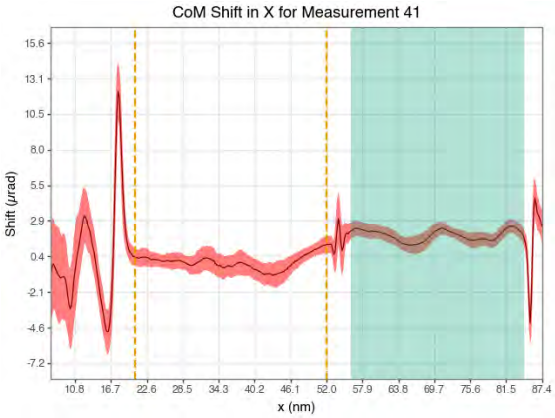

(c) CoM shift x-axis

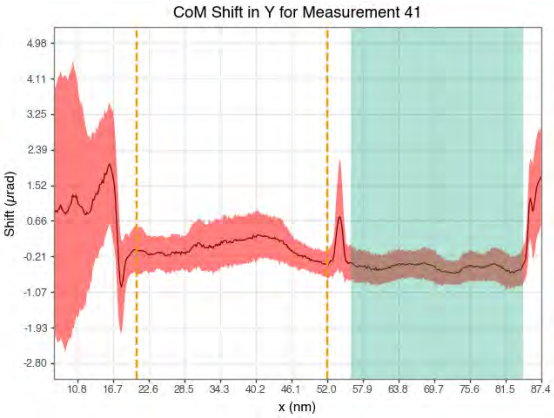

(d) CoM shift y-axis

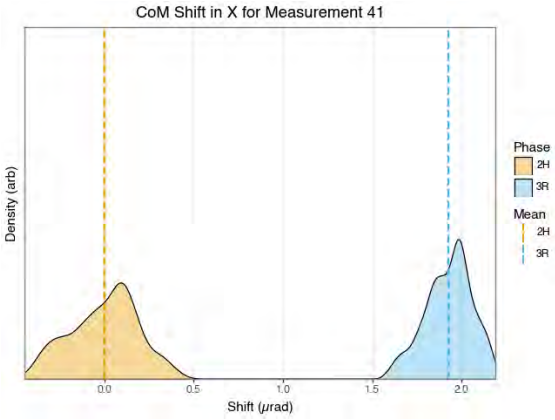

(e) CoM shift x-axis in 3R

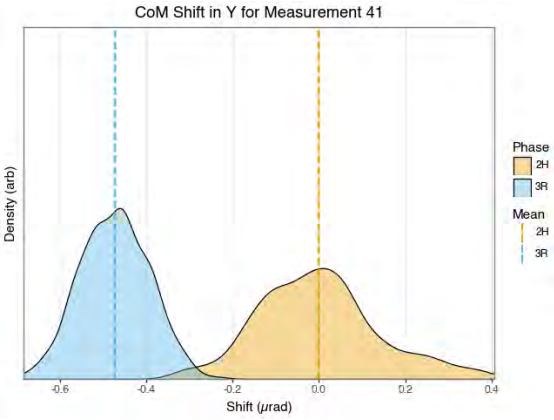

(f) CoM shift y-axis in 3R

Figure C.1: Scanned image 41.

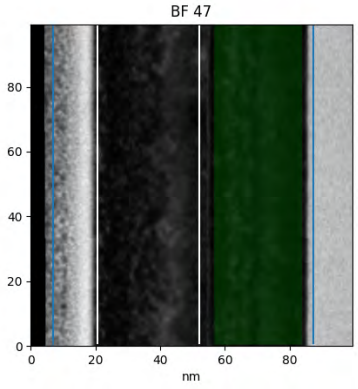

(a) BF image

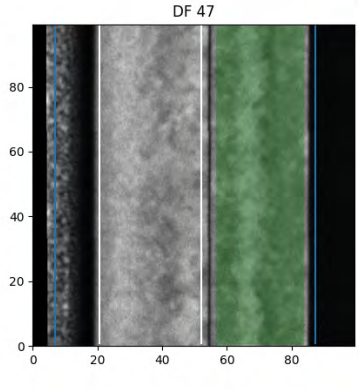

(b) DF image

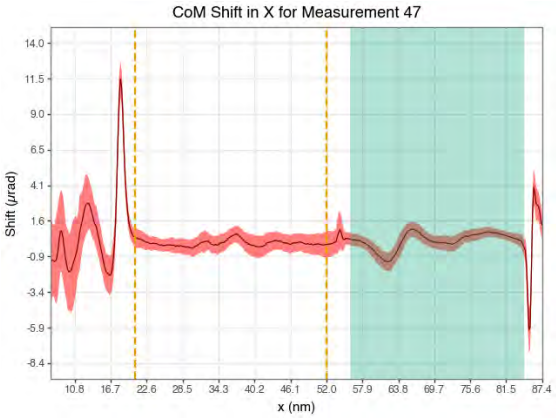

(c) CoM shift x-axis

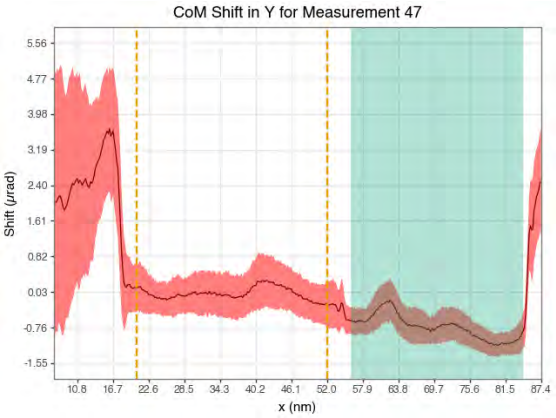

(d) CoM shift y-axis

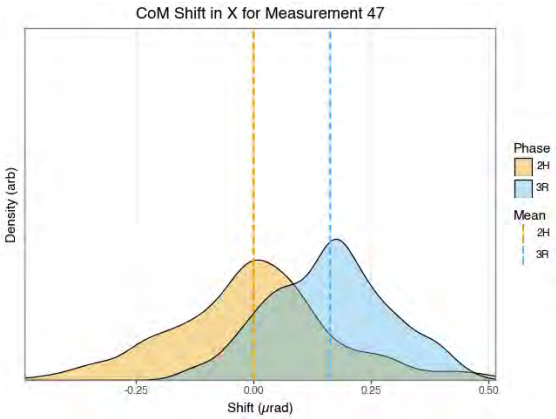

(e) CoM shift x-axis in 3R

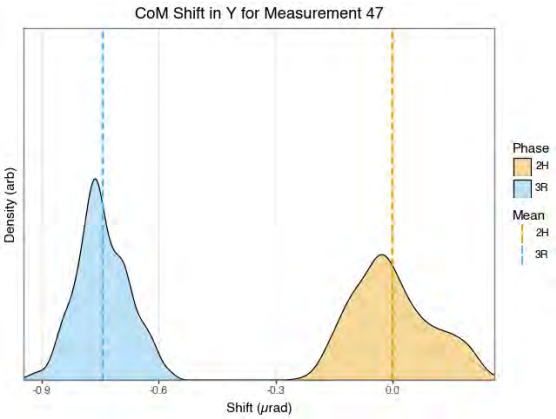

(f) CoM shift y-axis in 3R

Figure C.2: Scanned image 47.

C.2 Sample 2H3R_3

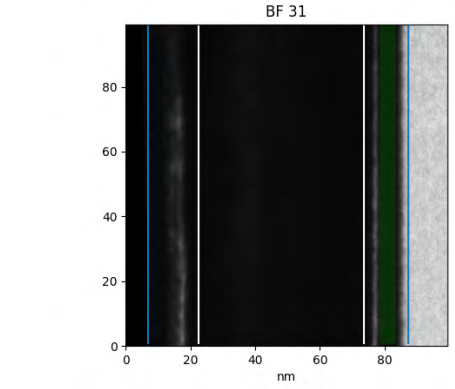

(a) BF image

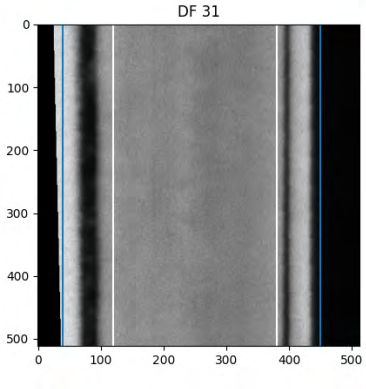

(b) DF image

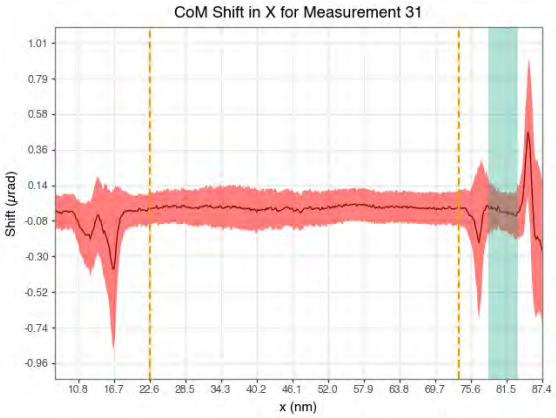

(c) CoM shift x-axis

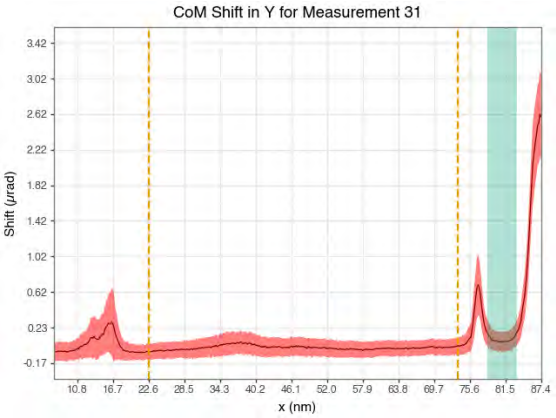

(d) CoM shift y-axis

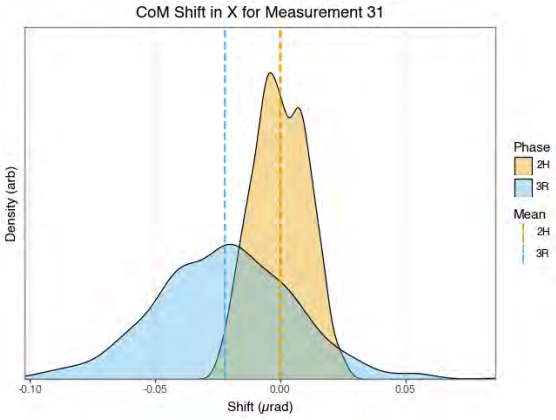

(e) CoM shift x-axis in 3R

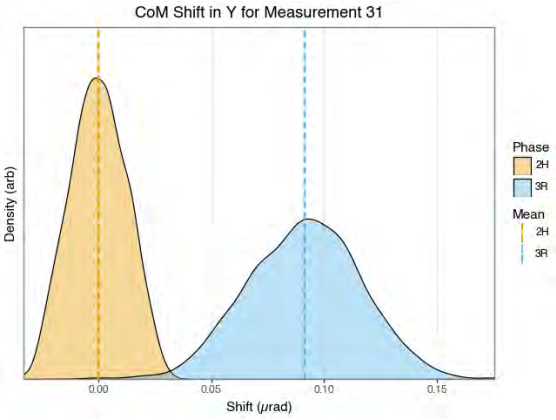

(f) CoM shift y-axis in 3R

Figure C.3: Scanned image 31.

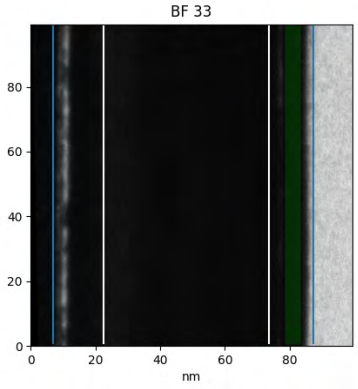

(a) BF image

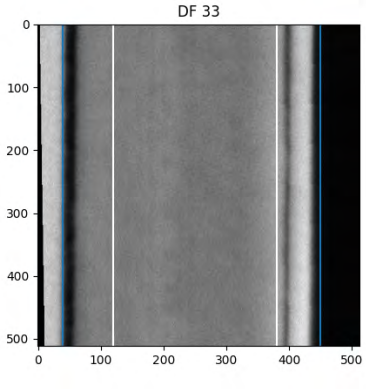

(b) DF image

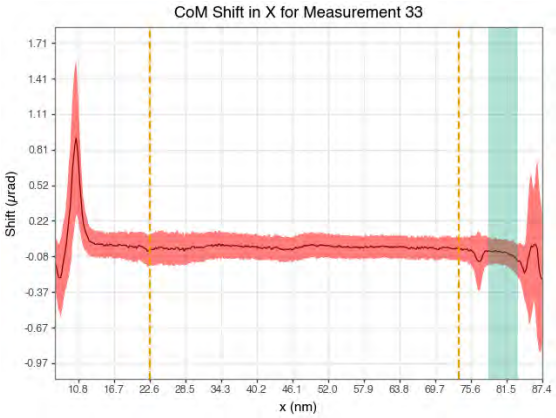

(c) CoM shift x-axis

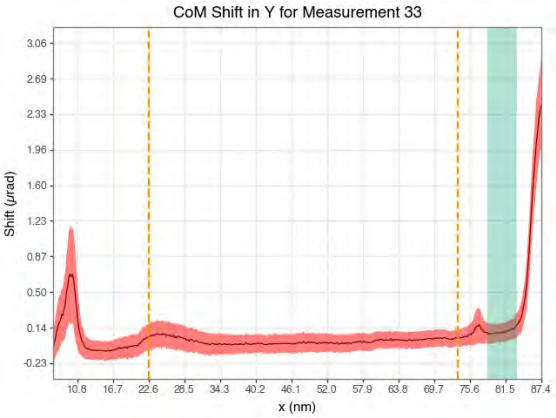

(d) CoM shift y-axis

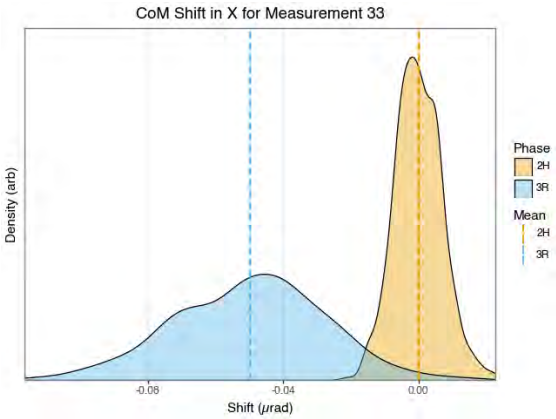

(e) CoM shift x-axis in 3R

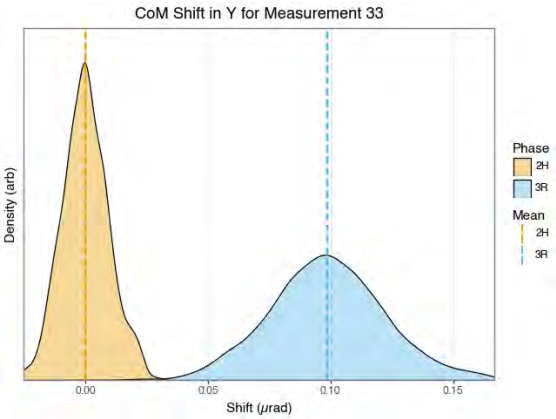

(f) CoM shift y-axis in 3R

Figure C.4: Scanned image 33.

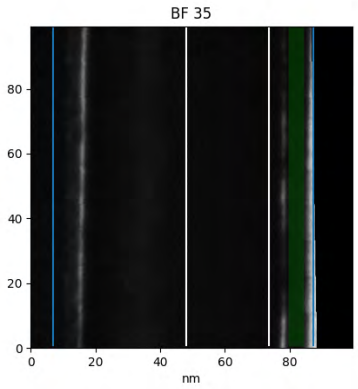

(a) BF image

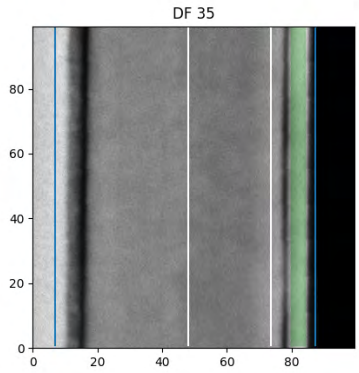

(b) DF image

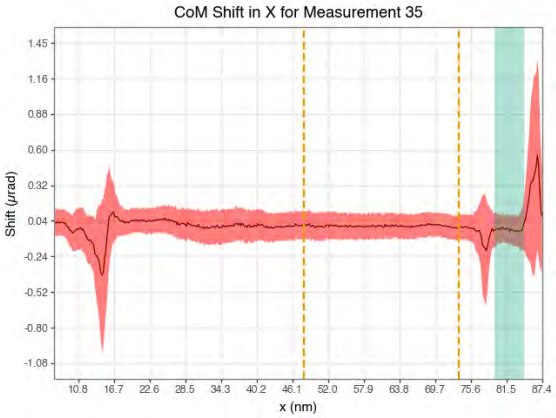

(c) CoM shift x-axis

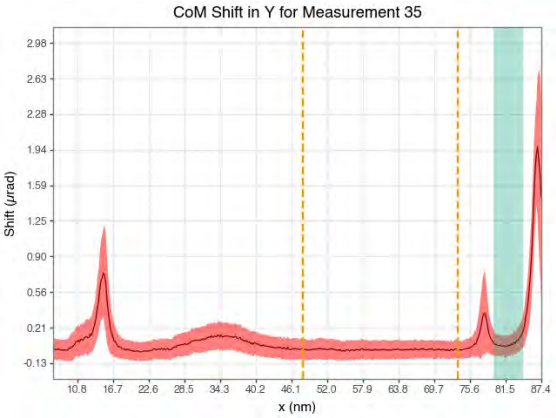

(d) CoM shift y-axis

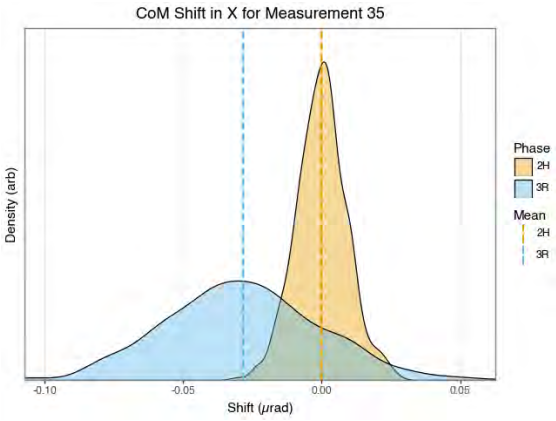

(e) CoM shift x-axis in 3R

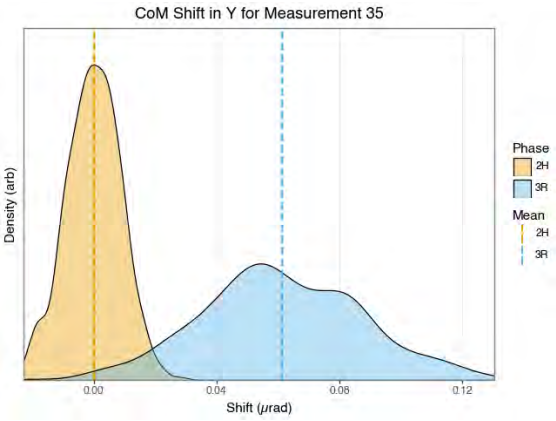

(f) CoM shift y-axis in 3R

Figure C.5: Scanned image 35.

C.3 Sample 2H3R_3 re-thinned

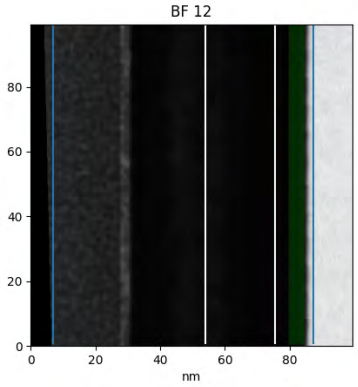

(a) BF image

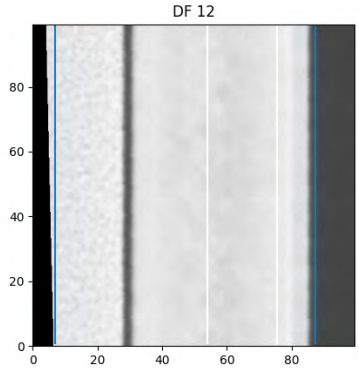

(b) DF image

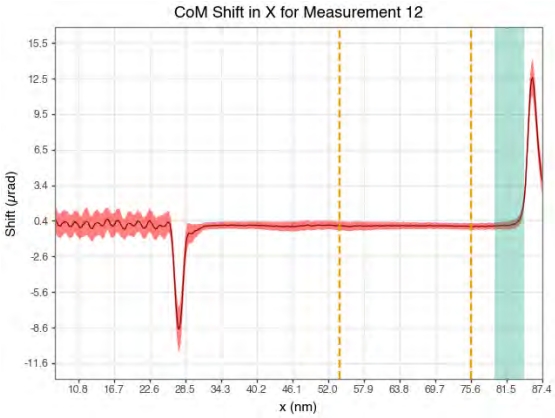

(c) CoM shift x-axis

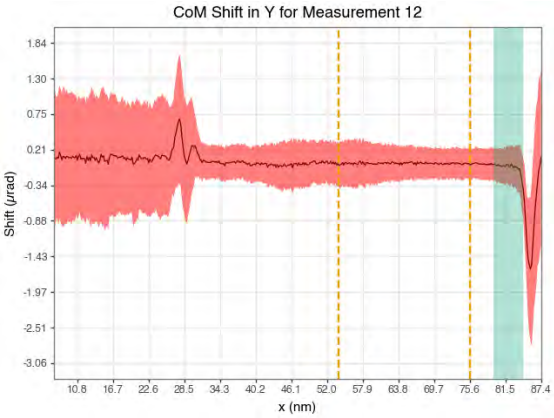

(d) CoM shift y-axis

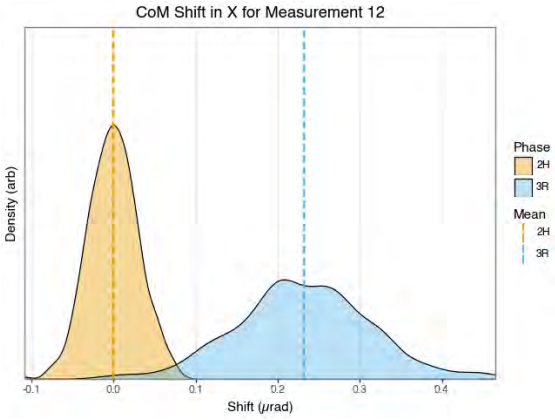

(e) CoM shift x-axis in 3R

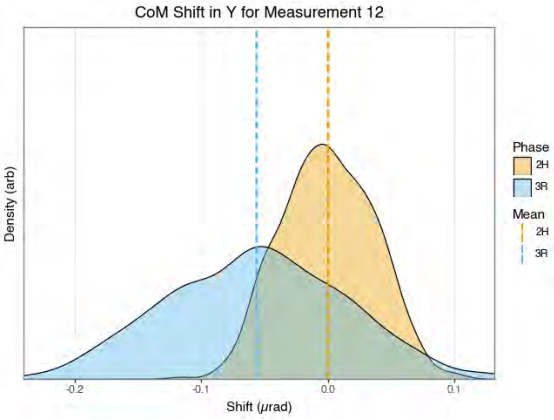

(f) CoM shift y-axis in 3R

Figure C.6: Scanned image 12.

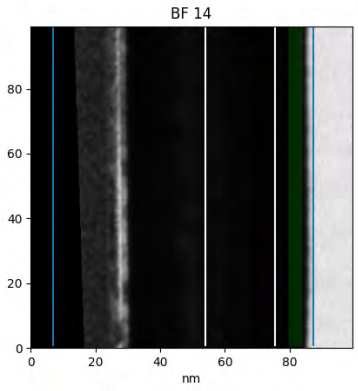

(a) BF image

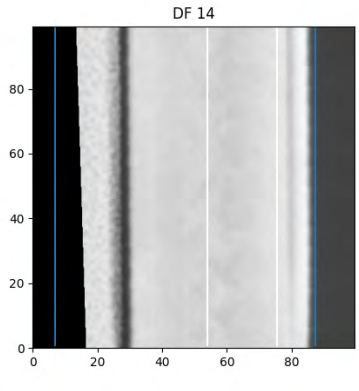

(b) DF image

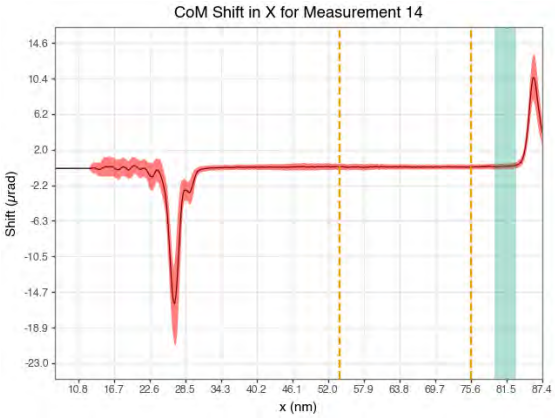

(c) CoM shift x-axis

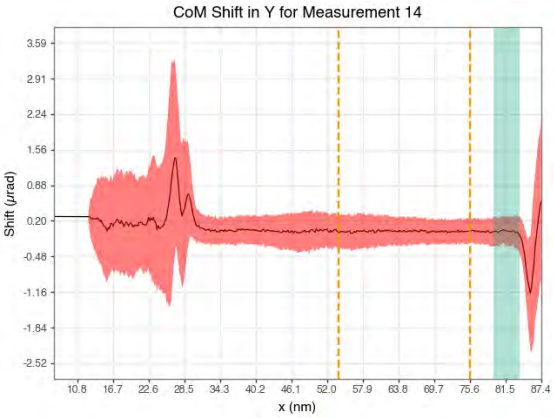

(d) CoM shift y-axis

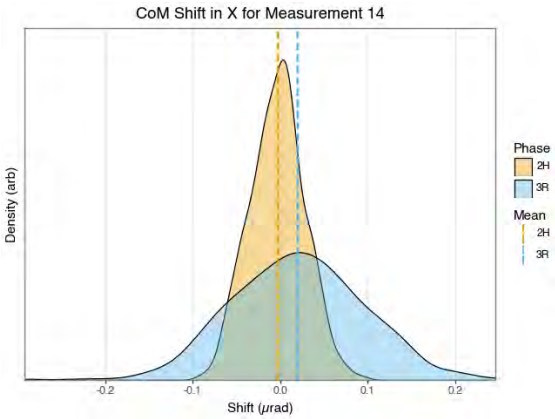

(e) CoM shift x-axis in 3R

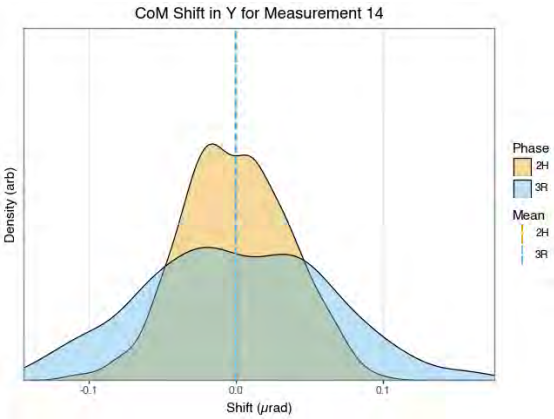

(f) CoM shift y-axis in 3R

Figure C.7: Scanned image 14.

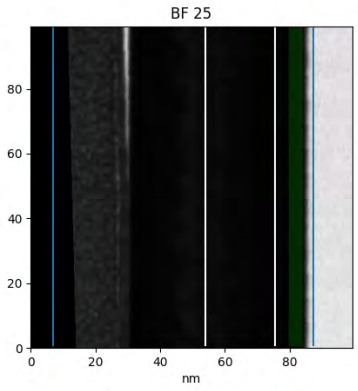

(a) BF image

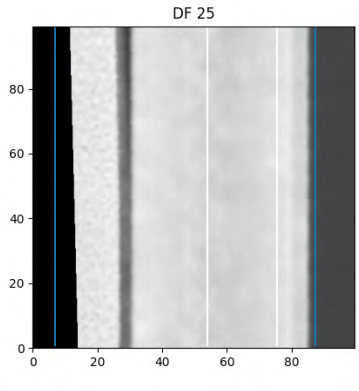

(b) DF image

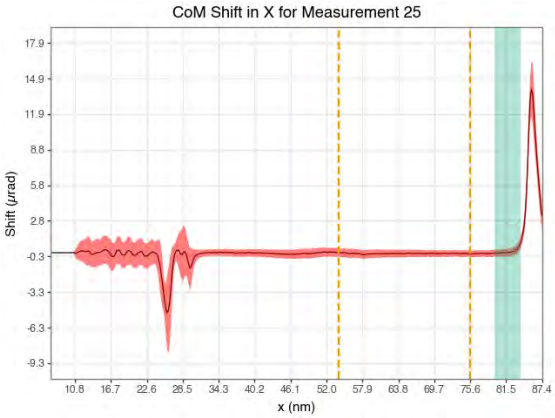

(c) CoM shift x-axis

(d) CoM shift y-axis

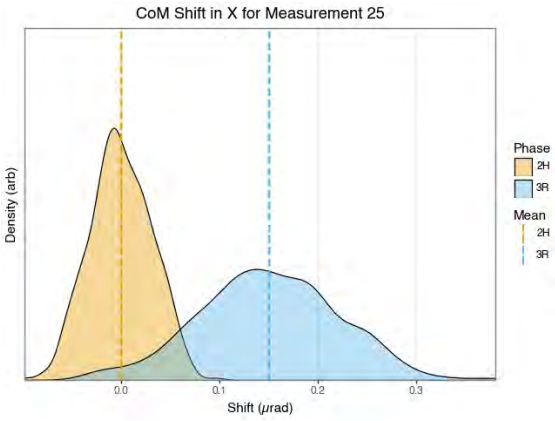

(e) CoM shift x-axis in 3R

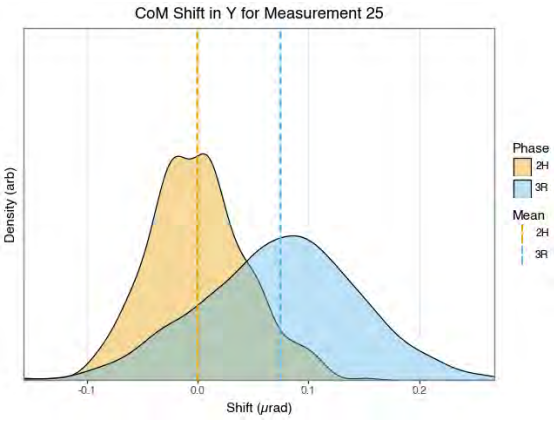

(f) CoM shift y-axis in 3R

Figure C.8: Scanned image 25.

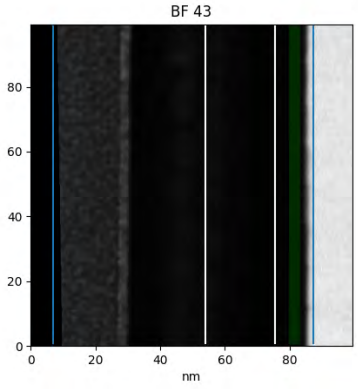

(a) BF image

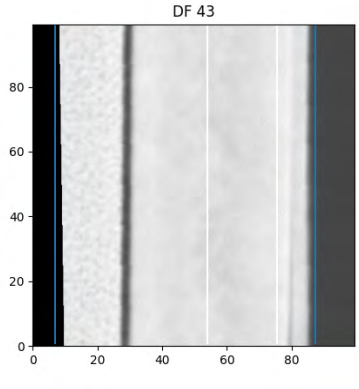

(b) DF image

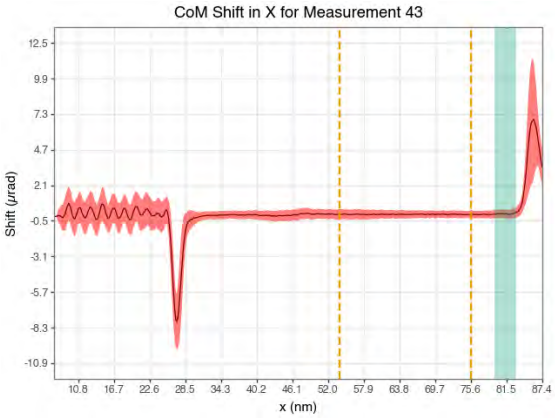

(c) CoM shift x-axis

(d) CoM shift y-axis

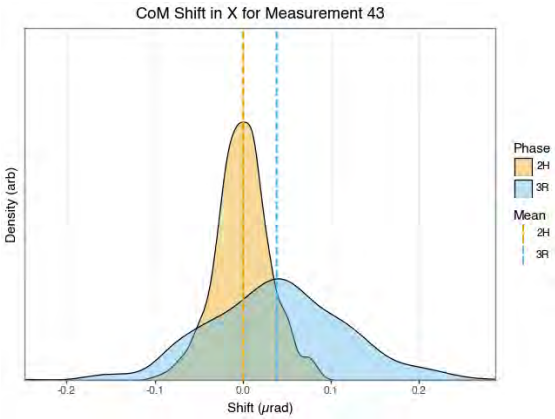

(e) CoM shift x-axis in 3R

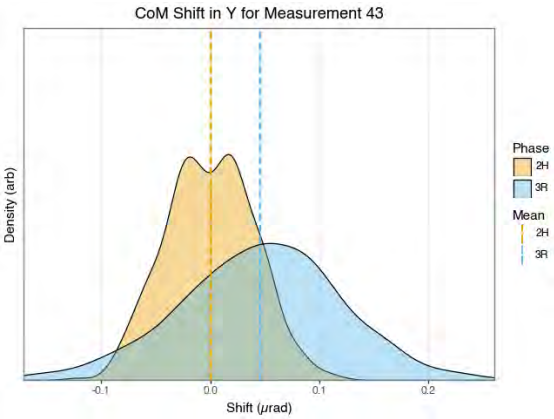

(f) CoM shift y-axis in 3R

Figure C.9: Scanned image 43.

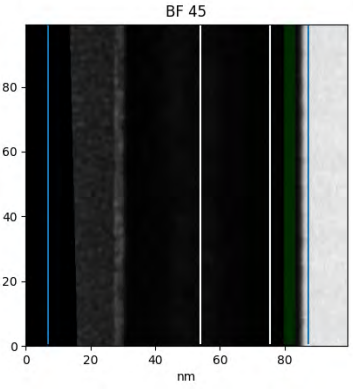

(a) BF image

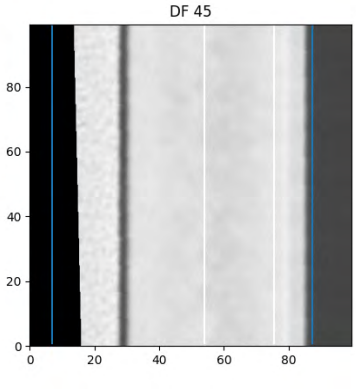

(b) DF image

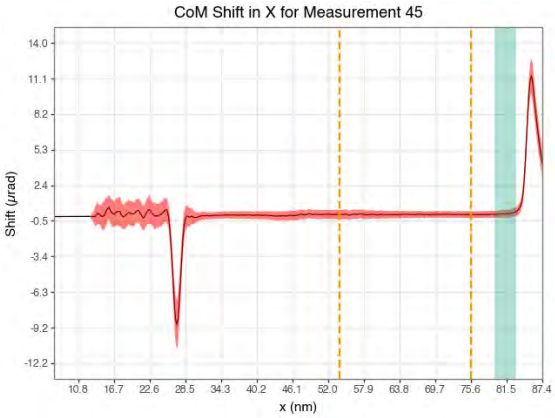

(c) CoM shift x-axis

(d) CoM shift y-axis

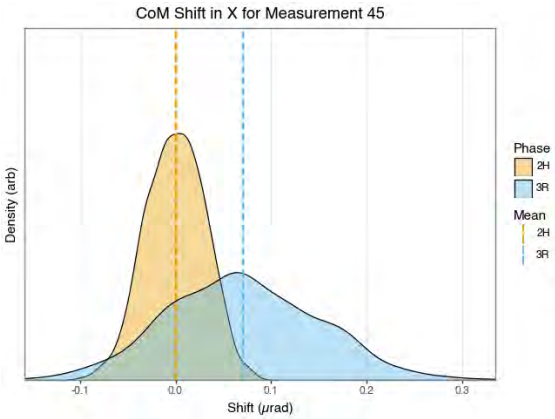

(e) CoM shift x-axis in 3R

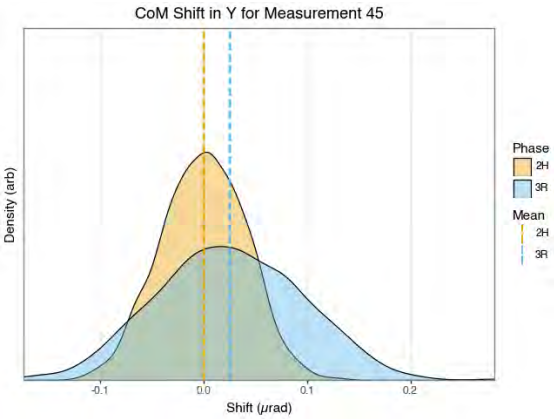

(f) CoM shift y-axis in 3R

Figure C.10: Scanned image 45.

D

TEM and STEM Images

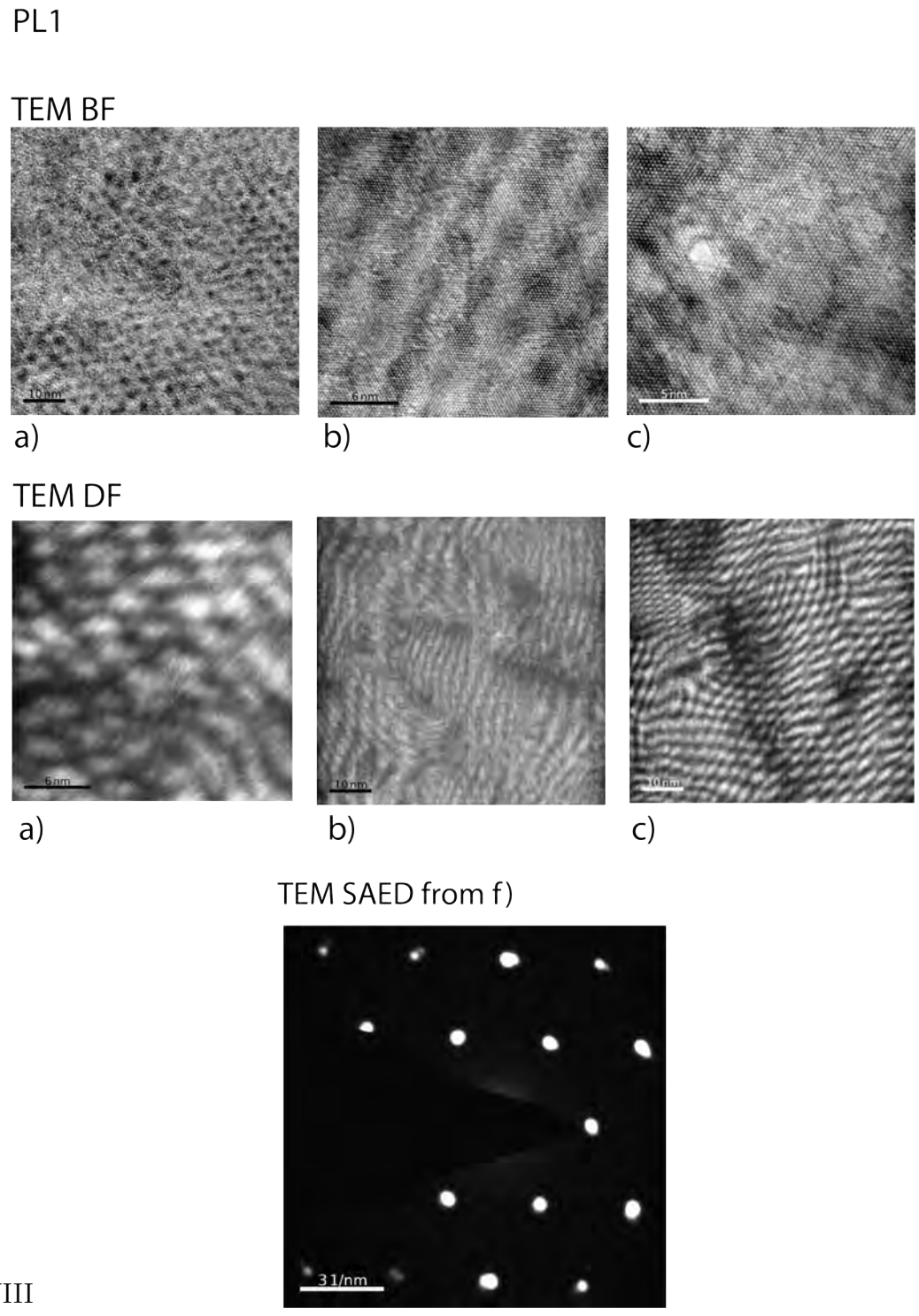

Figure D.1: Images from PL1.

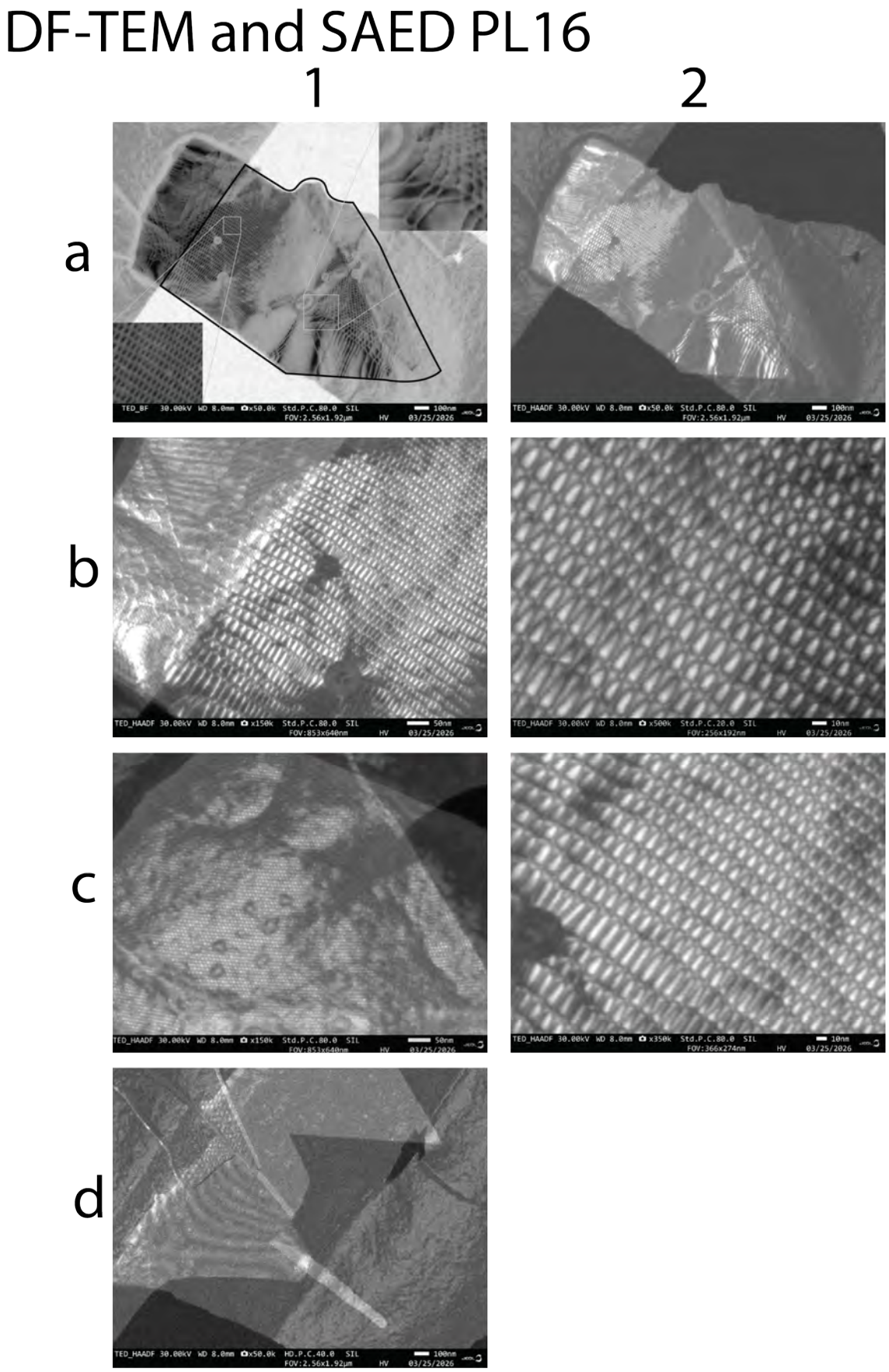

Figure D.2: TEM images from PL2.

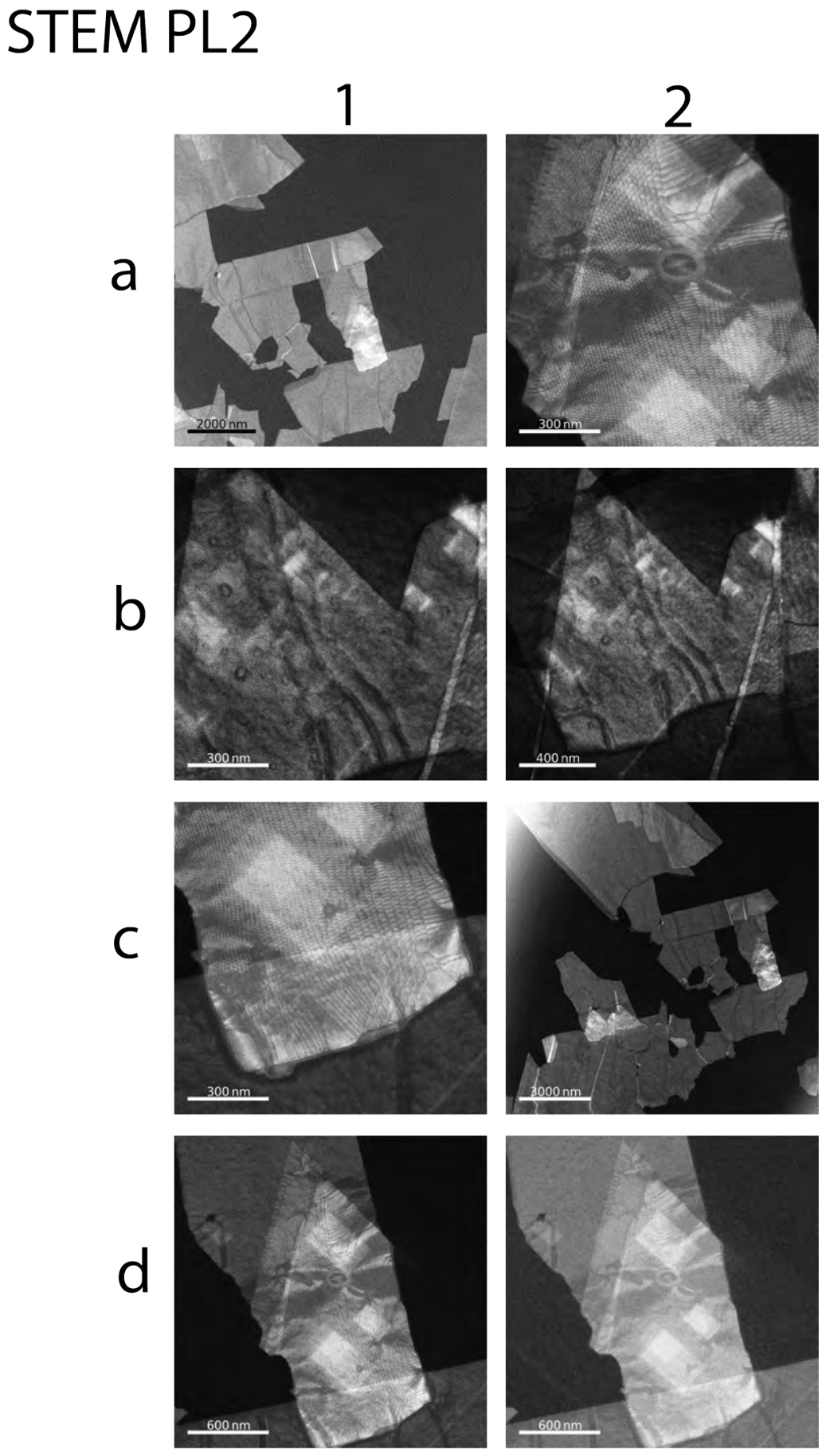

Figure D.3: STEM images from PL2.

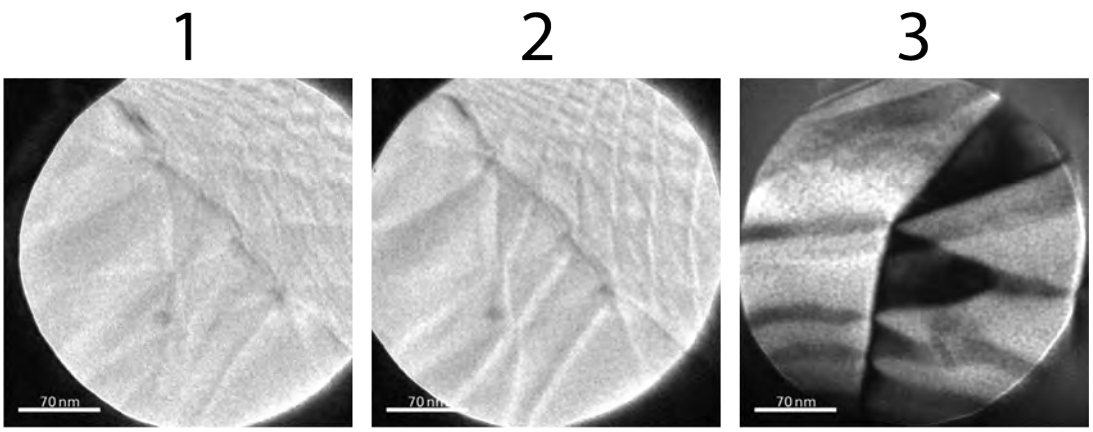

Figure D.4: TEM images from PL3.

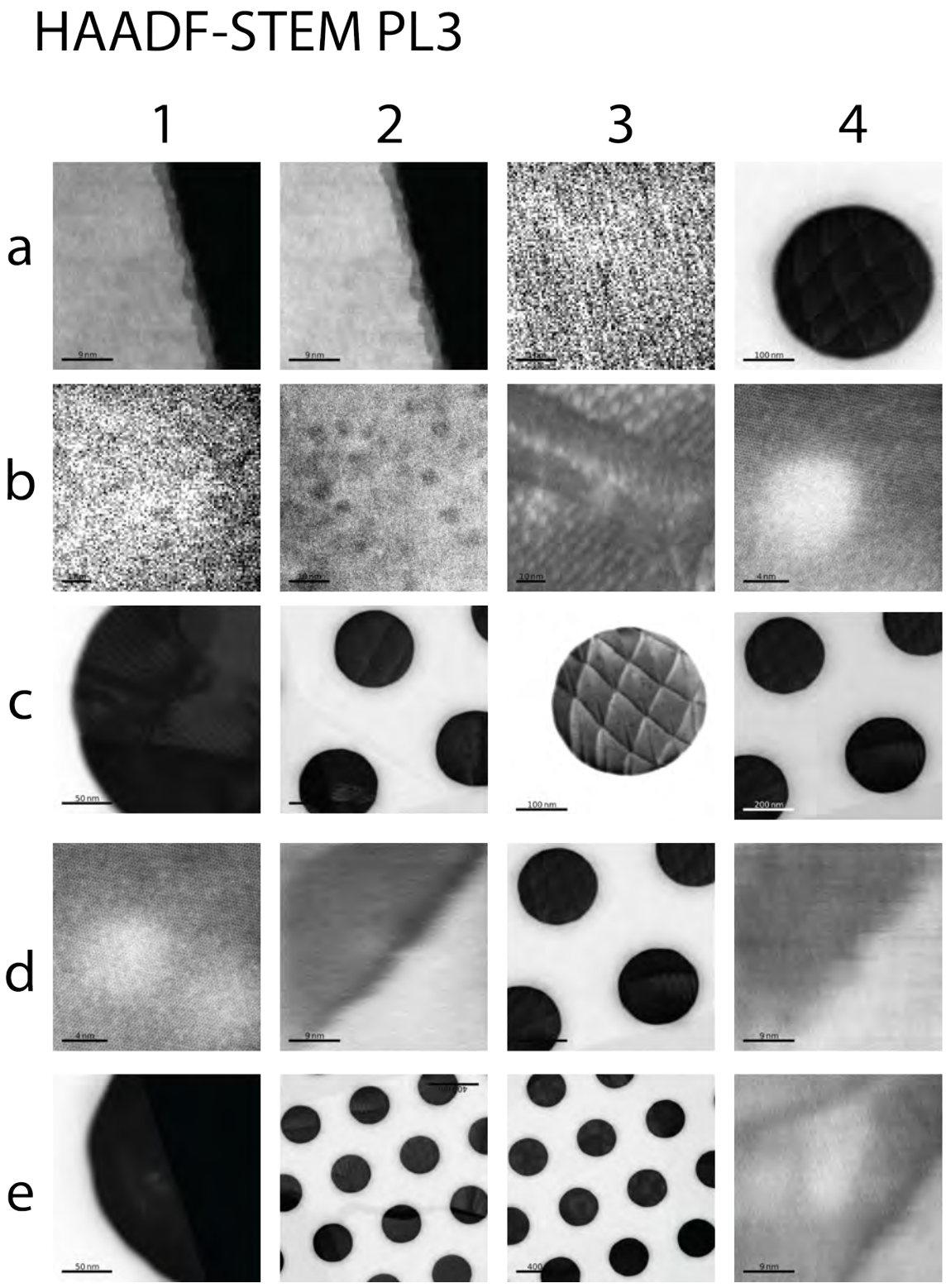

Figure D.5: STEM images from PL3.

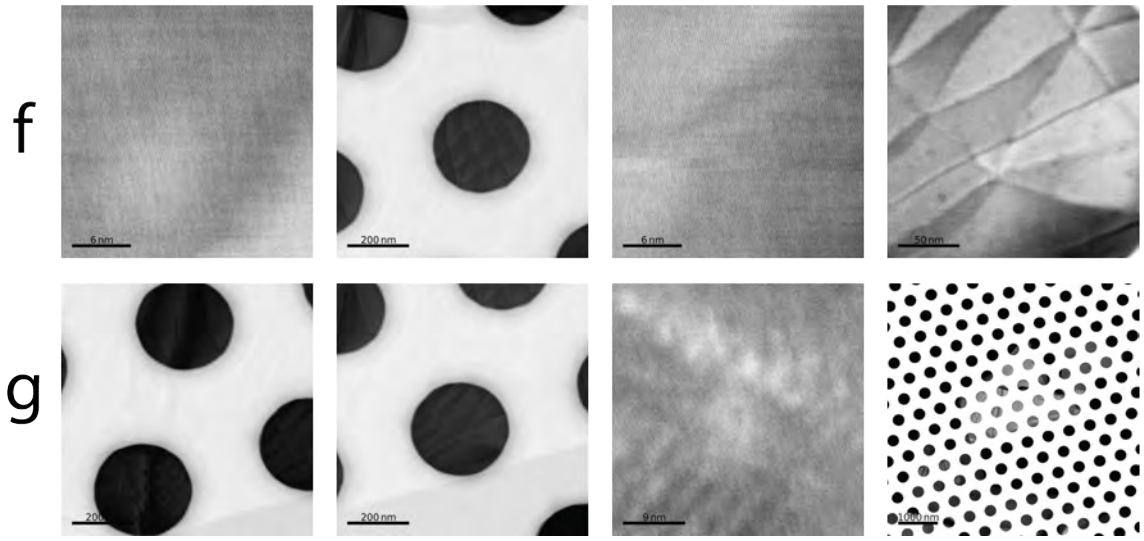

Figure D.6: STEM images from PL3.

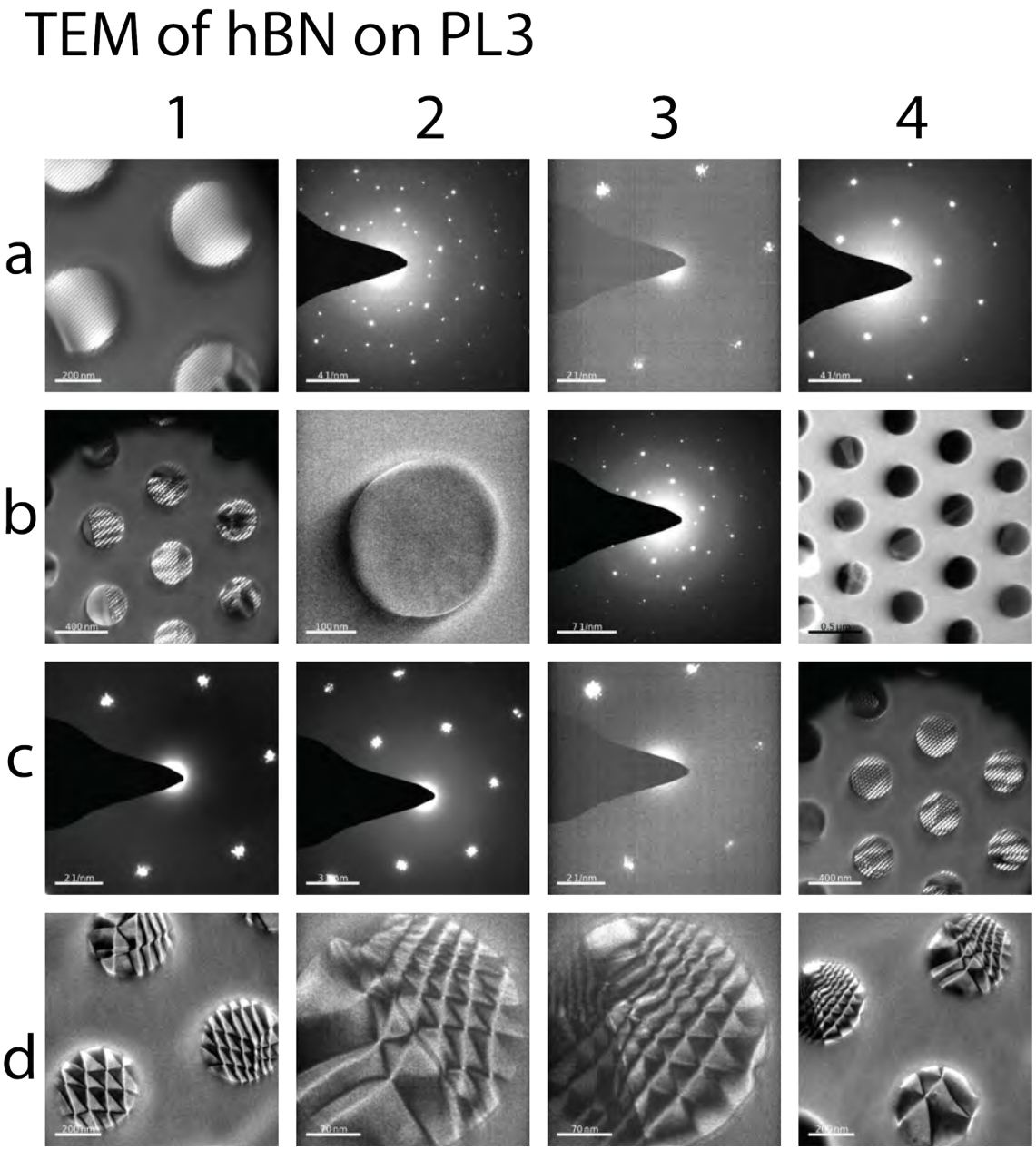

Figure D.7: STEM images from PL3 with hBN.

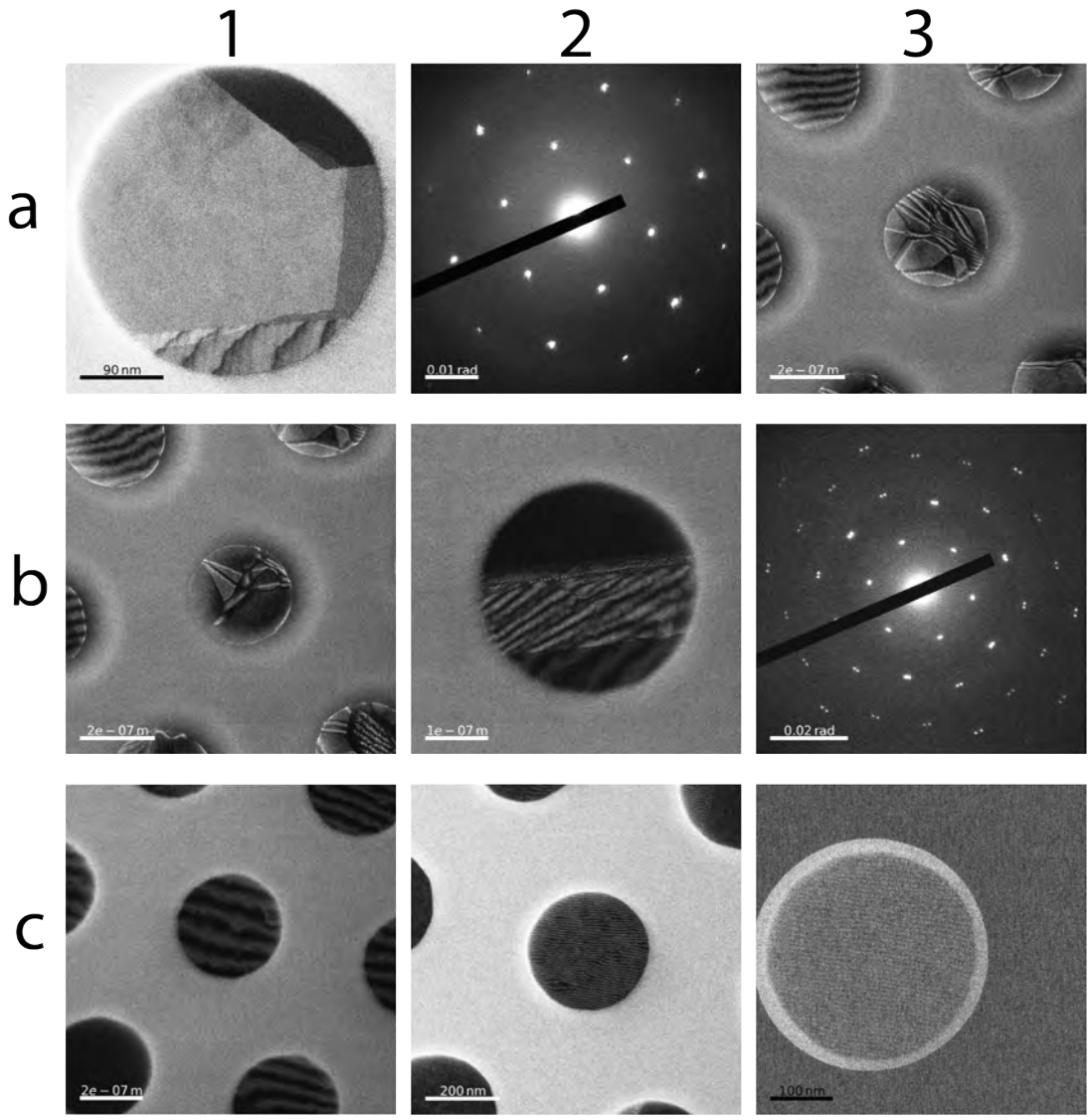

Figure D.8: STEM images from PL6.

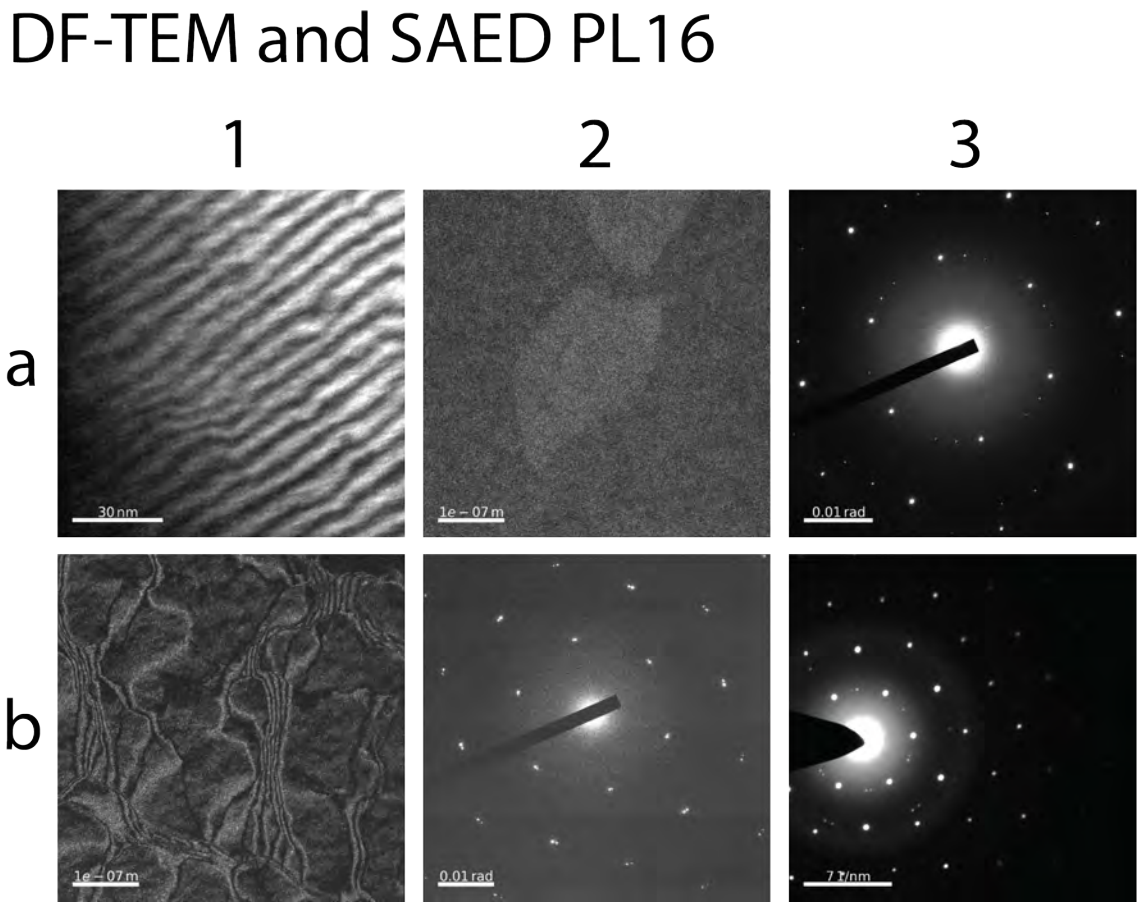

Figure D.9: TEM images from PL7.

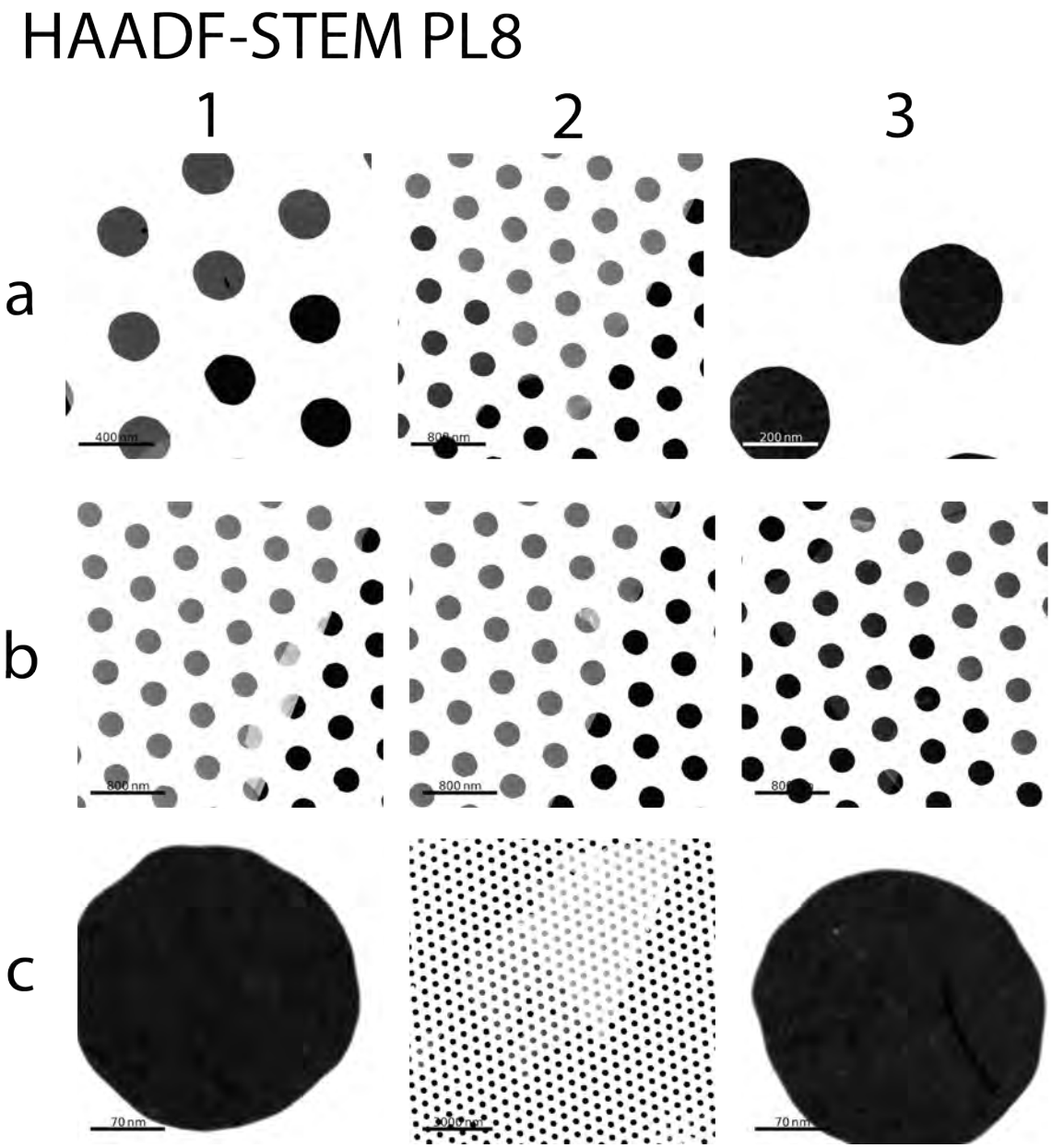

Figure D.10: STEM images from PL8.

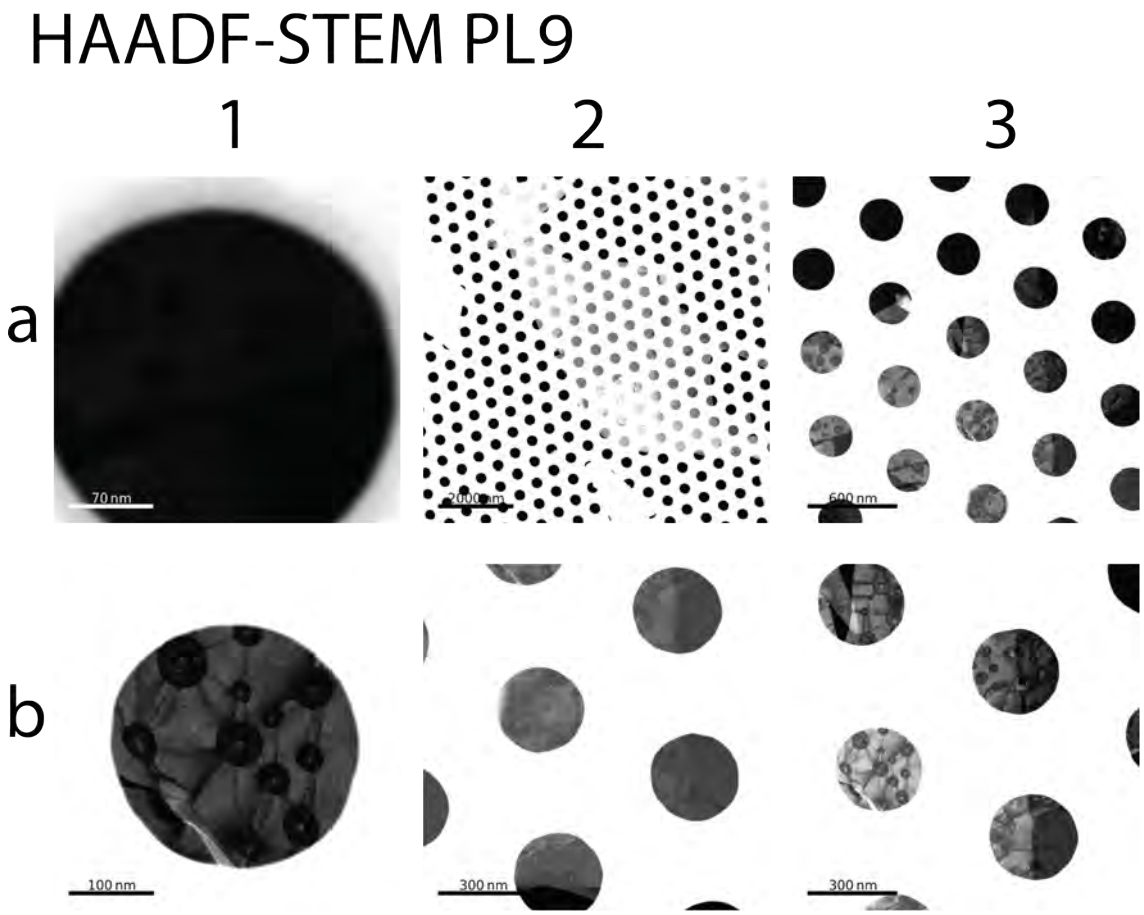

Figure D.11: STEM images from PL9.

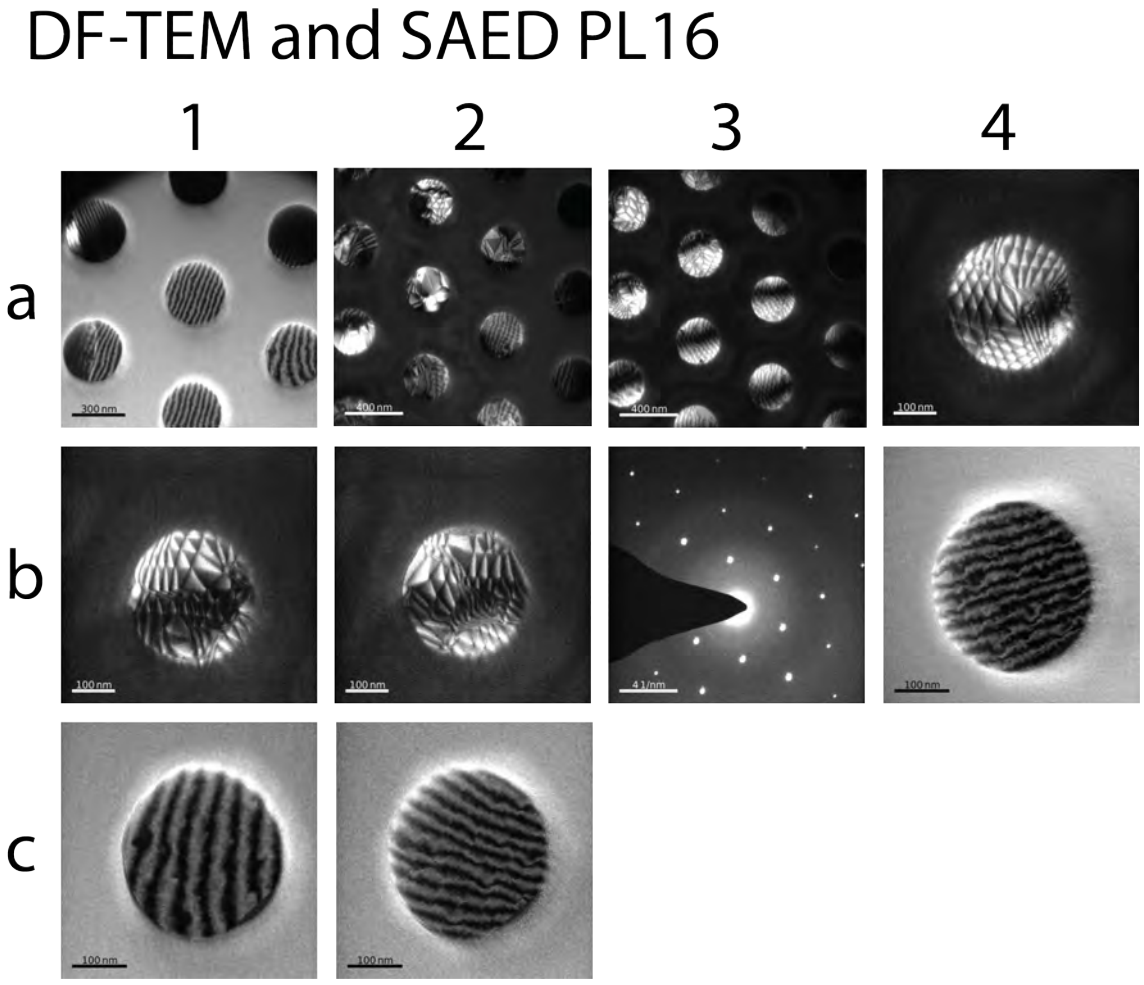

Figure D.12: TEM images from PL10.

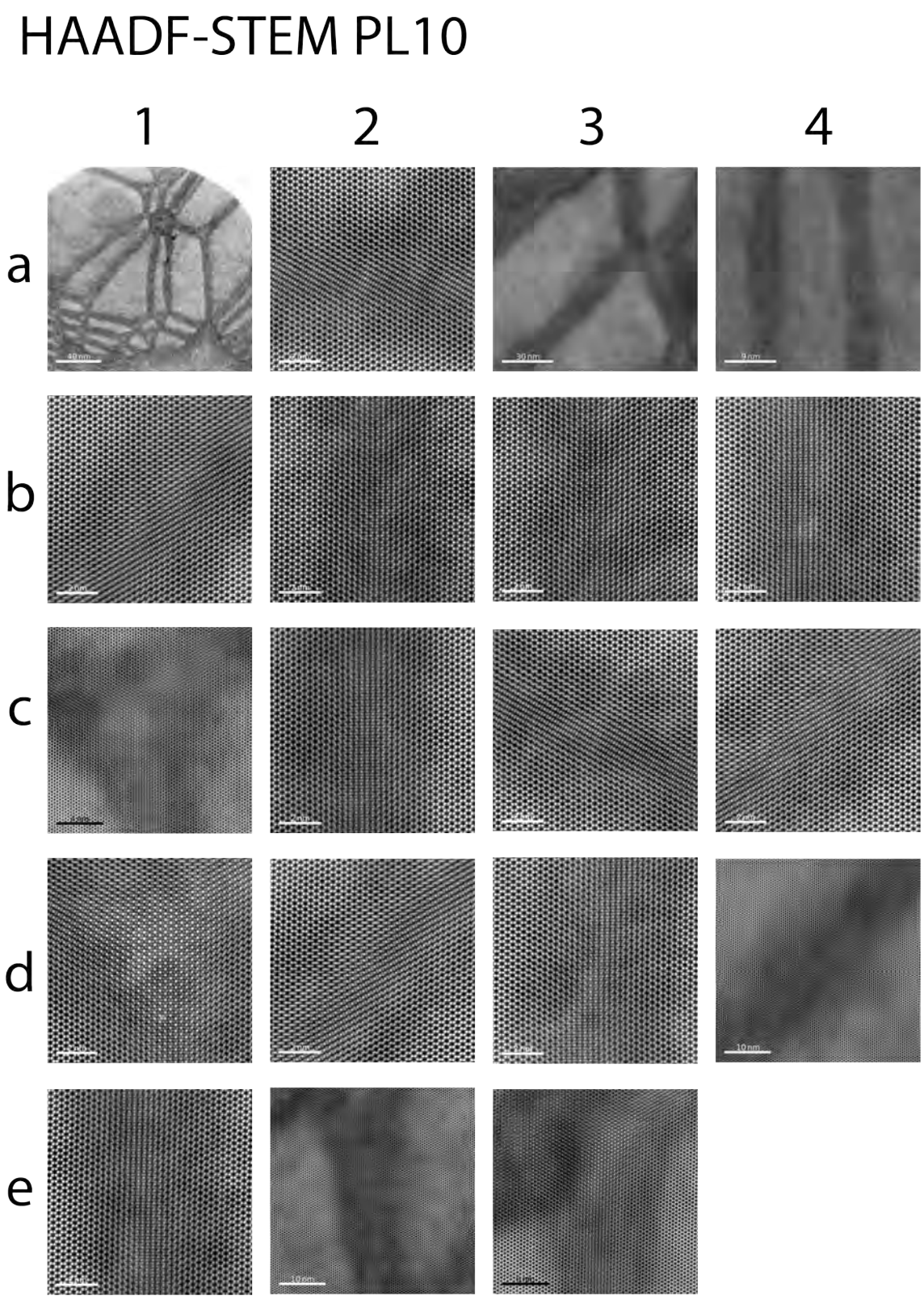

Figure D.13: STEM images from PL10.

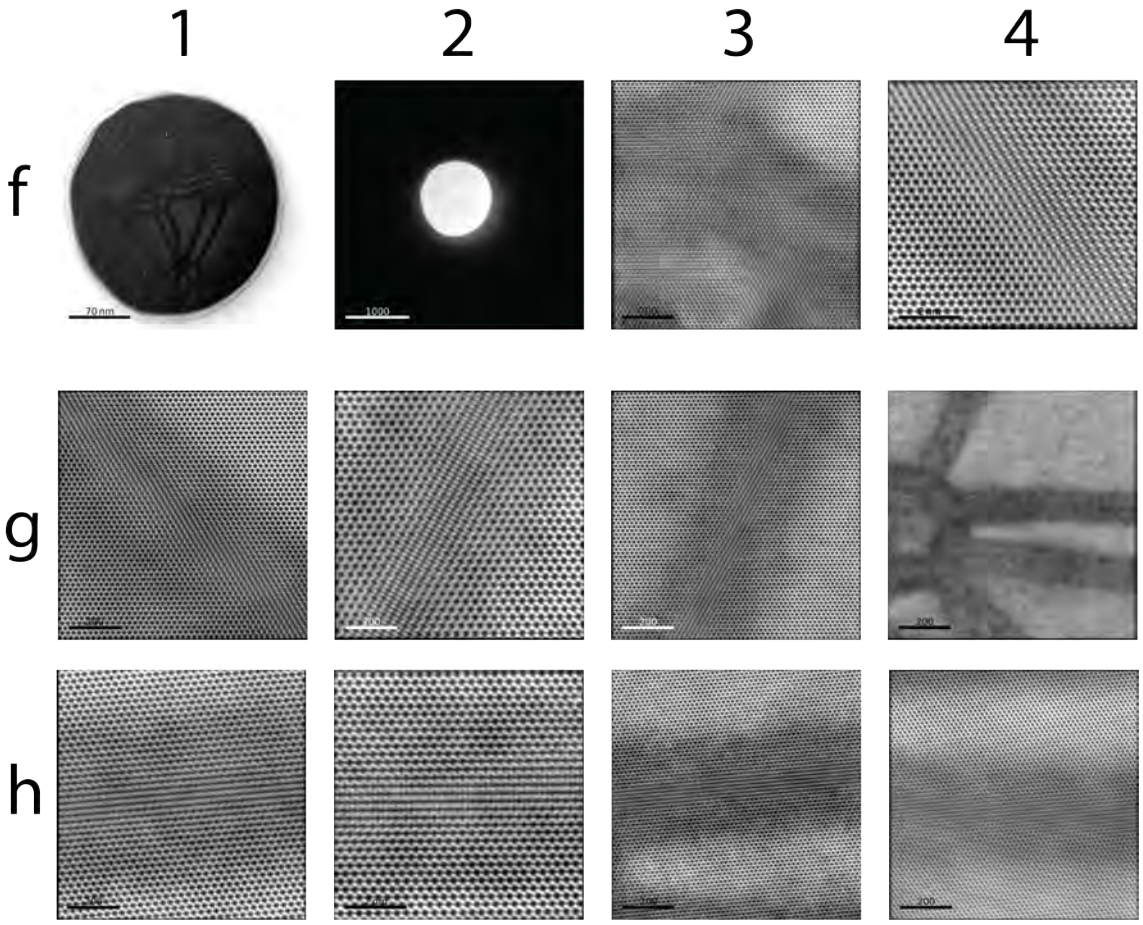

Figure D.14: STEM images from PL10.

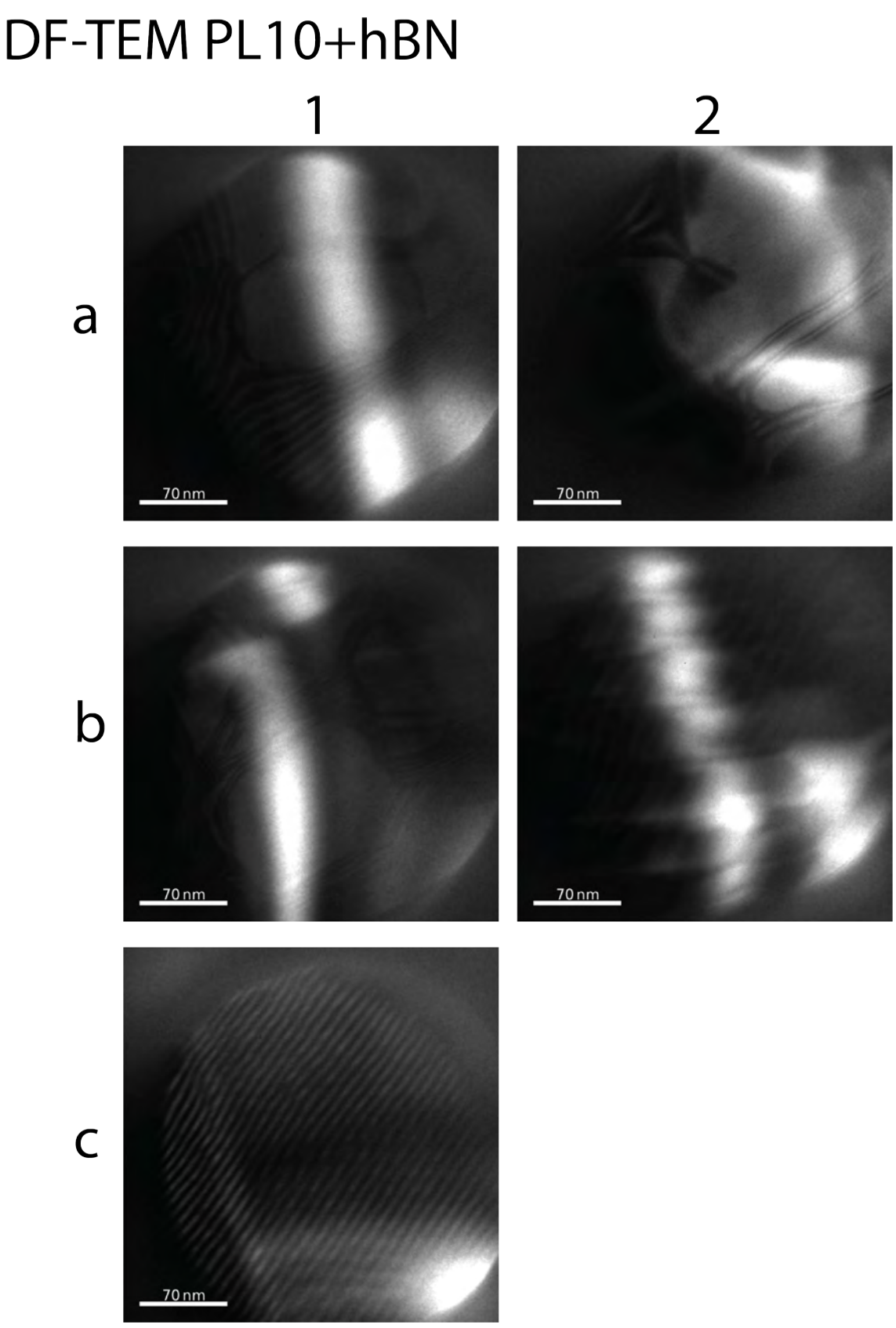

Figure D.15: TEM images from PL10 with hBN.

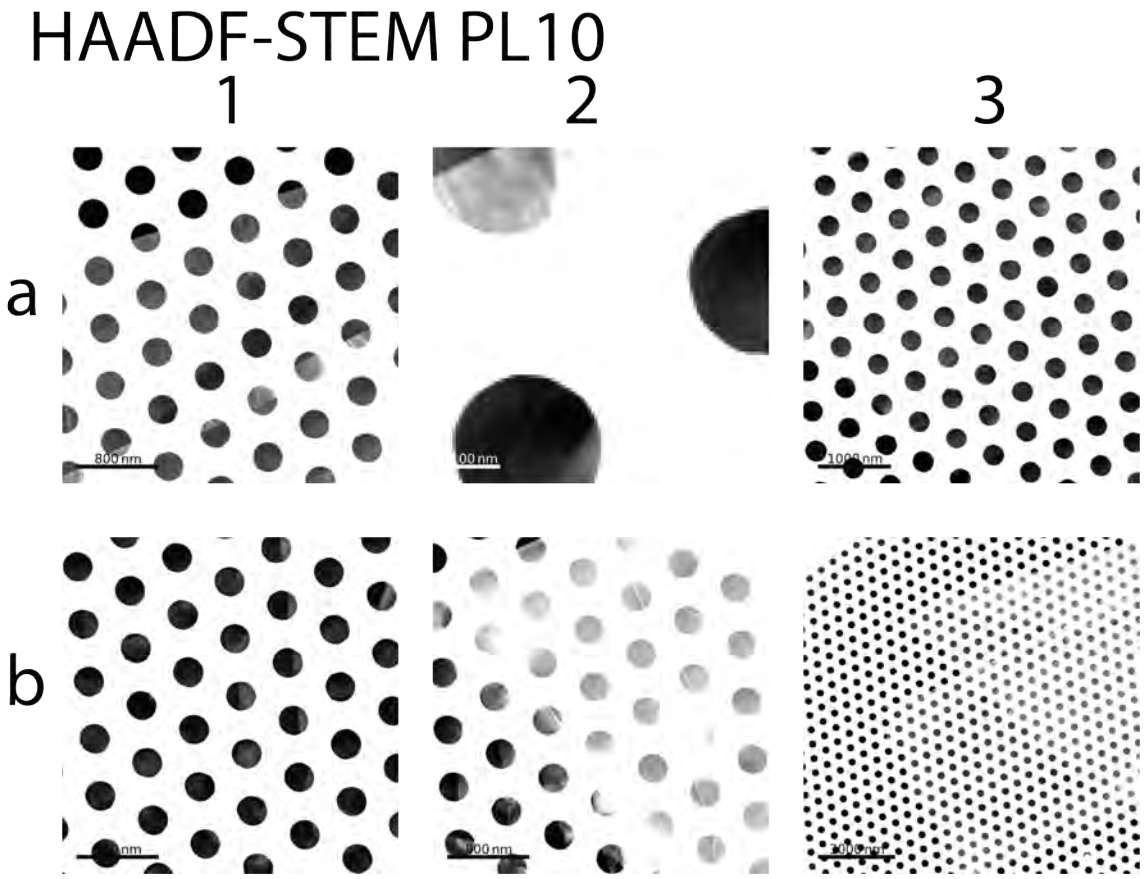

Figure D.16: STEM images from PL10 with hBN.

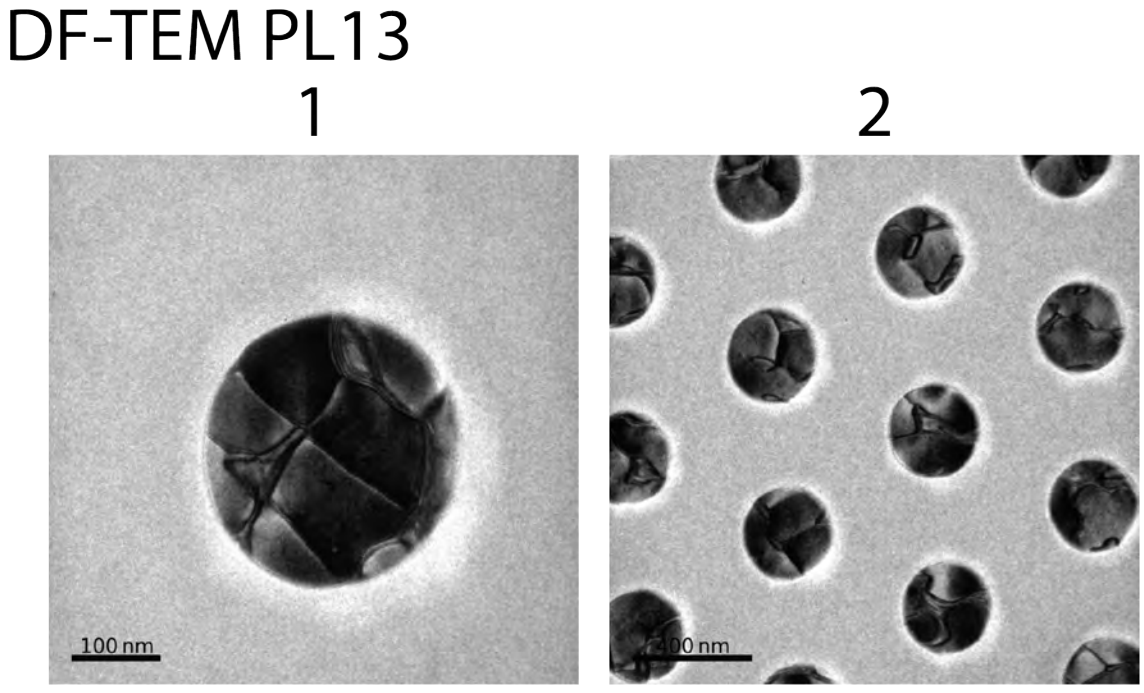

Figure D.17: TEM images from PL13.

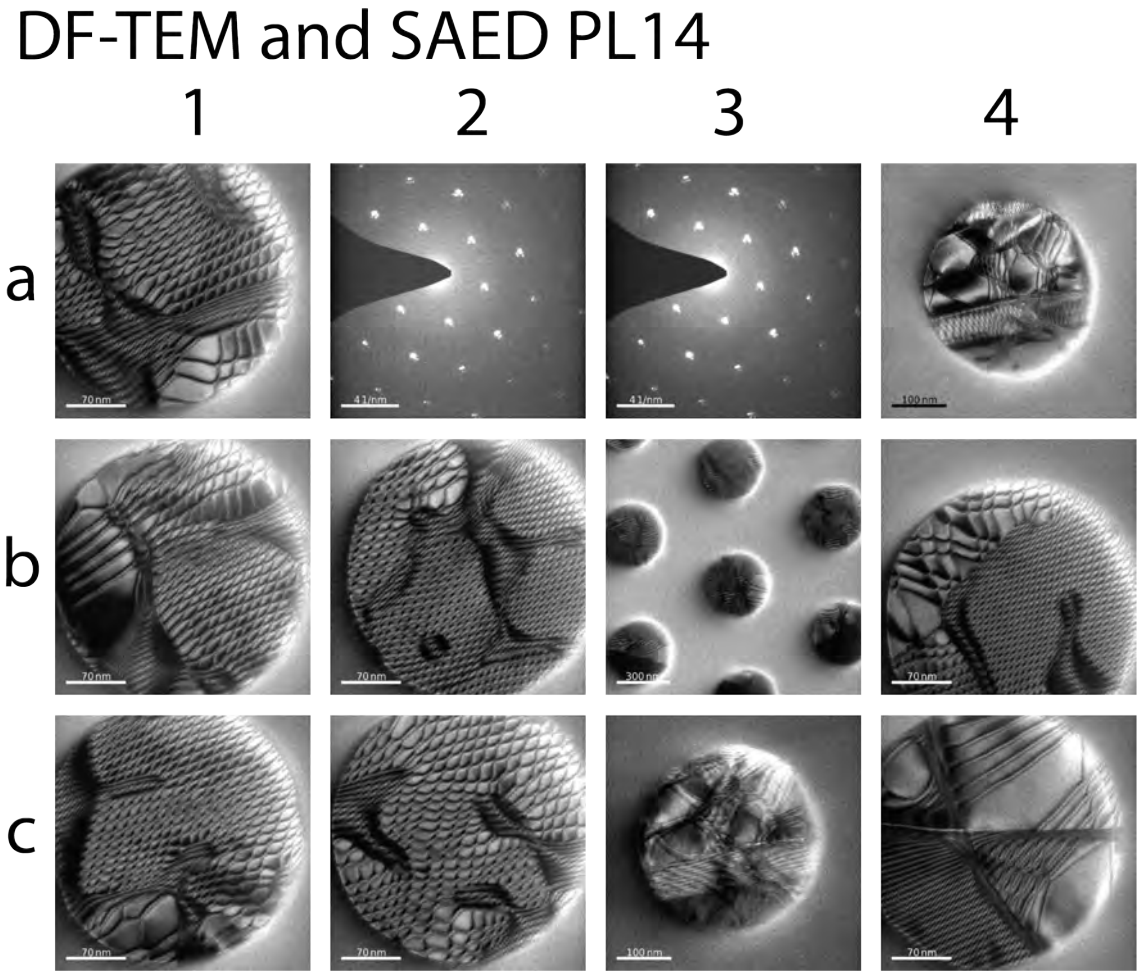

Figure D.18: TEM images from PL14.

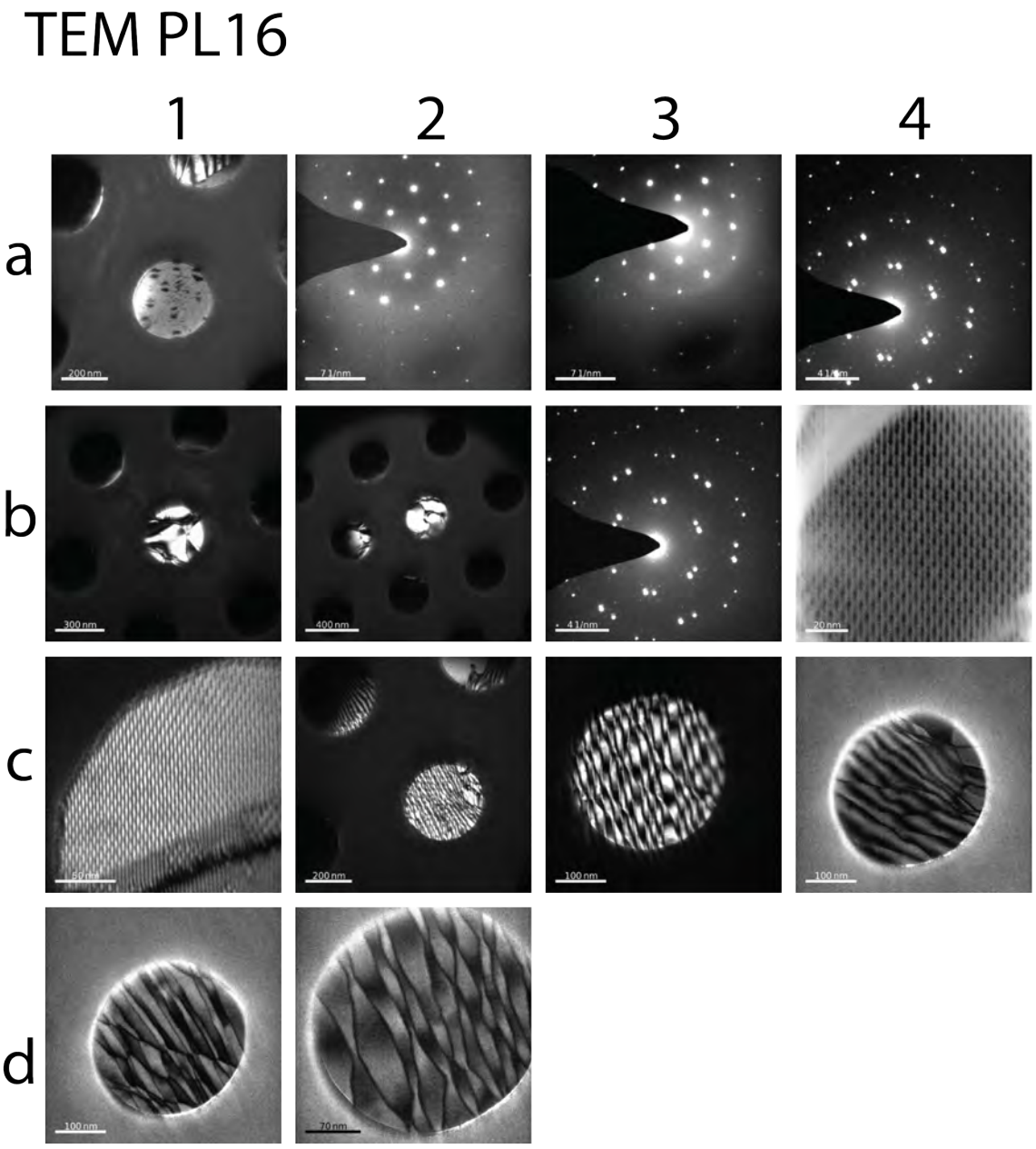

Figure D.19: TEM images from PL16.

DEPARTMENT OF PHYSICS AND ASTRONOMY
CHALMERS UNIVERSITY OF TECHNOLOGY
Gothenburg, Sweden
www.chalmers.se

CHALMERS
UNIVERSITY OF TECHNOLOGY